

First Search for Heavy Neutral Leptons with IceCube DeepCore

Dissertation
zur Erlangung des akademischen Grades
doctor rerum naturalium
(Dr. rer. nat.)

im Fach: Physik
Spezialisierung: Experimentalphysik

eingereicht an der
Mathematisch-Naturwissenschaftlichen Fakultät
der Humboldt-Universität zu Berlin

von
Leander Fischer M. Sc.
geboren am 24. Oktober 1992
in Heidelberg

Präsidentin der Humboldt-Universität zu Berlin
Prof. Dr. Julia von Blumenthal

Dekanin der Mathematisch-Naturwissenschaftlichen Fakultät
Prof. Dr. Caren Tischendorf

Copyright Notice

This book is released into the public domain using the CC-BY-4.0 code.

To view a copy of the CC-BY-4.0 code, visit:

<https://creativecommons.org/licenses/by/4.0/>

Colophon

This document was typeset with the help of KOMA-Script and L^AT_EX using the open-source kaobook template class.

The source code of this thesis is available at:

https://github.com/LeanderFischer/phd_thesis

Zusammenfassung

Zusammenfassung ...

Abstract

Abstract ...

Todo list

| | |
|--|----|
| Write introduction (RED) | 1 |
| Plot is missing + for W and 0 for Z boson. (RED) | 5 |
| Cite and/or sidenote this. (RED) | 6 |
| cite this (RED) | 6 |
| highlight a few more neutrino related open questions, to circle back to related to the HNL searches maybe? (YELLOW) | 6 |
| I need to explain the SM PMNS matrix before this, otherwise I'm missing that here.. (RED) | 7 |
| cite these and add some more (RED) | 7 |
| Say something about atmospheric neutrino flux uncertainties, based on recent JP/Anatoli papers. (YELLOW) | 13 |
| add current BF values from nufit or so? (YELLOW) | 13 |
| say something about how this changes with matter (YELLOW) | 14 |
| Re-write/re-formulate this section (copied from HNL technote). (RED) | 16 |
| add fancy icecube header picture here (ORANGE) | 19 |
| SB: there are more properties than just these. Somehow need a half sentence that explains why these are particularly important to single out (see ice papers for inspiration) (ORANGE) | 20 |
| CL: maybe define that absorption and scattering lengths are? they are defined differently so this invites a comparison that is not so obvious (ORANGE) | 20 |
| Add reference for the dust layer! Maybe also from the ice paper? mention/cite dust logger paper/pro- cedure? (ORANGE) | 20 |
| exchange for figure with scattering (check abs/sca is correct) (ORANGE) | 20 |
| Add accuracy of the efficiency calibration here. (ORANGE) | 21 |
| Blow up this image a bit, so it's better readable as marginfigure. (READ) | 21 |
| CL: value? (YELLOW) | 22 |
| SB: this needs revision. the energy range you mention is particular for oscillations already (atmopsheric neutrinos are plentiful outside of this range you mentioned). If you rewrite the first part you'll have to revisit the second part. Also in general I'd suggest not to rank analyses like Main and Other - DeepCore was orginally intended as a dark matter detector, and there are probably more DM analyses unblinded / year than oscillations. Just keep it general, no need to rank. (RED) . . | 22 |
| Cite n and θ_c (ORANGE) | 22 |
| SB: you already mentioned that Cher. Rad. doesn't lead to significant energy loss. I suggest to clean up the text a bit, you dont' need to emphasize that so many times. Pick one place (probably here) and eliminate it elsewhere (RED) | 23 |
| Add reference (PDG or find original) (ORANGE) | 23 |
| Add reference for these processes. (ORANGE) | 24 |
| cite em shower distribution (RED) | 24 |

| | |
|---|----|
| gamma (from equation) is not defined (RED) | 24 |
| Add angular profile plot (Summer agrees!) (create one based on Leif Rädel as Alex did) (RED) | 24 |
| JVS: I would describe simulation sets you produced in past rather than present tense (ORANGE) | 27 |
| Make my own DC string positions/distances plot version, viable for the margin? (YELLOW) | 27 |
| Re-make plot with all energies (cascades and total, both samples (they are the same)) (RED) | 28 |
| Re-make plot with all decay lengths (both samples) (RED) | 28 |
| describe why these are shown to highlight some key aspect (uniformity in both energies to sample the whole space, decay length as a result of the z sampling etc..), also add this shortly to the caption (RED) | 28 |
| again, describe what is shown and why this is interesting (e.g. energy distribution between the cascades, realistic exponential decay length distribution..) also add this to the captions shortly (RED) | 29 |
| JVS: consider remaking figures at the native size so type size is consistent. Also, consider making the legend box semi-transparent so the lines do not obscure the text and markers. (ORANGE) | 31 |
| Maybe decide if I want to handle git repo urls/references in a different way.. currently (without date+title) they look ugly in the margin, so I just state them as regular cites, but Cris gave me some other ideas on how to handle them.. (YELLOW) | 31 |
| Re-make plot with 3 target masses and better labels/legends etc. (RED) | 32 |
| SB: emphasize the cut-off/suppression (ORANGE) | 33 |
| Add comparisons of SM cross-sections between NuXSSplMkr and genie? (YELLOW) | 33 |
| Calculate max BRs or remove.. (RED) | 33 |
| JVS: consider also writing down the (trivial) 2-body decay kinematics for completeness and consistency. This transition is a bit jarring as it is (RED) | 34 |
| JVS: The build-up of the weight expression is hard to follow without knowing where it's going. It may be better to start with the fact that the importance sampling weight is the ratio of PDFs, then write down each pdf, then drill down into each of the terms (basically, the standard "tell me what you're going to tell me, then tell me, then tell me what you told me" scheme). (RED) | 35 |
| Combine low/high plots and remove all traces of the separation in the thesis (tables/text/etc.) (ORANGE) | 36 |
| What is the message of these plots? Make it clear in the text and also in the captions. Potentially cut down to one or two and leave the rest or move them to the appendix. (RED) | 36 |
| Adapt chapter to reflect switched chapter order (RED) | 37 |
| SB: Have you considered instead to have a chapter on all Simulation (signal and background) and then another chapter on Data processing and reconstruction? The model independent simulation description can either go into the simulation chapter OR it can go into the double cascade reconstruction chapter at an appropriate location/subsection (ORANGE) | 37 |
| put a number on this significant increase? (YELLOW) | 39 |
| put a number on the tilt angle? (YELLOW) | 40 |
| Add SPE distribution plot (RED) | 41 |
| Include some low level plots like the trigger efficiency for the HNL simulation (ORANGE) | 41 |
| add example plots (2?) for L3 cut variables and applied cuts (YELLOW) | 43 |
| add some figure showing the corridors? (YELLOW) | 44 |

| | |
|--|----|
| add table with rates per level (split in flavor) - maybe better in analysis chapter to also show signal? (RED) | 44 |
| add image with selected strings used for flercnn IC and DC (YELLOW) | 45 |
| add some performance plots of the FLERCNN reconstruction (ORANGE) | 46 |
| There is more information on pre-processing the samples and preparing the input features, and training each cnn, but I'm not sure if that might be too much detail? (YELLOW) | 46 |
| add reference for flercnn analysis internal note (ORANGE) | 46 |
| SB: I think its better to discuss the sources of uncertainty when you introduce each component, e.g. when you talk about cross-sections you can explain the existing measurements and models, and how the uncertainty is derived. Same for the detector calibration uncertainties - you can discuss the magnitude of the errors and how they are derived when you discuss the detector. (ORANGE) | 47 |
| add figure with Barr blocks? (RED) | 48 |
| which experiments measure the axial mass? (ORANGE) | 48 |
| cite this? (YELLOW) | 51 |
| maybe I want a figure for this, or not so important? (YELLOW) | 53 |
| Elaborate whether this is the case (show it in a plot?). Discuss directionality of cascades in general. (ORANGE) | 53 |
| fix caption of this figure (RED) | 54 |
| fix caption of this figure (RED) | 55 |
| one half sentence on why this number was chosen? (ORANGE) | 56 |
| make on figure, where the two selected regions are highlighted? (RED) | 58 |
| fix caption (RED) | 58 |
| re-make normalized? (ORANGE) | 59 |
| fix caption (RED) | 59 |
| re-make normalized? (ORANGE) | 59 |
| fix caption (RED) | 59 |
| circle back to the energy distributions I showed somewhere else, and state how the cascade energies are distributed in general (ORANGE) | 60 |
| fix caption of this figure (RED) | 61 |
| describe the "good fit" selection when I first show plots that use it (ORANGE) | 61 |
| add some 1D resolution plots (ORANGE) | 61 |
| fix caption of this figure (RED) | 62 |
| fix caption of this figure (RED) | 62 |
| fix caption of this figure (RED) | 63 |
| fix caption of this figure (RED) | 63 |
| fix caption of this figure (RED) | 63 |
| Make plot to show efficiency of the OscNext selection for HNL events. (ORANGE) | 63 |
| Plot energy (true total) and true decay length across the different levels (ORANGE) | 63 |
| Make table with the rates across the different levels for benchmark mass/mixing (ORANGE) | 63 |

| | |
|--|----|
| Should I adapt the total numbers to match the sum of the rounded individual parts? (YELLOW) | 68 |
| add 3D data histograms (RED) | 68 |
| Add fractions of the different particle types in the bins for benchmark mass/mixing (another table?) (ORANGE) | 68 |
| fix caption (RED) | 68 |
| remake without the top row of masked bins? add label to cbar and remove from title (RED) | 68 |
| Do I want/need to include the description of the KDE muon estimation? (YELLOW) | 69 |
| SB: generally you are missing a lot of references, and I don't think its very nice to read all these ranges and so on in the text. Surely you can just have a table with the systematics you include, their allowed range and prior if applicable? You can choose whether or not you want to discuss some parameters in more detail here, but it should be a discussion of the physics and impact on the analysis. e.g. you can include some plots showing how a change in some of the nuisance parameters changes the event counts in the analysis binning (RED) | 70 |
| Blow up labels/legend/title and make it more readable in the margin or move it into the main text? (RED) | 70 |
| elaborate why this is also done to cover the whole energy range for the Pion production, referencing the Barr Block plot that I haven't included yet :D (RED) | 70 |
| Need cite here! (RED) | 70 |
| I should add some final level effects of some systematics on the 3D binning and maybe discuss how they are different from the signal shape, or so? (ORANGE) | 71 |
| I still need to write this section... (RED) | 71 |
| Do I want more information about the different pipelines and stages? Could link back to the extra stage I wrote and add the earth model and oscillation calculation information here, I guess?! (ORANGE) | 71 |
| Put all three mass samples in one plot and adjust the text to it? Remove "fit start" from legend. (RED) | 72 |
| Mention that the mis-modeling (what it is) is at the order of 1e-07 for all of them (check again) and refer to the deviations in the mixing to be not relevant because of that! (RED) | 72 |
| Add 3D BFP-data pull distribution for one mass (they look the same, no?) (RED) | 73 |
| fix dimension to fit them in one row! (RED) | 73 |
| specify which they are, once I have them (RED) | 73 |
| add 1-d data/mc agreement for example mass sample (0.6?) and all 3 analysis variables (RED) | 73 |
| add table with reduced chi2 for all 1-d distributions (RED) | 73 |
| Cite (again)! (RED) | 73 |
| Compare here the best fit oscillation parameters to the FLERCNN results and try to quantify it, stating the pitfalls of the comparitions (statistically fully dependent) (RED) | 73 |
| Plot updates: change 0.6 GeV color, sort variables by type (same as table), offset markers left/right, change grid lines to separate the parameter region, ylabel limit instead of range (RED) | 73 |
| Show best fit hole ice angular acceptance compared to nominal and flasher/in-situ fits, maybe? (YELLOW) | 73 |
| Discuss what it means that the parameters are at these values? Here, or somewhere else? (RED) | 73 |
| fix table caption (RED) | 74 |
| add horizontal CL lines? | 75 |
| fix caption for this figure (RED) | 75 |

| | |
|--|----|
| make plot with BFPs and limit, comparing to upper limits from other experiments, think about how to present it (RED) | 75 |
| Write conclusion (RED) | 79 |
| Re-make plot with x,y for horizontal set one plot! | 83 |
| Re-make plot with x, y, z for both cascades in one. | 83 |
| Re-arrange plots in a more sensible way. | 83 |
| fix caption and design + significant digits to show (ORANGE) | 85 |
| maybe show range/prior and then deviation in sigma, or absolute for the ones without prior | 85 |

Contents

| | |
|--|-----------|
| Abstract | iii |
| Contents | xi |
| 1 Introduction | 1 |
| 2 Standard Model Neutrinos and Beyond | 3 |
| 2.1 The Standard Model | 3 |
| 2.1.1 Fundamental Fields | 3 |
| 2.1.2 Electroweak Symmetry Breaking | 4 |
| 2.1.3 Fermion Masses | 5 |
| 2.1.4 Leptonic Weak Interactions after Symmetry Breaking | 5 |
| 2.2 Beyond the Standard Model | 5 |
| 2.2.1 Mass Mechanisms | 6 |
| 2.2.2 Observational Avenues for Right-Handed Neutrinos | 7 |
| 2.2.3 Searching for Heavy Neutral Leptons | 7 |
| 2.3 Atmospheric Neutrinos as Source of Heavy Neutral Leptons | 12 |
| 2.3.1 Production of Neutrinos in the Atmosphere | 12 |
| 2.3.2 Oscillations | 13 |
| 2.3.3 Interactions with Nuclei | 14 |
| 3 The IceCube Neutrino Observatory | 19 |
| 3.1 Detector Components | 19 |
| 3.1.1 Digital Optical Modules and the Antarctic Ice | 20 |
| 3.1.2 IceCube | 21 |
| 3.1.3 DeepCore | 21 |
| 3.2 Particle Propagation in Ice | 22 |
| 3.2.1 Cherenkov Effect | 22 |
| 3.2.2 Energy Losses | 23 |
| 3.3 Event Morphologies | 25 |
| 4 Heavy Neutral Lepton Signal Simulation | 27 |
| 4.1 Model Independent Simulation | 27 |
| 4.1.1 Simplistic Samples | 27 |
| 4.1.2 Realistic Sample | 28 |
| 4.2 Model Dependent Simulation | 30 |
| 4.2.1 Custom LeptonInjector | 30 |
| 4.2.2 Sampling Distributions | 34 |
| 4.2.3 Weighting Scheme | 35 |
| 4.2.4 Generation Level Distributions | 36 |
| 5 Standard Model Background Simulation and Data Processing | 37 |
| 5.1 Event Generation | 37 |
| 5.1.1 Neutrinos | 38 |
| 5.1.2 Muons | 39 |
| 5.2 Detector Simulation | 39 |
| 5.2.1 Photon Propagation | 39 |
| 5.2.2 Detector Responses | 40 |
| 5.3 Processing | 41 |
| 5.3.1 Trigger and Filter | 41 |
| 5.3.2 Event Selection | 42 |

| | | |
|-----------------|---|-----------|
| 5.4 | Reconstruction | 44 |
| 5.4.1 | Fast Low Energy Reconstruction using Convolutional Neural Networks | 45 |
| 5.4.2 | Analysis Selection | 46 |
| 5.5 | Systematic Uncertainties | 47 |
| 5.5.1 | Atmospheric Flux Uncertainties | 47 |
| 5.5.2 | Cross-Section Uncertainties | 48 |
| 5.5.3 | Detector Calibration Uncertainties | 49 |
| 5.5.4 | Muon Uncertainties | 50 |
| 6 | Detecting Low Energetic Double Cascades | 53 |
| 6.1 | Reconstruction | 53 |
| 6.1.1 | Table-Based Minimum Likelihood Algorithms | 53 |
| 6.1.2 | Optimization for Low Energy Events | 54 |
| 6.1.3 | Performance | 56 |
| 6.2 | Double Cascade Classification | 60 |
| 6.3 | Generic Double Cascade Performance | 60 |
| 6.3.1 | Idealistic Performance | 61 |
| 6.3.2 | Realistic Performance | 61 |
| 6.3.3 | Low Energy Event Selection Efficiency | 63 |
| 7 | Search for Tau Neutrino Induced Heavy Neutral Lepton Events | 67 |
| 7.1 | Final Level Sample | 67 |
| 7.1.1 | Expected Rates/Events | 67 |
| 7.1.2 | Analysis Binning | 68 |
| 7.2 | Statistical Analysis | 69 |
| 7.2.1 | Test Statistic | 69 |
| 7.2.2 | Physics Parameters | 69 |
| 7.2.3 | Nuisance Parameters | 70 |
| 7.2.4 | Treatment of Detector Response Uncertainties via a Likelihood-Free Inference Method | 71 |
| 7.2.5 | Low Energy Analysis Framework | 71 |
| 7.3 | Analysis Checks | 71 |
| 7.3.1 | Minimization Robustness | 72 |
| 7.3.2 | Goodness of Fit | 72 |
| 7.3.3 | Data/MC Agreement | 73 |
| 7.4 | Results | 73 |
| 7.4.1 | Best Fit Nuisance Parameters | 73 |
| 7.4.2 | Best Fit Parameters and Limits | 74 |
| 8 | Summary and Discussion | 77 |
| 8.1 | Performance to Detecting Low Energetic Double Cascades | 77 |
| 8.2 | Search for Heavy Neutral Lepton Production and Decay | 77 |
| 8.2.1 | Agreement with Standard Model Three-Flavor Oscillation Measurement | 77 |
| 8.3 | Outlook | 77 |
| 8.3.1 | Shape Analysis Improvements | 77 |
| 8.3.2 | Test Coupling to Electron/Muon Flavor | 77 |
| 8.3.3 | Test Additional Coupling Processes | 77 |
| 8.3.4 | IceCube Upgrade | 77 |
| 9 | Conclusion | 79 |
| APPENDIX | | 81 |
| A | Heavy Neutral Lepton Signal Simulation | 83 |
| A.1 | Model Independent Simulation Distributions | 83 |

| | | |
|----------|--|-----------|
| A.2 | Model Dependent Simulation Distributions | 84 |
| B | Analysis Results | 85 |
| B.1 | Best Fit Nuisance Parameters | 85 |
| | Bibliography | 87 |

List of Figures

| | |
|---|----|
| 2.1 Feynman diagrams of neutrino weak interactions | 5 |
| 2.2 Current $ U_{\tau 4}^2 - m_4$ limits | 10 |
| 2.3 Atmospheric neutrino fluxes | 12 |
| 2.4 Neutrino-nucleon deep inelastic scattering | 15 |
| 2.5 Total inclusive neutrino-nucleon cross-sections | 15 |
| 2.6 HNL decay widths | 16 |
| 3.1 IceCube overview | 19 |
| 3.2 IceCube sideview | 20 |
| 3.3 Digital Optical Module (DOM) | 21 |
| 3.4 IceCube top view | 21 |
| 3.5 Cherenkov light front | 23 |
| 4.1 DeepCore string spacing | 28 |
| 4.2 Simplified model independent simulation generation level distributions | 29 |
| 4.3 Realistic model independent simulation generation level distributions | 30 |
| 4.4 HNL branching ratios | 31 |
| 4.5 Custom HNL total cross-sections for the four target masses compared to the total ($\nu_\tau/\bar{\nu}_\tau$ NC) cross-section used for SM neutrino simulation production with GENIE. | 32 |
| 4.6 Model dependent simulation generation level distributions | 36 |
| 5.1 Depth dependent scattering and absorption lengths | 40 |
| 5.2 IceCube trigger efficiencies | 41 |
| 5.3 Level 4 classifier outputs (muon and noise) | 44 |
| 5.4 FLERCNN architecture | 45 |
| 5.5 FLERCNN muon classifier probability distributions | 46 |
| 5.6 Inclusive total neutrino-nucleon cross-sections | 49 |
| 5.7 Hole ice angular acceptance modification | 50 |
| 6.2 short | 55 |
| 6.3 Preliminary 2-d reconstructed versus true cascade energy resolutions | 57 |
| 6.4 Preliminary 2-d reconstructed versus true decay length resolutions | 58 |
| 7.2 xx | 70 |
| 7.3 Asimov inject/recover test (0.6 GeV) | 72 |
| 7.4 Pseudo-data trials fit metric distribution (0.6 GeV) | 73 |
| 7.5 Best fit nuisance parameter distances to nominal | 74 |
| 7.6 xx | 75 |
| A.1 Simplified model independent simulation generation level distributions | 83 |
| A.2 Realistic model independent simulation generation level distributions | 84 |
| A.3 Model dependent simulation generation level distributions | 84 |

List of Tables

| | |
|---|----|
| 2.1 Standard model fermions | 4 |
| 3.1 IceCube low energy event signatures and underlying interactions | 25 |
| 4.1 Simplified model independent simulation sampling distributions | 29 |
| 4.2 Realistic model independent simulation sampling distributions | 30 |
| 4.3 HNL mass dependent decay channels | 33 |
| 4.4 Model dependent simulation sampling distributions | 34 |
| 5.1 GENIE generation cylinder volumes | 38 |
| 5.2 Vuvuzela noise simulation parameters | 41 |
| 5.3 Final analysis cuts | 47 |
| 7.1 Final level background event/rate expectation | 68 |
| 7.2 Final level signal event/rate expectation | 68 |
| 7.3 Analysis binning | 68 |
| 7.4 Nuisance parameter nominal values and fit ranges | 71 |
| 7.5 Staged minimization routine settings | 72 |
| 7.6 xx | 74 |
| B.1 xx | 85 |

Introduction

1

Write introduction (RED)

notes for the introduction

- ▶ observation of non-zero neutrino masses indicates likely existence of new physics beyond the standard model
- ▶ multiple SM neutral fermions (right handed) could explain the neutrino masses and their smallness
- ▶ if they are heavy enough to not be produced in oscillations, they are called heavy neutral leptons
- ▶
- ▶ In 1984 the PS191 [G. Bernardi et al., Phys. Lett. B 166, 479 (1986), G. Bernardi et al., Phys. Lett. B 203, 332 (1988)] experiment at CERN appears to have been the earliest beam dump to report HNL bounds from the direct production and decay.
- ▶

The neutrino was postulated by Wolfgang Pauli [1] in 1930 to explain the continuous energy spectrum of electrons originating from beta decay. Cowan and Reines confirmed this prediction of a light, neutral particle in 1956 when they discovered the electron neutrino using inverse beta decay [2]. Two additional neutrino flavors were found in the following years, and with the discovery of the muon neutrino in 1962 [3] and the tau neutrino in 2001 [4], the current theory of neutrinos in the standard model (SM) was established.

Although neutrinos were first believed to be massless, experimental evidence showing the existence of mixed neutrino states started to appear in the 1960s [5]. Mixing between different physical representations of neutrinos is proof for differences in their masses. The resulting phenomenon of neutrino oscillations can be incorporated into the standard model by extending it to include massive neutrinos. How massive they are and how strong is the mixing between neutrino states has to be obtained from measurement. Today there are a variety of precision oscillation experiments using solar, reactor and atmospheric neutrinos to tighten the constraints on the neutrino oscillation parameters. IceCube is one of those leading experiments probing the oscillation theory with atmospheric neutrinos.

The IceCube Neutrino Observatory [6] was constructed between 2004 and 2010 at the geographic South Pole. It is the first cubic kilometer Cherenkov neutrino detector and consists of 5160 optical sensors attached to 86 strings, drilled down to a maximum depth of ~ 2500 m into the Antarctic ice. Neutrinos are detected by the Cherenkov light that is emitted by secondary particles produced in neutrino-nucleon scattering interactions in the ice. With DeepCore, a more densely instrumented sub-array of IceCube, the neutrino detection energy threshold can be lowered to approximately 5 GeV.

At these energies, the similarity in event signatures poses difficulties in identifying different neutrino flavor interactions. Muon neutrino charged-current interactions produce light tracks as opposed to charged-current interactions of electron and tau neutrinos as well as neutral-current interactions

[1]: Pauli (1978), "Dear radioactive ladies and gentlemen"

[2]: Cowan et al. (1956), "Detection of the Free Neutrino: a Confirmation"

[3]: Danby et al. (1962), "Observation of High-Energy Neutrino Reactions and the Existence of Two Kinds of Neutrinos"

[4]: Kodama et al. (2001), "Observation of tau neutrino interactions"

[5]: Davis et al. (1968), "Search for Neutrinos from the Sun"

[6]: Aartsen et al. (2017), "The IceCube Neutrino Observatory: instrumentation and online systems"

of all neutrinos that produce light cascades. The sparse instrumentation of IceCube makes it more challenging to separate track- and cascade-like events. In this thesis, a novel method to distinguish those two event types is developed. In contrast to previously used univariate separation techniques, the multivariate machine learning method applied here maximizes the use of information from the detector response. Through the use of a Gradient Tree Boosting algorithm the separation of events in track and cascade is improved. As a result of the improved separation, the uncertainty to the atmospheric neutrino oscillation parameters Δm_{32}^2 and θ_{23} is significantly reduced.

Standard Model Neutrinos and Beyond

2

2.1 The Standard Model

The *Standard Model (SM)* of particle physics is a Yang-Mills theory [7] providing very accurate predictions of weak, strong, and *electromagnetic (EM)* interactions. It is a relativistic quantum field theory that relies on gauge invariance, where all matter is made up of fermions, which are divided into quarks and leptons, and bosons describe the interactions between the fermions that have to fulfil the overall symmetry of the theory. Leptons are excitations of Dirac-type fermion fields.

The initial idea of the theory is associated with the works of Weinberg [8], Glashow [9], and Salam [10], that proposed a unified description of EM and weak interactions as a theory of a spontaneously broken $SU(2) \times U(1)$ symmetry for leptons, predicting a neutral massive vector boson Z^0 , a massive charged vector boson W^\pm , and a massless photon γ as the gauge bosons. The Higgs mechanism [11], describing the breaking of the symmetry, predicts the existence of an additional scalar particle, the Higgs boson, giving the W^\pm and Z^0 bosons their mass. The Higgs boson was discovered in 2012 at the LHC [12, 13].

Gell-Mann and Zweig proposed the quark model in 1964 [14, 15], which was completed by the discovery of non-abelian gauge theories [16] to form the $SU(3)$ symmetry of the strong interaction called *quantum chromodynamics (QCD)*. QDC describes the interaction between quarks and gluons which completed the full picture of the SM in the mid-1970s. Together with the electroweak theory, the SM is a $SU(3)_C \times SU(2)_L \times U(1)_Y$ local gauge symmetry, with the conserved quantities C , *color*, L , *left-handed chirality*, and Y , *weak hypercharge*.

In the following, the basic properties of the SM are described, following the derivations of [17, 18].

2.1.1 Fundamental Fields

Fermions in the SM are Weyl fields with either *left-handed (LH)* or *right-handed (RH)* chirality, meaning they are eigenvectors of the chirality operator γ_5 with $\gamma_5 \psi_{R/L} = \pm \psi_{R/L}$. Only LH particles transform under $SU(2)_L$. The Higgs field is a complex scalar field, a doublet of $SU(2)_L$, which is responsible for the spontaneous symmetry breaking of $SU(2)_L \times U(1)_Y$ to $U(1)_{\text{EM}}$. Local gauge transformations of the fields are given by

$$\psi \rightarrow e^{ig\theta^a(x)T^a} \psi , \quad (2.1)$$

where g is the coupling constant, $\theta^a(x)$ are the parameters of the transformation, and T^a are the generators of the group, with a counting them. The number of bosons is dependent on the generators of the symmetry groups, while the strength is defined by the coupling constants. There are eight massless gluons corresponding to the generators of the $SU(3)_C$ group. These

| | | |
|-----|--|----|
| 2.1 | The Standard Model | 3 |
| 2.2 | Beyond the Standard Model | 5 |
| 2.3 | Atmospheric Neutrinos as Source of Heavy Neutral Leptons | 12 |

[7]: Yang et al. (1954), "Conservation of Isotopic Spin and Isotopic Gauge Invariance"

[8]: Weinberg (1967), "A Model of Leptons"

[9]: Glashow (1961), "Partial-symmetries of weak interactions"

[11]: Higgs (1964), "Broken symmetries, massless particles and gauge fields"

[12]: Chatrchyan et al. (2012), "Observation of a New Boson at a Mass of 125 GeV with the CMS Experiment at the LHC"

[13]: Aad et al. (2012), "Observation of a new particle in the search for the Standard Model Higgs boson with the ATLAS detector at the LHC"

[14]: Gell-Mann (1964), "A Schematic Model of Baryons and Mesons"

[15]: Zweig (1964), "An $SU(3)$ model for strong interaction symmetry and its breaking. Version 2"

[17]: Giunti et al. (2007), *Fundamentals of Neutrino Physics and Astrophysics*

[18]: Schwartz (2013), *Quantum Field Theory and the Standard Model*

mediate the strong force which conserves color charge. The W_1, W_2, W_3 , and B boson fields of the $SU(2)_L \times U(1)_Y$ group are mixed into the massive bosons through spontaneous symmetry breaking as

$$W^\pm = \frac{1}{\sqrt{2}}(W_1 \mp iW_2) \quad (2.2)$$

and

$$Z^0 = \cos \theta_W W_3 - \sin \theta_W B, \quad (2.3)$$

with θ_W being the *Weinberg angle*. The massless photon field is given by

$$A = \sin \theta_W W_3 + \cos \theta_W B \quad (2.4)$$

and its conserved quantity is the EM charge Q , which depends on the weak hypercharge, Y , and the third component of the weak isospin, T_3 , as $Q = T_3 + Y/2$.

| | Type | | | Q |
|---------|---------|-----------|------------|------|
| quarks | u | c | t | +2/3 |
| | d | s | b | -1/3 |
| leptons | ν_e | ν_μ | ν_τ | 0 |
| | e | μ | τ | -1 |

Table 2.1: Fermions in the Standard Model. Shown are all three generations of quarks and leptons with their electric charge Q .

Fermions are divided into six quarks and six leptons. Weak, strong, and EM force act on the quarks, and they are always found in bound form as baryons or mesons. Leptons do not participate in the strong interaction and only the electrically charged leptons are massive and are effected by the EM force, while neutrinos are massless and only interact via the weak force. Each charged lepton has an associated neutrino, which it interacts with in *charged-current (CC)* weak interactions, that will be explained in more detail in Section 2.1.4. The fermions are listed in Table 2.1.

2.1.2 Electroweak Symmetry Breaking

To elaborate the process of spontaneous symmetry breaking through which the gauge bosons of the weak interaction acquire their masses, the Lagrangian of the Higgs field is considered as

$$\mathcal{L}_{\text{Higgs}} = (D_\mu \Phi^\dagger)(D^\mu \Phi) - \lambda \left(\Phi^\dagger \Phi - \frac{v^2}{2} \right)^2, \quad (2.5)$$

with parameters λ and v , where λ is assumed to be positive. Φ is the Higgs doublet, which is defined as

$$\Phi = \begin{pmatrix} \Phi^+ \\ \Phi^0 \end{pmatrix}, \quad (2.6)$$

with the charged component Φ^+ and the neutral component Φ^0 . The covariant derivative is given by

$$D_\mu = \partial_\mu - ig_2 \frac{\sigma^i}{2} W_\mu^i - \frac{1}{2}ig_1 B_\mu, \quad (2.7)$$

with the Pauli matrices σ^i and the gauge boson fields W_μ^i and B_μ of the $SU(2)_L$ and $U(1)_Y$ groups, respectively. The coupling constants g_2 and g_1 are the respective coupling constants which are related to the Weinberg angle as $\tan \theta_W = \frac{g_1}{g_2}$. The Higgs potential has a non-zero *vacuum expectation value (vev)* at the minimum of the potential at $\Phi^\dagger \Phi = \frac{v^2}{2}$. Since the vacuum is electrically neutral, it can only come from a neutral component of the Higgs

doublet as

$$\Phi_{\text{vev}} = \frac{1}{\sqrt{2}} \begin{pmatrix} 0 \\ v \end{pmatrix}. \quad (2.8)$$

2.1.3 Fermion Masses

The mass term for charged fermions with spin-1/2 is given by

$$\mathcal{L}_{\text{Dirac}} = m(\bar{\Psi}_R \Psi_L - \bar{\Psi}_L \Psi_R), \quad (2.9)$$

composed of the product of left- and right-handed Weyl spinors $\Psi_{L/R}$. This term is not invariant under $SU(2)_L \times U(1)_Y$ gauge transformations, but adding a Yukawa term

$$\mathcal{L}_{\text{Yukawa}} = -Y^e \bar{L}_L \Phi e_R + h.c., \quad (2.10)$$

coupling the fermion fields e_R to the Higgs field Φ , recovers the invariance and gives the fermions their masses. Here, Y^e is the Yukawa coupling constant and \bar{L}_L is the $SU(2)_L$ doublet. With the vev, this results in the mass term for the charged leptons and down-type quarks of $-m_e(\bar{e}_L e_R + \bar{e}_R e_L)$ with $m_e = \frac{Y^e v}{\sqrt{2}}$. With $\tilde{\Phi} = i\sigma_2 \Phi^*$, a similar Yukawa term can be written as $-Y^u \bar{L}_L \tilde{\Phi} u_R + h.c.$, which leads to the masses of the up-type quarks.

2.1.4 Leptonic Weak Interactions after Symmetry Breaking

After the spontaneous symmetry breaking, the leptonic part of the electroweak Lagrangian can be written as

$$\begin{aligned} \mathcal{L}_{\text{EW}}^\ell &= \frac{g}{\sqrt{2}} W^+ \sum_{\alpha=e,\mu,\tau} \bar{\nu}_\alpha \gamma^\mu P_L \ell_\alpha + \frac{g}{4c_w} Z \\ &\times \left\{ \sum_{\alpha=e,\mu,\tau} \bar{\nu}_\alpha \gamma^\mu P_L \nu_\alpha + \sum_\alpha \bar{\ell}_\alpha \gamma^\mu [2s_w^2 P_R - (1 - 2s_w^2) P_L] \ell_\alpha \right\} + h.c., \end{aligned} \quad (2.11)$$

where $c_w \equiv \cos \theta_w$, $s_w \equiv \sin \theta_w$, P_L and P_R are the left and right projectors, respectively, while ν_α and ℓ_α are the neutrino and charged lepton weak eigenstates. The W^\pm and Z bosons are the massive gauge bosons of the weak interaction. The large boson masses $m_W \sim 80 \text{ GeV}$ and $m_Z \sim 90 \text{ GeV}$ result in a short range of the force of about $1 \times 10^{-18} \text{ m}$. Interactions carried out by the W^\pm bosons are called *charged current (CC)* interactions, as they propagate a charge, therefore changing the interacting lepton to its charged/neutral counterpart. *Neutral current (NC)* interactions are those mediated by the Z^0 boson, where no charge is transferred. NC interactions couple neutrinos to neutrinos and charged leptons to charged leptons, but not to each other. The Feynman diagrams for CC and NC interactions are shown in Figure 2.1.

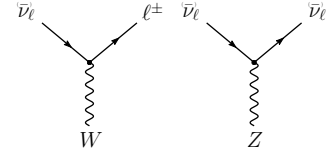


Figure 2.1: Feynman diagrams of charged-current (left) and neutral-current (right) neutrino weak interactions, taken from [19].

Plot is missing + for W and 0 for Z boson. (RED)

2.2 Beyond the Standard Model

The fundamentals of the SM described above are not enough to explain all observed phenomena. Gravity cannot be explained by the SM, as it is incompatible with general relativity, neither can some of the cosmological observations like dark matter, and the matter-antimatter asymmetry be explained. But most importantly, the SM does not predict neutrinos to

have mass, which is experimentally proven by neutrino oscillations, so some extension to the SM is needed in order to explain the observed phenomena.

Cite and/or sidenote this.
(RED)

Standard cosmology (Λ CDM) assumes that equal amounts of matter and anti-matter were produced in the early universe. However, the universe today is dominantly made up of matter. This so-called *baryon asymmetry* can be measured by the difference between the number densities of baryons and anti-baryons normalized to the number density of photons as

$$\eta_B = \frac{n_B - n_{\bar{B}}}{n_\gamma} , \quad (2.12)$$

cite this (RED)

where n_B , $n_{\bar{B}}$, and n_γ are the number densities of baryons, anti-baryons, and photons, respectively. Baryons are the dominant component with η_B being observed to be around 6×10^{-10} . Leptogenesis and EW baryogenesis are scenarios that could explain this phenomenon, where the former could be realized by the existence of heavy RH neutrinos.

- [5]: Davis et al. (1968), "Search for Neutrinos from the Sun"
- [20]: Fukuda et al. (1998), "Evidence for Oscillation of Atmospheric Neutrinos"
- [21]: Ahmad et al. (2002), "Direct Evidence for Neutrino Flavor Transformation from Neutral-Current Interactions in the Sudbury Neutrino Observatory"
- [22]: Alam et al. (2021), "Completed SDSS-IV extended Baryon Oscillation Spectroscopic Survey: Cosmological implications from two decades of spectroscopic surveys at the Apache Point Observatory"
- [23]: Aghanim et al. (2020), "Planck2018 results: VI. Cosmological parameters"
- [24]: Aker et al. (2022), "Direct neutrino-mass measurement with sub-electronvolt sensitivity"

highlight a few more neutrino related open questions, to circle back to related to the HNL searches maybe? (YEL-Low)

The observation of neutrino flavor conversions and neutrino oscillations in a multitude of experiments [5, 20, 21] is the strongest evidence for physics beyond the SM measured in laboratories to date. The observation that neutrinos change their flavor while they propagate through space can only be explained, if at least two neutrinos have a non-zero mass. From those measurements we know the mass differences are very small as compared to the lepton masses, but neither their existence, nor their smallness is predicted by the SM. There are upper limits on the sum of all neutrino masses from cosmological observations at 1.2 eV [22, 23] and at 0.8 eV from the KATRIN experiment [24]. Adding RH neutrino states to the theory could explain the origin of the observed non-zero neutrino masses and could be tested for by searching for corresponding signatures in experiments.

2.2.1 Mass Mechanisms

Since there are no RH neutrinos in the SM, the mass mechanism described in Section 2.1.3, which couples the Higgs field to LH and RH Weyl fields, predicts the LH neutrinos to be massless. From experimental observations it is known that at least two of the three neutrino generations need to have a non-zero mass. Assuming the existence of RH neutrino fields ν_R , one way of producing the neutrino masses is by adding a Yukawa coupling term similar to the one for up-type quarks mentioned in Section 2.1.3, to write the full Yukawa Lagrangian as

$$\mathcal{L}_{\text{Yukawa}} = -Y^e_{ij} \bar{L}_L^i \Phi e_R^j - Y^\nu_{ij} \bar{L}_L^i \tilde{\Phi} \nu_R^j + h.c. , \quad (2.13)$$

with i, j running over the three generations of leptons e, μ , and τ , and Y^e and Y^ν being the Yukawa coupling matrices. Diagonalizing the Yukawa coupling matrices through unitary transformations U^e and U^ν leads to the **Dirac mass term** in the mass basis as

$$\mathcal{L}_{\text{Dirac}}^{\text{mass}} = \frac{v}{\sqrt{2}} (\bar{e}_L M_e e_R - \bar{\nu}_L M_\nu \nu_R) , \quad (2.14)$$

where M_e and M_ν are the diagonal mass matrices of leptons and neutrinos, respectively. A purely Dirac mass term would not explain the smallness of

the neutrino masses in a straightforward way. Only fine-tuning the Yukawa coupling constants to small values would lead to small neutrino masses.

An additional way of generating neutrino masses is by adding a Majorana mass term of the form

$$\mathcal{L}_{\text{Majorana}} = -\frac{1}{2} M_{ij} (\nu_R^i)^c \nu_R^j + h.c., \quad (2.15)$$

with M_{ij} being the Majorana mass matrix and the indices i, j running over all n_R RH neutrino generations. The superscript c denotes the charge conjugate field. Combining the charge conjugated RH neutrino fields with the LH neutrino fields as

$$\mathbf{N} = \begin{pmatrix} \nu_L \\ \nu_R^c \end{pmatrix}, \quad (2.16)$$

with ν_R containing the n_R RH fields. The full neutrino mass Lagrangian is then given by the combined **Dirac and Majorana mass term** as

$$\mathcal{L}_{\text{Dirac+Majorana}}^{\text{mass},\nu} = \frac{1}{2} \mathbf{N}^T \hat{C} M^{\text{D+M}} \mathbf{N} + h.c., \quad (2.17)$$

and the mass matrix is given by

$$M^{\text{D+M}} = \begin{pmatrix} 0 & (M^D)^T \\ M^D & M^R \end{pmatrix}. \quad (2.18)$$

On top of explaining the origin of neutrino masses itself, a combined Dirac and Majorana mass term could also solve the question of their smallness. If the mass of the RH neutrinos is very large, the masses of the active neutrino flavors is suppressed, which is known as *see-saw mechanism*.

minimal scenario needed to explain the two observed non-zero SM neutrino masses is two RH neutrinos

mixing between mass and flavor eigenstates is then described by a 5x5 mixing matrix

2.2.2 Observational Avenues for Right-Handed Neutrinos

if the RH neutrinos have masses at the eV scale, they can be observed through variations in neutrino oscillation experiments as was done in OscNext and MEOWs analysis in IceCube and they could explain the observed anomalies in xyz (take some info from Alex), cite alex thesis for a more thorough overview?

I need to explain the SM PMNS matrix before this, otherwise I'm missing that here.. (RED)

cite these and add some more (RED)

heavy RH neutrinos, also known as heavy neutral leptons, are too massive to be produced in oscillations and would have to be searched for in direct production and decay experiments that will be discussed in more detail in the following

2.2.3 Searching for Heavy Neutral Leptons

Colliders

LHC: proton-proton collider $\text{sqrt}(s)$: 7, 8, 13

ATLAS/CMS: nearly hermetic detectors around interaction, multiple searches for HNL scenarios LHCb: forward detector, designed to search for new particles in decays of heavy hadrons

Type I Seesaw Results:

HNL production in GeV range from : decays of heavy mesons, tau leptons, W bosons, H bosons, or top quarks HNL decays: to lepton number conserving (dirac), or lepton number conserving and violating channels (majorana), depending on mass and mixing parameters, prompt and displaced decays are possible

Atlas results set constraints on mixing with e and mu:

Atlas in minimal extension: 10^{-6} with $|U_{\mu 4}|^2$ at 4-10 GeV same for CMS: 10^{-5} with $|U_{\mu 4}|^2$ and $|U_{e 4}|^2$ at 10-600 GeV

CMS: final state of 3 leptons (two opposite charged and nu) giving $|U_{\mu 4}|^2$
 $4 * 10^{-7}$ at 8-14 GeV

the above mentioned (strong) constraints are mostly based on a model with one HNL coupling to one flavor in type 1 seesaw at least 2 are needed to see the two SM nu masses, both coupling to several flavors it was shown (cite) that re-interpreting these results with more than one HNL can lead to much weaker constraints and to compare results, the assumed model and couplings have to be considered the strong reduction in constraints is due to the opening of new channels, to which the search may not be sensitive

more complex scenarios are possible and might produce various signatures, but are harder to measure: extended gauge symmetries, effective field theories

type III seesaw (HNL as SM EW triplets) can be observed as they are produced in pairs (no active-sterile mixing needed) and result in multi lepton states and high pt jets -> strong exclusion of masses below 790 GeV

LHCb: low mass and high mass results (above below mW), competitive in low mass

low mass channel: $B^+ \rightarrow \mu^+ N \rightarrow \pi^+ \mu^-$, at order 10^{-3} for $|U_{\mu 4}|^2$ at 0.5-3.5 GeV

high mass channel: $W^+ \rightarrow \mu^+ \mu^- + \text{jet}$, at order $10^{-3} \cdot 10^{-2} / 10^{-4} \cdot 10^{-3}$ for $|U_{\mu 4}|^2$ at 5-50 GeV for LNC/LNV

there is a shit ton of future colliders and/or experiments at the LHC planned, that have sensitivities to HNLs.. think about which/how to discuss them

Nuclear Decay

novel approach to search for HNLs through energy-momentum conservation measurements in nuclear reactions

mixing of HNL with electron nu/nubar would cause irregularities, interpretable as limits in $|U_{e 4}|^2$ and m4

Beta Decay detect kinks in the energy spectra at $Q - m_4 c^2$

m_4 probable between energy detection threshold and Q value of the decay

tritium 3H: $Q=18.6$ keV

planned analysis in KATRIN and TRISTAN (1 to 18 keV mass) projected statistical upper limits (95) around $10^{-7} |U_{e4}|^2$ (but will need detector upgrades)

in Project 8 measure the absolute neutrino mass using cyclotron radiation emission spectroscopy (CRES), may also be able to search for HNLs

atmospheric argon 39Ar: $Q=565$ keV

DUNE: massive LArTPCs at long baseline (1300km) accelerator nu (1GeV), measure ionization charge of 39Ar beta decays: projected sensitivity in 20kev to 450keV mass range for $|U_{e4}|^2$ at 10^{-7} (requires substantial trigger development), without more like 10^{-5}

Electron Capture requires total energy-momentum reconstruction of non nu final states in electron capture

e capture: pure 2-body decay of recoiling atom and electron neutrino (mono energetic) measuring atom and associated de-excitation xray or auger electron, energy momentum conservation can be probed

separated non-zero missing mass peak would indicate HNL mixing with the electron neutrino/antineutrino

BeEST experiment: 100-850 keV mass, 7Be ($Q=862$ keV), previous results at $10^{-4} |U_{e4}|^2$, future sensitivity at $10^{-7} |U_{e4}|^2$ after upgrades to the experiment

(proposed) HUNTER experiment: 20-300 keV mass (K-capture of 131Cs), "significantly improve current limits"

Reactor Searches MeV masses (up to 12) at short baseline reactor experiments (commercial or research reactors)

source of electron antineutrinos, therefore also HNL (if they mix)

visible channels: N to nu e+ e-, and N to nu gamma, nu gamma gamma, where the first dominates

pioneering analysis reports $10^{-4} |U_{e4}|^2$ at 2-7 MeV mass range

many experiments exist at 5-25 meters from reactor core, at 100 MW research or 1 GW commercial reactors and 1-5 m³ volume detectors.. these are designed to address reactor anomaly, but could most likely also probe decay in flight to electron positron

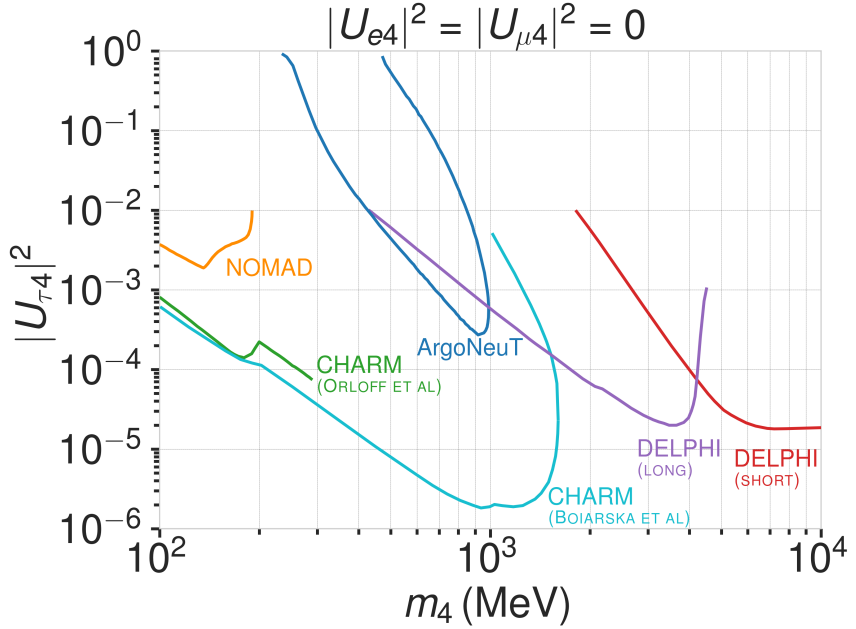


Figure 2.2: Current $|U_{\tau 4}|^2 - m_4$ limits from NOMAD [25], ArgoNeut [26], CHARM [27, 28], and DELPHI [29].

Extracted Beamlines

protons interacting with a target or a beam dump can produce pions, kaons, and heavy-quark hadrons, which can decay to neutrinos and HNLs

HNLs from those interactions can have energies of 1 MeV to 5 GeV and decay at long distances, because of their long lifetimes (model dependent)

experiments using a spectrometer with particle identification can detect unique decay signatures at displaced vertices

the observable signature is just a displaced vertex from for example N to 1 pi, N to l+ l-, N to nu pi0 etc., which cannot be explained by SM neutrinos, without scattering process (not sufficient mass)

depending on the decay channel, a specific mixing can be probed

the other way of searching for HNLs with this is to look for peaks in the missing mass spectrum at the production vertex (at target)

HNL search pioneer work was done by experiments at extracted beam lines, with early results from PS191, CHARM, NOMAD reporting bounds from direct production and decay of HNLs

today there is a large activity of searches for HNLs at extracted beamlines and the strongest bounds on decays are by recent results at PIENU [24, 25], NA62 [28, 29], T2K [36, 514], MicroBooNE [515, 516], and ArgoNeuT [517] experiments

as a standard, the results are presented with only one non-zero mixing parameter at a time

show strongest limits for all three mixings?

Atmospheric and Solar

natural sources of neutrinos up to 20 MeV (solar) and 100s of GeV (atmospheric)

both provide all flavors because of mixing/oscillations and can therefore be used to probe mixing with ν_e , $\nu_{\mu\mu}$, and $\nu_{t\bar{t}}$

depending on the mass and mixing, which govern the decay length, different signatures can be used to probe large parts of the phase space

depending on the type of coupling (just mass-mixing, or more complicated like dipole-portal) considered, the scales could be different

Production in the Sun if the HNL lifetimes are large enough, they could reach the detector after being produced in the sun

this will only allow production through non-zero $|U_{e4}|^2$ and not the other mixings

measurements of the decay to e+ e- nu and comparing to the expected inter-planetary positron flux as was done in Borexino lead to the strongest limits in the few MeV regime

KAMLAND and Super-K could potentially also search for this through the inverse beta decay

Upscatter outside of the Detector for HNL decay length scales of the order of the Earth's diameter, the HNLs could be upscattered anywhere in the earth from the solar or atmospheric neutrino fluxes and decay in the detector

for masses below 18 MeV, limits were derived in [37] R. Plestid (2020), 2010.04193 and [585] R. Plestid (2020), 2010.09523 (just tau-coupled for mixing and all flavor for dipole-portal) and decay in Borexino

in principle this could also be possible for atmospheric neutrinos, but flux and oscillation have to be taken into account

direct production of HNLs in the atmosphere is also possible, but has not been investigated yet

Production and Decay in the Detector If HNL decay lengths are sufficiently short, production and decay could happen in the detector and the observation of two vertices could be used to constrain the mixing parameters

in principle mixing with any neutrino flavor produced in the sun or the atmosphere could be probed and theoretical studies have been performed for mass-mixing and dipole-portal couplings for IceCube and Super-K, Hyper-K, Dune

expand a bit more, or just jump to my section?

Cosmological and Astrophysical

leave these out for the moment?

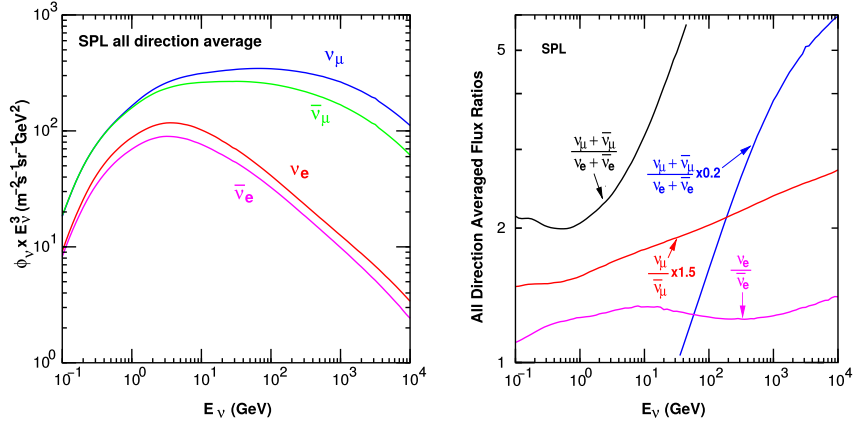


Figure 2.3: The atmospheric fluxes of different neutrino flavors as a function of energy (left) and the ratios between muon neutrinos and electron neutrinos as well as the ratios between neutrinos and antineutrinos for both those flavors (right). Results from the calculations performed for the geographic South Pole, taken from [31].

2.3 Atmospheric Neutrinos as Source of Heavy Neutral Leptons

2.3.1 Production of Neutrinos in the Atmosphere

[30]: Tanabashi et al. (2018), “Review of Particle Physics”

The analysis performed in this work is based on the sample of neutrinos observed in IceCube DeepCore at energies below 100 GeV. At these energies, the flux exclusively originates in the Earth’s atmosphere. Highly relativistic cosmic rays (protons and heavier nuclei [30]) interact in the upper atmosphere, producing showers of secondary particles. Neutrinos are produced in decays of charged pions and kaons (π and K mesons) present in those showers, where the dominant contribution comes from the decay chain

$$\begin{aligned} \pi^\pm &\rightarrow \mu^\pm + \nu_\mu (\bar{\nu}_\mu) , \\ \mu^\pm &\rightarrow e^\pm + \bar{\nu}_\mu (\nu_\mu) + \nu_e (\bar{\nu}_e) , \end{aligned} \quad (2.19)$$

where muon neutrinos ν_μ and muons μ^\pm are produced in the first decay and both electron and muon neutrinos $\nu_{e/\mu}$ are produced in the second decay. Atmospheric muons, which are also produced in these decays, are the main background component for IceCube DeepCore analyses.

The different atmospheric flux components are shown in Figure 2.3 (left), for a much broader energy range than relevant for this work. Both neutrinos and antineutrino fluxes are shown for electron and muon neutrinos and all fluxes are the directionally averaged expectation calculated at the South Pole. Muon neutrinos are dominating the flux and from Equation 2.19 the naive assumption would be that the ratio between muon and electron neutrinos is $(\nu_\mu + \bar{\nu}_\mu) / (\nu_e + \bar{\nu}_e) = 2$. This is roughly true at energies below 1 GeV, where all muons decay in flight, but at larger energies muons can reach the detector before decaying, which increases the ratio to approximately 10:1 at around 100 GeV. Additionally, kaon decays start to contribute which also increases the number of muons and muon neutrinos. The increasing ratio can be seen in Figure 2.3 (right), which also shows the ratio between neutrinos and antineutrinos for both flavors.

Charged mesons or tau particles can also be produced in cosmic ray interactions. Their decays lead to the production of tau neutrinos. At the energies relevant for this work however, the resulting tau neutrino flux is negligible as compared to the muon neutrino flux [32] and is not considered in the analysis. This is because both charged mesons and tau particles are much

[32]: Fedynitch et al. (2015), “Calculation of conventional and prompt lepton fluxes at very high energy”

heavier than pions and kaons and therefore their production is suppressed at high energies.

2.3.2 Oscillations

Say something about atmospheric neutrino flux uncertainties, based on recent JP/Anatoli papers. (YELLOW)

So far we have described neutrinos in their flavor eigenstates, which are relevant for weak interactions. In the SM three-neutrino model the weak flavor states are ν_e , ν_μ , and ν_τ , which relate them to the charged leptons they interact with in CC interactions. There is a second way of describing neutrino wave functions based on their Hamiltonian eigenvalues [33], namely as the mass eigenstates ν_1 , ν_2 , and ν_3 . These states are related to the flavor eigenstates by the unitary, 3x3 Pontecorvo-Maki-Nakagawa-Sakata (PMNS) matrix U , where the flavor states are a superposition of the mass states as

$$|\nu_\alpha\rangle = \sum_k U_{\alpha k}^* |\nu_k\rangle , \quad (2.20)$$

with the weak flavor states $|\nu_\alpha\rangle$, $\alpha = e, \mu, \tau$, and the mass states $|\nu_k\rangle$ with $k = 1, 2, 3$. The mixing matrix can be parameterized as [30]

$$U = \begin{pmatrix} 1 & 0 & 0 \\ 0 & c_{23} & s_{23} \\ 0 & -s_{23} & c_{23} \end{pmatrix} \begin{pmatrix} c_{13} & 0 & s_{13}e^{-i\delta_{CP}} \\ 0 & 1 & 0 \\ -s_{13}e^{i\delta_{CP}} & 0 & c_{13} \end{pmatrix} \begin{pmatrix} c_{12} & s_{12} & 0 \\ -s_{12} & c_{12} & 0 \\ 0 & 0 & 1 \end{pmatrix}, \quad (2.21)$$

where $c_{ij} = \cos \theta_{ij}$ and $s_{ij} = \sin \theta_{ij}$ are cosine and sine of the mixing angle θ_{ij} , that defines the strength of the mixing between the mass eigenstates i and j , and δ_{CP} is the neutrino CP-violating phase.

[30]: Tanabashi et al. (2018), "Review of Particle Physics"

add current BF values from nufit or so? (YELLOW)

Describing neutrinos in their mass state is crucial to understand their propagation through space and time. Their propagation in vacuum can be expressed by applying a plane wave approach, where the mass eigenstates evolve as

$$|\nu_k(t)\rangle = e^{-iE_k t/\hbar} |\nu_k\rangle . \quad (2.22)$$

The energy of the mass eigenstate $|\nu_k\rangle$ is $E_k = \sqrt{\vec{p}^2 c^2 + m_k^2 c^4}$, with momentum \vec{p} and mass m_k , \hbar is the reduced Planck constant, and c is the speed of light in vacuum. The existence of non-zero, non-equal masses and the neutrino mixing relation in Equation 2.20, lead to the observed phenomenon of neutrino oscillations. Oscillations mean that a neutrino changes from its initial flavor, that it was produced with, to another flavor and back after traveling a certain distance. A neutrino is produced as a flavor eigenstate $|\nu_\alpha\rangle$ in a CC weak interaction, but its propagation happens as the individual mass states it is composed of. The probability of finding the neutrino with initial flavor $|\nu_\alpha\rangle$ in the flavor state $|\nu_\beta\rangle$ after the time t is calculated as

$$P_{\nu_\alpha \rightarrow \nu_\beta}(t) = |\langle \nu_\beta | \nu_\alpha(t) | \nu_\beta | \nu_\alpha(t) \rangle|^2 , \quad (2.23)$$

by applying Fermi's Golden Rule [34], which defines the transition rate from one eigenstate to another by the strength of the coupling between them. This coupling strength is the square of the matrix element and using the fact that the mixing matrix is unitary ($U^{-1} = U^\dagger$) to describe the mass eigenstates as flavor eigenstates, we find the time evolution of the flavor state $|\nu_\alpha(t)\rangle$,

[34]: Dirac (1927), "The Quantum Theory of the Emission and Absorption of Radiation"

which can be inserted into Equation 2.23 to find the probability as

$$P_{\nu_\alpha \rightarrow \nu_\beta}(t) = \sum_{j,k} U_{\beta j}^* U_{\alpha j} U_{\beta k} U_{\alpha k}^* e^{-i(E_k - E_j)t/\hbar}. \quad (2.24)$$

The indices j and k run over the mass eigenstates. We can approximate the energy as

$$E_k \approx E + \frac{c^4 m_k^2}{2E} \longrightarrow E_k - E_j \approx \frac{c^4 \Delta m_{kj}^2}{2E}, \quad (2.25)$$

for small neutrino masses compared to their kinetic energy. Here, $\Delta m_{kj}^2 = m_k^2 - m_j^2$ is the mass-squared splitting between states k and j . Replacing the time in Equation 2.24 by the distance traveled by relativistic neutrinos $t \approx L/c$ we get

$$\begin{aligned} P_{\nu_\alpha \rightarrow \nu_\beta}(t) &= \delta_{\alpha\beta} - 4 \sum_{j>k} \text{Re}(U_{\beta j}^* U_{\alpha j} U_{\beta k} U_{\alpha k}^*) \sin^2\left(\frac{c^3 \Delta m_{kj}^2}{4E\hbar} L\right) \\ &\quad + 2 \sum_{j>k} \text{Im}(U_{\beta j}^* U_{\alpha j} U_{\beta k} U_{\alpha k}^*) \sin^2\left(\frac{c^3 \Delta m_{kj}^2}{4E\hbar} L\right), \end{aligned} \quad (2.26)$$

which is called the survival probability if $\alpha = \beta$, and the transition probability if $\alpha \neq \beta$. Once again, this probability is only non-zero if there are neutrino mass eigenstates with masses greater than zero. Additionally, there must be a mass-squared difference Δm^2 and non-zero mixing between the states. Since we assumed propagation in vacuum in Equation 2.22, the transition and survival probabilities correspond to vacuum mixing.

say something about how
this changes with matter
(YELLOW)

2.3.3 Interactions with Nuclei

The neutrino detection principle of IceCube DeepCore is explained in Chapter 3 and relies on the weak interaction processes between neutrinos and the nuclei of the Antarctic glacial ice. At neutrino energies above 5 GeV, the cross-sections are dominated by *deep inelastic scattering (DIS)*, where the neutrino is energetic enough to resolve the underlying structure of the nucleons and interact with one of the composing quarks individually. As a result the nucleon breaks and a shower of hadronic secondary particles is produced. Depending on the type of interaction, the neutrino either remains in the final state for NC interactions or is converted into its charged lepton counterpart for CC interactions. The CC DIS interactions have the form

$$\begin{aligned} \nu_l + N &\rightarrow l^- + X, \\ \bar{\nu}_l + N &\rightarrow l^+ + X, \end{aligned} \quad (2.27)$$

where $\nu_l/\bar{\nu}_l$ and l^-/l^+ are the neutrino/antineutrino and its corresponding lepton/antilepton, and l can be either an electron, muon, or tau. N is the nucleon and X stands for any set of final state hadrons. The NC DIS interactions are

$$\begin{aligned} \nu_l + N &\rightarrow \nu_l + X \text{ and} \\ \bar{\nu}_l + N &\rightarrow \bar{\nu}_l + X. \end{aligned} \quad (2.28)$$

Figure 2.4 shows the Feynman diagrams for both processes DIS interactions have a roughly linear energy dependent cross-section above ~ 20 GeV and

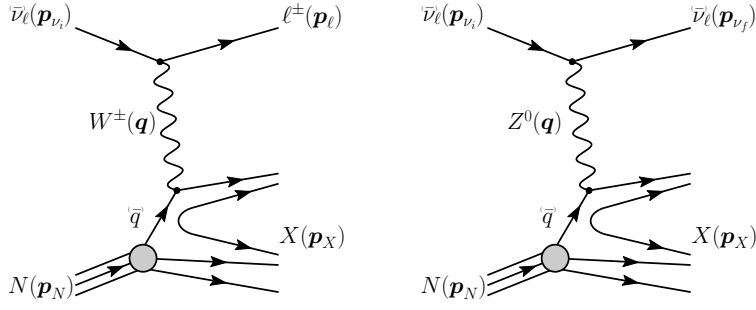


Figure 2.4: Feynman diagrams for deep inelastic scattering of a neutrino with a nucleon via charged-current (left) and neutral current (right) interactions. p_{ν_i} , p_N and p_{ν_f} , p_L , p_N are the input and output four-momenta, while q is the momentum transfer. Taken from [19].

are well measured and easy to theoretically calculate. They are the primary interaction channel for neutrinos detected with IceCube.

At energies below 5 GeV, *quasi-elastic scattering (QE)* and *resonant scattering (RES)* become important. At these energies the neutrinos interact with the approximately point-like nucleons, without breaking them up in the process. RES describes the process of a neutrino scattering off a nucleon producing an excited state of the nucleon in addition to a charged lepton. It is the dominant process at 1.5 GeV to 5 GeV for neutrinos and 1.5 GeV to 8 GeV for antineutrinos. Below 1.5 GeV QE is the main process, where protons are converted to neutrons in antineutrino interactions and vice-versa for neutrino interactions. Additionally, a charged lepton corresponding to the neutrino/antineutrino flavor is produced. The cross-sections of QE and RES scattering processes are not linear in energy and the transition region from QE/RES to DIS is poorly understood. The total cross-sections and their composition is shown in Figure 2.5. It can be seen that the interaction cross-sections are very small at the order of 10^{-38} cm^2 . This is the reason why very large volume detectors are required to measure atmospheric neutrinos with sufficient statistics to perform precision measurements of their properties. The interaction length of a neutrino with $E_\nu = 10 \text{ GeV}$ is of $\mathcal{O}(10 \times 10^{10} \text{ km})$, for example.

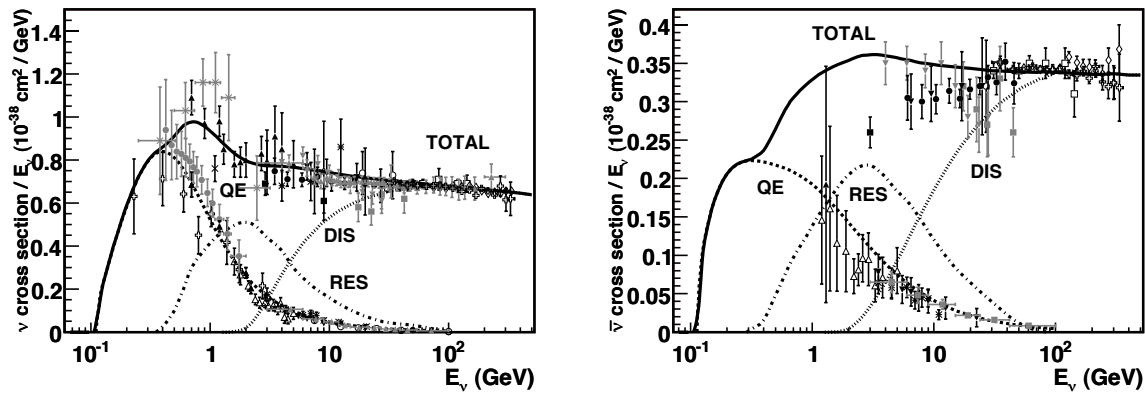


Figure 2.5: Total neutrino (left) and antineutrino (right) per nucleon cross-section divided by neutrino energy plotted against energy. The three main scattering processes quasi-elastic scattering (QE), resonant scattering (RES), and deep-inelastic scattering (DIS) are shown. Taken from [35].

HNL Production and Decay

Up-Scattering in the Ice

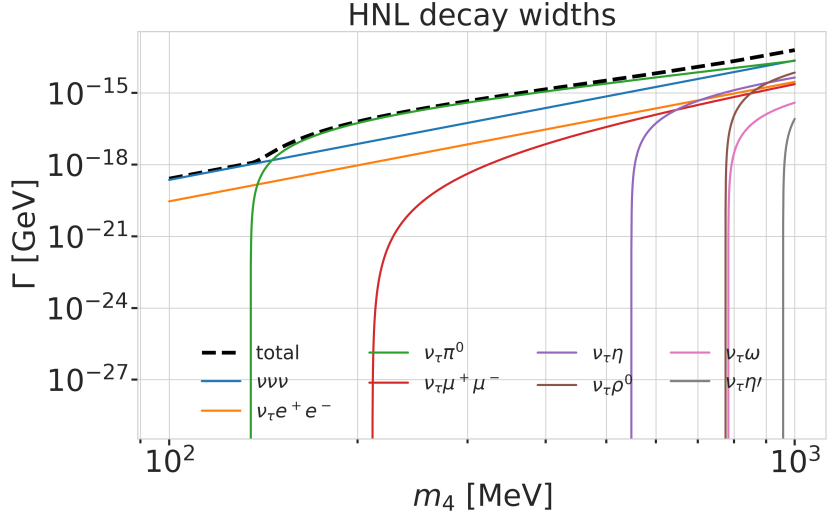


Figure 2.6: Decay widths of the HNL within the mass range considered, calculated based on the results from [36]. Given the existing constraints on $|U_{e4}|^2$ and $|U_{\mu 4}|^2$, we consider that the corresponding decay modes are negligible.

Re-write/re-formulate this section (copied from HNL technote). (RED)

[36]: Coloma et al. (2021), “GeV-scale neutrinos: interactions with mesons and DUNE sensitivity”

Decay in the Ice

To explain the signature we can observe in IceCube we first have to revisit the weak interactions that the HNL inherits from its LH counterpart through mixing. We will be following the derivation in [36]. Extending the SM by n additional RH neutrinos, ν_i ($i = 3 + n$), leads to the mass Lagrangian

$$\mathcal{L}_v^{\text{mass}} \supset - \sum_{\alpha=e,\mu,\tau} \sum_{i=4}^{3+n} Y_{\nu,\alpha i} \bar{L}_{L,\alpha} \tilde{\phi} \nu_i - \frac{1}{2} \sum_{i=4}^{3+n} M_i \bar{\nu}_i \nu_i^c + h.c., \quad (2.29)$$

in a basis where the Majorana mass terms are diagonal. $Y_{\nu,\alpha i}$ are the Yukawa couplings to the lepton doublets and M the Majorana masses for the heavy singlets. $L_{L,\alpha}$ stands for the SM LH lepton doublet of flavor α while ϕ is the Higgs field, and $\tilde{\phi} = i\sigma_2\phi^*$ and $\nu_i^c \equiv C\bar{\nu}_i^t$, with $C = i\gamma_0\gamma_2$ in the Weyl representation. The full neutrino mass matrix with the Higgs vacuum expectation value $v/\sqrt{2}$ reads

$$\mathcal{M} = \begin{pmatrix} 0_{3 \times 3} & Y_\nu v / \sqrt{2} \\ Y_\nu^t v / \sqrt{2} & M \end{pmatrix}, \quad (2.30)$$

and can be diagonalized by a $(3+n) \times (3+n)$ full unitary rotation U , that itself leads to neutrino masses upon diagonalization, additionally manifesting the mixing between active neutrinos and heavy states. The resulting model consists of 3 light SM neutrino mass eigenstates ν_i ($i = 1, 2, 3$) and n heavier states, as introduced above. The flavor states will now consist of a combination of light and heavy states

$$\nu_\alpha = \sum_{i=1}^{3+n} U_{\alpha i} \nu_i, \quad (2.31)$$

and the leptonic part of the EW Lagrangian can be written as

$$\begin{aligned} \mathcal{L}_{\text{EW}}^\ell = & \frac{g}{\sqrt{2}} W_\mu^+ \sum_\alpha \sum_i U_{\alpha i}^* \bar{\nu}_i \gamma^\mu P_L \ell_\alpha + \frac{g}{4c_w} Z_\mu \\ & \times \left\{ \sum_{i,j} C_{ij} \bar{\nu}_i \gamma^\mu P_L \nu_j + \sum_\alpha \bar{\ell}_\alpha \gamma^\mu [2s_w^2 P_R - (1-2s_w^2) P_L] \ell_\alpha \right\} + h.c., \end{aligned} \quad (2.32)$$

while

$$C_{ij} \equiv \sum_{\alpha} U_{\alpha i}^* U_{\alpha j}. \quad (2.33)$$

The indices now sum over all $(3 + n)$ flavor and mass states.

Based on this formulation and assuming that only the mixing with the tau sector is open ($|U_{\alpha 4}^2| = 0, \alpha = e, \mu$), the relevant production diagram of the HNL can be drawn as shown in Figure ???. Alongside the fourth heavy mass state, a Hadronic cascade is produced. The heavy mass state will travel for some distance (dependent on mass and mixing) before it decays. The subsequent decay processes are depicted in Figure ???. It can be a CC or NC decay and both leptonic and mesonic modes are possible (dependent on the mass). This will produce a tau or a tau neutrino and another cascade that can be EM or Hadronic. The branching ratios corresponding to the decay modes of the HNL for the mass range of interest (i.e. between 100 MeV and 1 GeV) are shown in Figure ?? as a function of the HNL mass.

The IceCube Neutrino Observatory

3

The IceCube Neutrino Observatory [6] is a cubic-kilometer, ice-Cherenkov detector located at the geographic South Pole. IceCube utilizes the Antarctic glacial ice as detector medium to observe neutrinos by measuring the Cherenkov light produced from secondary charged particles. It was deployed between 2006 and 2011 and has been taking data since the installation of the first modules. The primary goal of IceCube is the observation of astrophysical neutrinos as a telescope, but it can also be used to study fundamental particle physics properties by measuring atmospheric neutrinos as well as studying cosmic rays.

This chapter first describes the main- and sub-array of the detector and its detection module in Section 3.1, the propagation of particles through ice is explained in Section 3.2, and finally, the signatures that IceCube can observe of the different particles are introduced in Section 3.3.

| | |
|---|----|
| add fancy icecube header | |
| 3.1 Detector Components | 19 |
| picture here (ORANGE) | |
| 3.2 Particle Propagation in Ice | 22 |
| 3.3 Event Morphologies | 25 |

[6]: Aartsen et al. (2017), “The IceCube Neutrino Observatory: instrumentation and online systems”

3.1 Detector Components

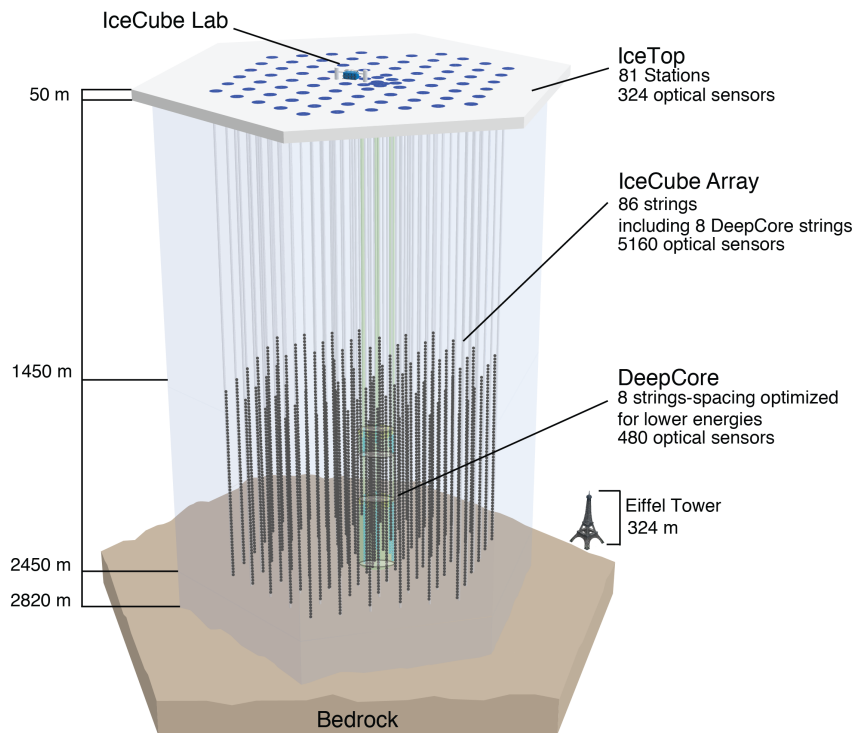


Figure 3.1: Overview of the IceCube detector showing the in-ice main- and sub-array IceCube and DeepCore, IceTop, and the IceCube Laboratory. From [6].

The full IceCube detector array consists of 86 vertical, in-ice strings and 81 surface stations as shown in Figure 3.1. The in-ice part is composed of 60 optical modules per string deployed at depths of 1450 m - 2450 m below the ice, while the surface stations of the cosmic air-shower array, *IceTop*, are ice-filled tanks. The surface stations and the majority of the strings are arranged in a hexagonal grid with the operations building, the *IceCube Laboratory* (ICL), central to the grid on the surface. A top view of the hexagonal arrangement

is shown in Figure 3.4. The in-ice array is designed to detect neutrinos in the energy range from GeV to PeV.

3.1.1 Digital Optical Modules and the Antarctic Ice

[37]: Price et al. (2000), "Age vs depth of glacial ice at South Pole"

SB: there are more properties than just these. Somehow need a half sentence that explains why these are particularly important to single out (see ice papers for inspiration) (ORANGE)

CL: maybe define that absorption and scattering lengths are? they are defined differently so this invites a comparison that is not so obvious (ORANGE)

[38]: Abbasi et al. (2022), "In-situ estimation of ice crystal properties at the South Pole using LED calibration data from the IceCube Neutrino Observatory"

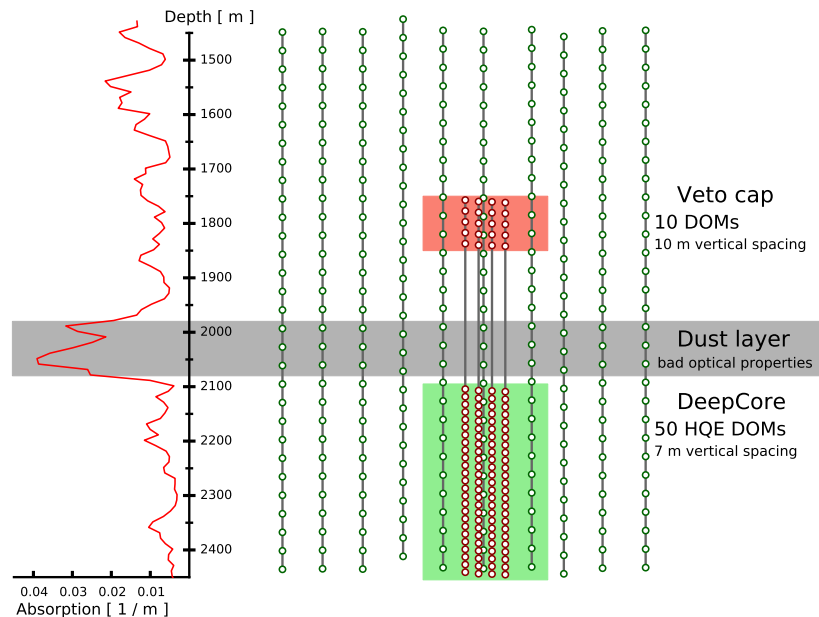
Add reference for the dust layer! Maybe also from the ice paper? mention figure 3.2 side-by-side IceCube and DeepCore showing the depth dependent scattering and absorption lengths (left panel) and the DOM positions around the dust layer.

exchange for figure with scattering (check abs/sca is correct) (ORANGE)

[39]: Abbasi et al. (2009), "The IceCube data acquisition system: Signal capture, digitization, and timestamping"

[39]: Abbasi et al. (2009), "The IceCube data acquisition system: Signal capture, digitization, and timestamping"

The IceCube detection medium is the Antarctic glacial ice itself, which was formed over 100 000 years by accumulation of snow that was subsequently compressed by its own weight to form a dense crystal structure [37]. As a result of this formation process, the optical properties, scattering and absorption, primarily change with depth. Within the detector volume the absorption length ranges from 100 m - 400 m, while the scattering length lies between 20 m and 100 m. They are correlated, with the absorption length being roughly four times the scattering length [38]. The vertical distribution of scattering and absorption length can be seen in Figure 3.2, where one dominant feature is the *dust layer* between 2000 m and 2100 m depth. This region has a higher concentration of dust particles that were deposited in a period of high volcanic activity, which leads to bad optical properties in form of larger scattering and absorption.



The ice is instrumented by 5160 optical sensors called *Digital Optical Modules* (DOMs) [39], which can detect the Cherenkov light produced by charged particles traveling through the ice. Each DOM is made of a spherical glass housing, containing a downward-facing Photomultiplier Tube (PMT), the main-board with control, readout, and processing-electronics, and a LED flasher-board for calibration purposes. The design and the individual components of a DOM can be seen in Figure 3.3.

The majority of PMTs are the 10" Hamamatsu R7081-02, which have a bialkali photocathode and are sensitive to wavelengths in the range of 300 nm to 650 nm, with a peak quantum efficiency of 25% at 390 nm. In the central part of the IceCube array the peak efficiency reaches 34%. The dark count rate in the temperature range of -40°C to -20°C is ~ 300 Hz. The DOM electronics measure the PMT voltage and control the gain. At a voltage crossing of the equivalent to 0.25 PE the waveform readout is activated [39]. Only when

either one of the nearest or next to nearest DOMs above or below also sees a voltage crossing within a $1\text{ }\mu\text{s}$ time window¹, the voltages are digitized and sent to the ICL. Through the application of a waveform unfolding algorithm, called *WaveDeform* [40], the waveforms are compressed, and the results are the reconstructed times and charges of the photo-electrons. This is the basis for all further IceCube data processing.

The PMT is covered with a mu-metal grid (made from wire mesh), shielding the photocathode from Earth's magnetic field, and it is optically coupled to the glass sphere by RTV silicone gel. The glass sphere is a pressure vessel, designed to withstand both the constant ice pressure and the temporary pressure during the refreezing process of the water in the drill hole during deployment (peaking at around 690 bar). The sphere is held by a harness that connects the DOMs along a string and also guides the cable beside them.

The flasher-board controls 12 LEDs that produce optical pulses with a wavelength of 405 nm [6]. The LEDs can be pulsed separately or in combination with variable output levels and pulse lengths. Using the known information of the light source positions and times this can be used for in-situ calibration of the detector by measuring absorption and scattering properties of the ice. Calibrating the absolute efficiency of the DOMs itself is more accurately done using minimum ionizing muons [41, 42], since the total amplitude of the LED light is not well known.

3.1.2 IceCube

The 78 strings that are arranged in a hexagonal pattern from the main part of the in-ice array, which is called *IceCube*. With a $\sim 125\text{ m}$ horizontal spacing between the strings and a $\sim 17\text{ m}$ vertical spacing between DOMs, *IceCube* has a lower energy threshold of around 100 GeV . *IceCube* was designed to detect astrophysical neutrinos with energies above 1 TeV .

The coordinate system that is used in *IceCube* is centered at $46500'\text{E}, 52200'\text{N}$ at an elevation of 883.9 m [6]. Per definition, it's a right-handed coordinate system where the y -axis points along the Prime Meridian (Grid North) towards Greenwich, UK, and the x -axis points 90° clockwise from the y -axis (Grid East). The z -axis is normal to the ice surface, pointing upwards. For *IceCube* analyses depth is defined as the distance along the z axis from the ice surface, assumed to be at an elevation of 2832 m .

3.1.3 DeepCore

The additional 8 strings form a denser sub-array of *IceCube* called *DeepCore* [43]. It's located at the bottom-center of the in-ice array and its *fiducial volume* also includes the 7 surrounding *IceCube* strings as shown in Figure 3.4. The strings in this region have a closer average horizontal distance of about 70 m . The lower 50 DeepCore DOMs on each string are placed in the region of clear ice below the dust layer between 2100 m to 2450 m depth, where their vertical spacing is $\sim 7\text{ m}$. The remaining 10 modules on each string are placed above the dust layer to be used as veto against atmospheric muons as can be seen in Figure 3.2. Additionally, the DeepCore DOMs are equipped with higher quantum efficiency PMTs. The combination of the denser spacing, the high

1: This is referred to as a *hard local coincidence (HLC)* [39].

[40]: Aartsen et al. (2014), "Energy Reconstruction Methods in the IceCube Neutrino Telescope"

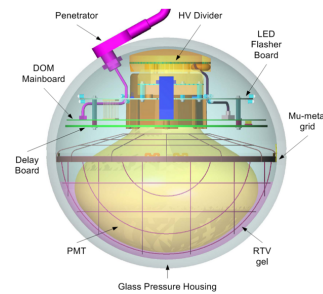


Figure 3.3: Design and components of a Digital Optical Module (DOM) [39]

[6]: Aartsen et al. (2017), "The IceCube Neutrino Observatory: instrumentation and online systems"

[41]: Feintzeig (2014), "Searches for Point-like Sources of Astrophysical Neutrinos with the IceCube Neutrino Observatory"

[42]: Kulacz (2019), "In Situ Measurement of the IceCube DOM Efficiency Factor Using Atmospheric Minimum Ionizing Muons"

Add accuracy of the efficiency calibration here. (ORANGE)

[6]: Aartsen et al. (2017), "The IceCube Neutrino Observatory: instrumentation and online systems"

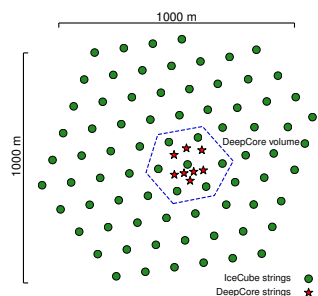


Figure 3.4: Top view of the *IceCube* array.

Blow up this image a bit, so it's better readable as marginfigure. (READ)

[43]: Abbasi et al. (2012), "The design and performance of *IceCube DeepCore*"

CL: value? (YELLOW)

SB: this needs revision.
the energy range you
mention is particular for
oscillations already (at-
mospheric neutrinos are
plentiful outside of this
range you mentioned).
If you rewrite the first
part you'll have to revisit
the second part. Also in
general I'd suggest not to
rank analyses like Main
and Other - DeepCore
was originally intended
as a dark matter detec-
tor, and there are prob-
ably more DM analyses
unblinded / year than
oscillations. Just keep it
general, no need to rank.
(RED)

quantum efficiency modules, and the most favorable ice properties below the dust layer leads to a lower energy detection threshold of around 5 GeV, allowing the more efficient observation of atmospheric neutrinos, which are mostly in the energy range of 10 GeV - 100 GeV. The main analysis performed with DeepCore is an atmospheric neutrino oscillation measurement, but the large flux of atmospheric neutrinos allows for many other Beyond Standard Model searches, such as searches for dark matter, non-standard interactions, or sterile neutrinos.

3.2 Particle Propagation in Ice

Neutrinos interacting in the ice via DIS produce muons, electromagnetic showers, and hadronic showers, depending on their flavor and the interaction type. The particles produced in those processes mainly lose their energy through *ionization*, *bremsstrahlung*, *pair production*, and the *photo-nuclear interaction*. Electrically charged particles also emit Cherenkov light when traveling through the ice, which is the main observable in IceCube, but only contributes a small amount to the total energy loss. The Cherenkov effect and the energy losses of the particles are described in the following sections, followed by an overview of the different particle signatures in IceCube.

3.2.1 Cherenkov Effect

When a charged particle moves through a medium with a velocity that is greater than the speed of light in that medium, it emits Cherenkov radiation, losing a very small amount of energy ($\mathcal{O}(10^{-4})$ of the total energy loss). The detection principle of IceCube DeepCore, is based on the observation of resulting Cherenkov photons that are emitted by the charged secondary particles produced in the neutrino interactions that were introduced in Section ???. The Cherenkov effect was first observed by Pavel Cherenkov in 1934 [44] and occurs when the charged particle travels faster than the phase velocity of light, therefore polarizing the medium. Upon de-excitation the molecules emit the received energy as photons in a spherical wavefront. Since the particle moves past this wavefront, the superposition of the spherical light emissions forms a cone, which is shown in blue in the bottom panel of Figure 3.5.

Using trigonometry, the angle θ_c at which the Cherenkov light is emitted can be calculated as

$$\theta_c = \arccos\left(\frac{1}{\beta n}\right), \quad (3.1)$$

where β is the velocity of the particle in units of the speed of light and n is the refractive index of the medium. When the particle velocity is close to the speed of light, the equation holds and the angle is only dependent on the refractive index of the medium. For the Antarctic ice, the refractive index is $n \approx 1.3$ and as a result $\theta_c \approx 41^\circ$.

The frequency of the emission depends on the charge z and the wavelength-dependent index of refraction $n(\omega)$ and is given by the Frank-Tamm formula [45, 46]

$$\frac{d^2N}{dxd\lambda} = \frac{2\pi\alpha z^2}{\lambda^2} \left(1 - \frac{1}{\beta^2 n(\omega)^2}\right), \quad (3.2)$$

with $\alpha \approx 1/137$ the fine structure constant, λ the wavelength of the emitted light, and x the path length traversed by the particle. Relativistic particles in ice produce roughly 250 photons per cm in the wavelength range of 300 nm - 500 nm [47].

3.2.2 Energy Losses

Even though relativistic, charged particles traveling through matter produce Cherenkov radiation, their energy is mainly lost through other processes that are dependent on the particle type and energy. The exact principles of energy loss for the different types can broadly be categorized into the three groups: quasi-continuous energy loss by muons, electromagnetic cascades, and hadronic cascades.

Muons

Muons lose their energy by ionization, bremsstrahlung, pair production, and the photo-nuclear effect. The energy loss by ionization is the dominant process for muons above 1 GeV and has a weak energy dependence given by

$$\left\langle -\frac{dE}{dx} \right\rangle = a_I(E) + b_R(E) \cdot E , \quad (3.3)$$

where E is the energy and $a_I(E)$ and $b_R(E) \cdot E$ are the energy loss by ionization and the combined radiative losses, respectively. In the energy range relevant for this work (10 GeV - 100 GeV), the parameters a_I and b_R only depend on energy very weakly and can be approximated by constants. The energy loss is then given by

$$\left\langle -\frac{dE}{dx} \right\rangle = a + b \cdot E . \quad (3.4)$$

Based on this description, there is a critical energy which divides the regimes where ionization and radiative losses dominate. The critical energy is given by $E_{\text{crit}} = a/b$ and for muons in ice it is ~ 713 GeV (using $a \approx 2.59 \text{ MeVcm}^{-1}$ and $b \approx 3.63 \times 10^{-6} \text{ cm}^{-1}$ [48]). Since the energy range of interest is well below this critical energy, the range of a muon can easily be related to its energy by

$$\langle L \rangle = \frac{E_0}{a} . \quad (3.5)$$

Measuring the length of a muon track therefore allows for an estimation of its energy if the full track is contained within the instrumented volume of IceCube. Using the given numbers a 30 GeV muon travels ~ 116 m, which is well within the instrumented volume of IceCube, which spans across distances of up to 1000 m. This approximate treatment does not take into account the stochastic nature of some energy losses. Bremsstrahlung and photo-nuclear interactions for example rarely occur, but when they do, they deposit a large chunk of energy. A thorough investigation of the energy losses of muons in ice can be found in [49].

Electromagnetic Showers

Photons as well as electrons and positrons are produced either directly in neutrino interactions or in secondary particle interactions. Above a critical

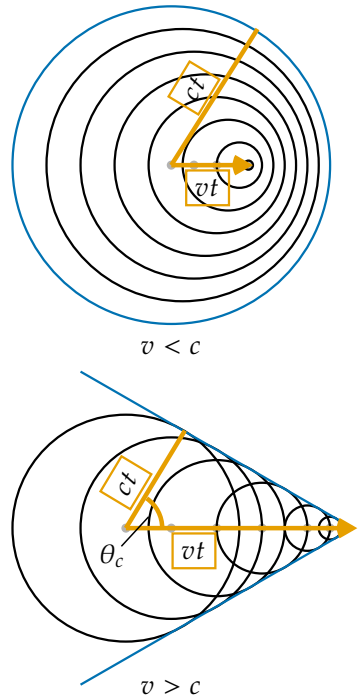


Figure 3.5: Schematic depiction of the spherical light front produced by a particle traveling slower than the speed of light in the medium (top) and the formation of the Cherenkov light front produced by a charged particle traveling faster than the speed of light in the medium (bottom). Blue is the resulting wavefront, while the black circles are spherically emitted light at each position and the orange arrows show the direction of the particle.

Cite n and θ_c (ORANGE)

[45]: Frank et al. (1937), "Coherent visible radiation from fast electrons passing through matter"

[46]: Tamm (1991), "Radiation Emitted by Uniformly Moving Electrons"

[47]: Rädel et al. (2012), "Calculation of the Cherenkov light yield from low energetic secondary particles accompanying high-energy muons in ice and water with Geant4 simulations"

SB: you already mentioned that Cher. Rad. doesn't lead to significant energy loss. I suggest to clean up the text a bit, you don't need to emphasize that so many times. Pick one place (probably here) and eliminate it elsewhere (RED)

Add reference (PDG or find original) (ORANGE)

[48]: Chirkin et al. (2004), "Propagating leptons through matter with Muon Monte Carlo (MMC)"

[49]: Raedel (2012), "Simulation Studies of the Cherenkov Light Yield from Relativistic Particles in High-Energy Neutrino Telescopes with Geant4"

Add reference for these processes. (ORANGE)

[30]: Tanabashi et al. (2018), "Review of Particle Physics"

cite em shower distribution (RED)

gamma (from equation) is not defined (RED)

[49]: Raedel (2012), "Simulation Studies of the Cherenkov Light Yield from Relativistic Particles in High-Energy Neutrino Telescopes with Geant4"

[50]: Agostinelli et al. (2003), "Geant4—a simulation toolkit"

Add angular profile plot (Summer agrees!) (create one based on Leif Rädel as Alex did) (RED)

[49]: Raedel (2012), "Simulation Studies of the Cherenkov Light Yield from Relativistic Particles in High-Energy Neutrino Telescopes with Geant4"

[51]: Gabriel et al. (1994), "Energy dependence of hadronic activity"

energy E_c , they lose their energy through repeated pair production and bremsstrahlung emission forming an expanding, electromagnetic shower profile. The particles' energy reduces with every interaction and their number increases until they fall below the critical energy where ionization and excitation of surrounding atoms become the dominant energy loss processes for electrons and positrons. For photons the remaining energy is lost through the Compton effect and the photoelectric effect. Below the critical energy no new shower particles are produced. Electromagnetic cascades can be characterized by the radiation length, X_0 , after which electrons/positrons reduced their energy to $1/e$ of their initial energy. For photons, it's equivalent to $7/9$ of the mean free path of pair production. The critical energy for ice is $E_c \approx 78$ MeV, with a radiation length of $X_0 \approx 39.3$ cm [30].

The radiation length governs the longitudinal shower profile and using $t = x/X_0$, the shower intensity can be described by

$$\frac{dE}{dt} = E_0 b \frac{(bt)^{a-1} e^{-bt}}{\Gamma(a)}, \quad (3.6)$$

where a and b are parameters that have to be estimated from experiment. Based on the work from [49], performed with Geant4 [50], the parameters for electromagnetic showers in ice are

$$e^- : a \approx 2.01 + 1.45 \log_{10}(E_0/\text{GeV}), b \approx 0.63 , \quad (3.7a)$$

$$e^+ : a \approx 2.00 + 1.46 \log_{10}(E_0/\text{GeV}), b \approx 0.63 , \quad (3.7b)$$

$$\gamma : a \approx 2.84 + 1.34 \log_{10}(E_0/\text{GeV}), b \approx 0.65 . \quad (3.7c)$$

The maximum of the shower is at $t_{max} = (a - 1)/b$ and the Cherenkov emission of the charged particles produced in the shower is peaked around the Cherenkov angle, since they are produced in the forward direction.

Hadronic Showers

In DIS interactions, a cascade is always produced by the hadrons coming from the breaking target nucleus. The cascade is a result of secondary particles produced in strong interactions between the hadrons and the traversed matter. The charged particles produced in the shower will emit Cherenkov radiation, while neutral particles will be invisible to the detector. There is also an electromagnetic component of the shower, due to for example the decay of neutral pions into photons. Hadronic showers of the same energy as electromagnetic showers have larger fluctuations in energy deposition and shape, since they depend on the produced particle types. Hadrons also have a higher energy threshold for Cherenkov light production, because of their higher mass. Based on [49, 51], the visible electromagnetic fraction of hadronic showers can be parameterized as

$$F(E_0) = \frac{T_{\text{hadron}}}{T_{\text{EM}}} = 1 - (1 - f_0) \left(\frac{E_0}{E_s} \right)^{-m} , \quad (3.8)$$

where $T_{\text{hadron/EM}}$ is the total track length of a hadronic/electromagnetic shower with the same energy, f_0 is the ratio of hadronic and electromagnetic light yield, E_0 is the initial energy, and E_s is an energy scale. The parameter m is a free model parameter. The ratio $F(E_0)$ increases with energy, but is

always smaller than 1. The variance of this distribution is given by

$$\sigma_F(E_0) = \sigma_0 \log(E_0)^{-\gamma} . \quad (3.9)$$

The parameters m , E_s , and f_0 were estimated by fitting the model to the results of Geant4 simulations. Cherenkov light from hadronic showers also peaks around the Cherenkov angle, but the angular distribution is more smeared out, due to the variations in particle type and their energy depositions.

3.3 Event Morphologies

The event morphologies produced by particles detected in IceCube are combinations of the three energy loss types described in Section 3.2.2, e.g. *cascades* from electromagnetic and hadronic showers and elongated *tracks* from muons traveling through the detector. Table 3.1 gives an overview of the possible event signatures.

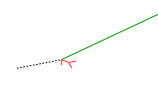
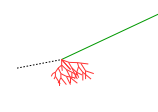
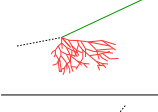
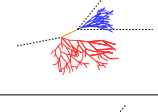
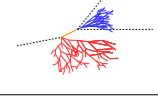
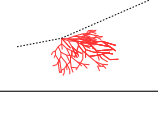
| Interaction | Secondary particles | Signature |
|---------------------|---|-----------------|
| CC $\nu_\mu^{(-)}$ |  μ^\pm track | Track-only |
| |  μ^\pm track and hadrons | Cascade + track |
| CC $\nu_\tau^{(-)}$ |  τ^\pm decaying into μ^\pm (~17% BR), hadrons | |
| |  τ^\pm decaying into e^\pm or hadrons (~83% BR) | |
| CC $\nu_e^{(-)}$ |  e^\pm , hadrons | Cascade-only |
| NC $\nu_\ell^{(-)}$ |  hadrons | |

Table 3.1: IceCube low energy event signatures, their underlying interaction type, and the particles that produce them. Also shown are the secondary particles produced in the interactions. Black dashed lines represent neutrinos, green lines muons, orange line leptons, and blue and red lines are particles in electromagnetic and hadronic cascades, respectively. Adapted from [19].

Neutrino interactions are observed as cascades, tracks, or a combination of both, depending on the initial flavor and the interaction type for the specific event.

In ν_μ - CC interactions, a muon is produced in addition to a hadronic shower from the breaking nucleus. If the interaction happens outside the detector, but the muon passes through the detector, this will create a track-like signature. The same happens if the interaction happens inside, but the

energy transfer to the nucleus is small ($y \approx 0$). At energies relevant for this work, tracks have length at the same order of the distance between DOMs, so they can be observed as such.

If the interaction happens inside the detector and the energy transfer to the hadronic part of the shower is larger, it will create a cascade with a track leaving it. A similar signature is observed after a ν_τ - CC interaction, in which a tau is produced that later decays into a muon, with a branching ratio of 17 %. In those cases the muon usually has a lower energy and the track will be fainter and harder to observe.

The other 83 % of ν_τ - CC interactions produce a tau that decays into an electron or hadrons, leaving a cascade-only signature through the electromagnetic or hadronic shower. All ν_e - CC interactions also produce pure cascades, since the electron quickly loses its energy in an electromagnetic shower. In all ν - NC interactions, the produced neutrino escapes and only the hadronic shower is observable. Since the size of the cascades at the energy range of interest is smaller than the spacing of the DOMs, they are approximately observed as point-like, spherical light sources. Even though the light is almost isotropically emitted, some asymmetry remains in the light profile, which can be used to reconstruct the direction of the incoming neutrino.

Atmospheric muons also produce pure track like signatures, similar to ν_μ - CC interactions happening outside the detector. They are one of the main backgrounds for analyses using atmospheric neutrinos and are therefore the target of many filter steps described in Section 5.3.1.

Heavy Neutral Lepton Signal Simulation

4

The central part of this thesis is the HNL signal simulation itself. Since this is the first search for HNLs with IceCube DeepCore, there was no prior knowledge of the number of events expected per year nor of the expected performance in terms of reconstruction and classification accuracy which governs the 90 % confidence level on estimating the $|U_{\tau 4}|^2$ mixing matrix element. This is the first HNL simulation developed for IceCube DeepCore. Two avenues of simulation generation were pursued in parallel. The physically accurate, model dependent simulation is described in Section 4.2 and a collection of model independent simulation samples was realized and is explained in Section 4.1. The latter is used for performance benchmarking and as a cross-check for the model dependent simulation. The SM simulation generation and the default low energy event selection and processing chain are introduced in Chapter 5 and everything but the generation is applied identically to both neutrinos and HNLs.

| | |
|--|----|
| 4.1 Model Independent Simulation | 27 |
| 4.2 Model Dependent Simulation | 30 |

JVS: I would describe simulation sets you produced in past rather than present tense (ORANGE)

4.1 Model Independent Simulation

To investigate the potential of IceCube to detect HNLs by identifying the unique double cascade morphology explained in Section ??, it is very valuable to have a simulation chain where the double cascade kinematics can be controlled directly. In a realistic model the decay kinematics and the absolute event expectation all depend on the specific model parameters chosen (see Section ??). To decouple the simulation from a specific parameter choice, a model independent double cascade generator was developed. Using this generator several simulation samples were produced to investigate the performance of IceCube DeepCore to detect low energetic double cascades, dependent on their properties. All samples are produced using a collection of custom generator functions [52] that place two EM cascade vertices with variable energy and direction at choosable locations in the detector. The results of this study will be discussed in Chapter 6.

4.1.1 Simplistic Samples

To investigate some idealistic double cascade event scenarios, two samples are produced for straight up-going events that are centered on a string and horizontal events located inside DeepCore.

Make my own DC string positions/distances plot version, viable for the margin? (YELLOW)

The first sample is used to investigate one of the most promising scenarios to detect a double cascade, where both cascade centers are located on a DeepCore string (namely string 81) and the directions are directly up-going. The horizontal positions and distances of all DeepCore fiducial volume strings are shown in Figure 4.1 and string 81 is at a medium distance of ~ 70 m to its neighboring strings. As already mentioned in Section 3.1.3, DeepCore strings have higher quantum efficiency DOMs and a denser vertical spacing, making them better to detect low energetic events that produce little light. To produce the events, the x, y position of the cascades is fixed to the

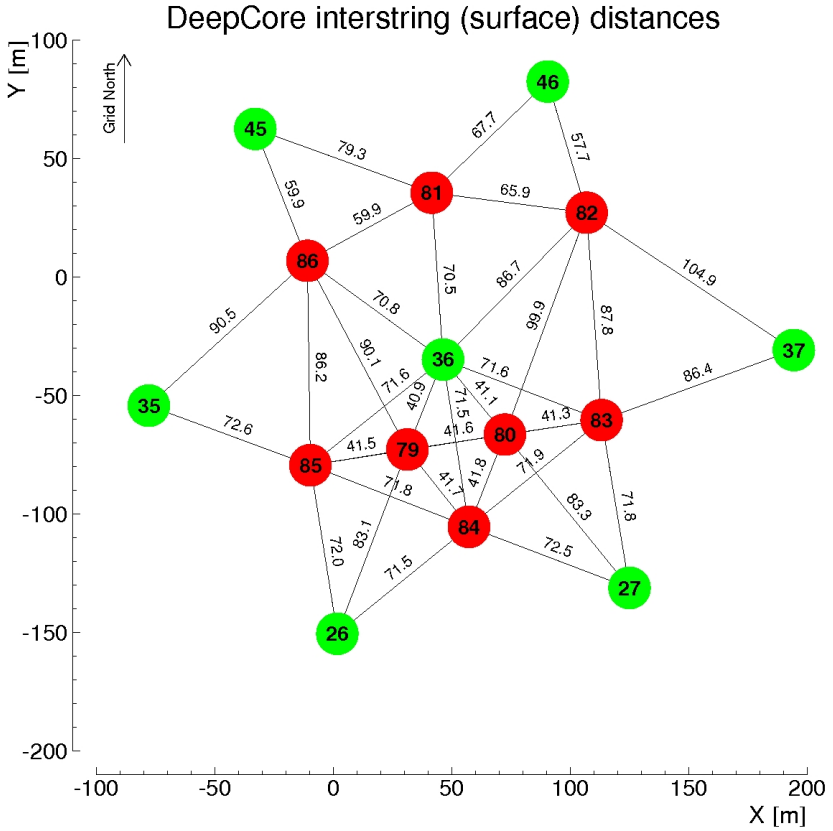


Figure 4.1: Horizontal positions and distances between DeepCore strings. Red strings are instrumented more densely (vertically) and partially have higher quantum efficiency (HQE) DOMs.

center of string 81 while the z positions are each sampled uniformly along the axis of the string. Note here that this will therefore not produce a uniform length distribution between the cascades. The positions are defined in the IceCube coordinate system that was already introduced in Section 3.1.2. The energies are sampled uniformly between 0.0 GeV and 60.0 GeV. The specific sampling distributions/values for the cascades are listed in Table 4.1. The order of the cascades is chosen such that the lower one is first ($t_0 = 0.0$ ns) and the upper one is second ($t_1 = L/c$), assuming the speed of light c as speed of the heavy mass state, traveling between the two cascades.

The second sample is used to investigate the reconstruction performance for horizontal events, where the spacing between DOMs is much larger. The cascades are placed uniformly on a circle centered in DeepCore. The direction is always horizontal and azimuth is defined by the connecting vector of both cascade positions. The energies are again sampled uniformly between 0.0 GeV and 60.0 GeV and the detailed sampling distributions/values are also listed in Table 4.1. Some examples of the generation level distributions of the simplified samples are shown in Figure 4.2, while further distributions can be found in Figure A.1.

4.1.2 Realistic Sample

To thoroughly investigate the potential of IceCube DeepCore to detect double cascade events, a more realistic simulation sample is produced that aims to be as close as possible to the expected signal simulation explained in Section 4.2, while still allowing additional freedom to control the double cascade kinematics. For this purpose the total energy is sampled from an E^{-2} power

Re-make plot with all energies (cascades and total, both samples (they are the same)) (RED)

Re-make plot with all decay lengths (both samples) (RED)

describe why these are shown to highlight some key aspect (uniformity in both energies to sample the whole space, decay length as a result of the z sampling etc..), also add this shortly to the caption (RED)

| Sample | Variable | Distribution | Range/Value |
|-------------------|---------------|------------------|--------------------------------|
| Up-going | | | |
| | energy | uniform | 0.0 GeV to 60.0 GeV |
| | zenith | fixed | 180.0° |
| | azimuth | fixed | 0.0° |
| | x, y position | fixed | (41.6, 35.49) m |
| | z position | uniform | -480.0 m to -180.0 m |
| Horizontal | | | |
| | energy | uniform | 0.0 GeV to 60.0 GeV |
| | zenith | fixed | 90.0° |
| | azimuth | uniform | 0.0° to 360.0° |
| | x, y position | uniform (circle) | c=(46.29, -34.88) m, r=150.0 m |
| | z position | fixed | -330.0 m |

Table 4.1: Generation level sampling distributions and ranges/values of up-going and horizontal model independent simulation.

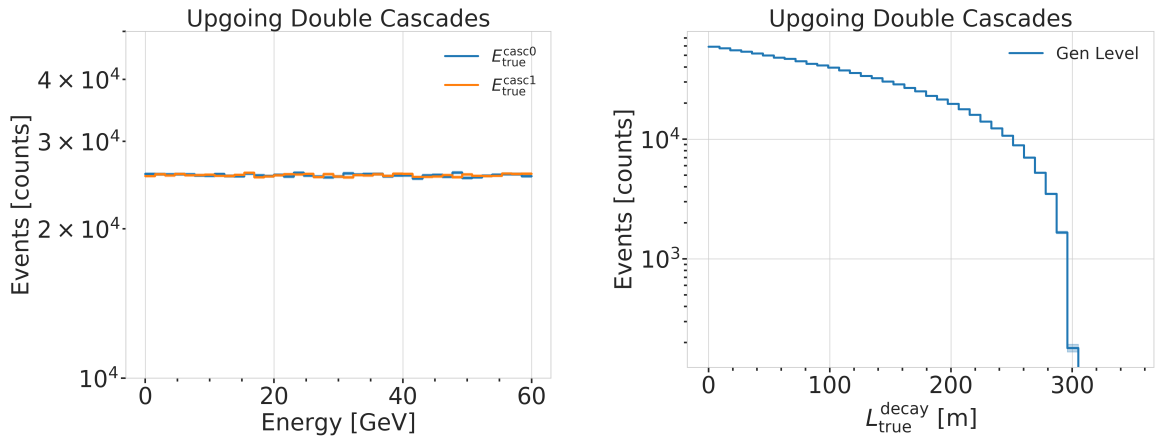


Figure 4.2: Generation level distributions of the simplistic simulation samples. Cascade and total energies (left) and decay lengths (right) of both samples are shown.

law, mimicking the energy spectrum of the primary neutrinos as stated in Section 5.1.1. The total energy is divided into two parts, by assigning a fraction between 0 % and 100 % to one cascade and the remaining part to the other cascade. This is a generic approximation of the realistic process described in Section 4.2, and chosen such that the whole sample covers various cases of energy distributions between the two cascades. To efficiently generate events in a way that produces distributions similar to what would be observed with DeepCore, one of the cascade positions is sampled inside the DeepCore volume by choosing its coordinates uniformly on a cylinder that is centered in DeepCore. This is similar to a trigger condition of one cascade always being inside the DeepCore fiducial volume. By choosing the direction of the event by sampling zenith and azimuth uniformly between 70° and 180° and 0° and 360°, respectively, the position of the other cascade can be inferred for a given decay length, assuming a travel speed of c , and choosing whether the cascade position that was sampled is the first cascade or the second with a 50 % chance. The decay length is sampled from an exponential distribution, as expected for a decaying heavy mass state. The sampling distributions/values are listed in Table 4.4. Example distributions of the generation level variables are shown in Figure 4.3, while further distributions can be found in Figure A.2.

again, describe what is shown and why this is interesting (e.g. energy distribution between the cascades, realistic exponential decay length distribution..) also add this to the captions shortly (RED)

Table 4.2: Generation level sampling distributions and ranges/values of the realistic model independent simulation.

| Variable | Distribution | Range/Value |
|----------------------|--------------------------|----------------------------------|
| energy (total) | power law E^{-2} | 1 GeV to 1000 GeV |
| decay length | exponential $e^{-0.01L}$ | 0 m to 1000 m |
| zenith | uniform | 70° to 180° |
| azimuth | uniform | 0° to 360° |
| x, y (one cascade) | uniform (circle) | $c=(46.29, -34.88)$ m, $r=150$ m |
| z (one cascade) | uniform | -480.0 m to -180.0 m |

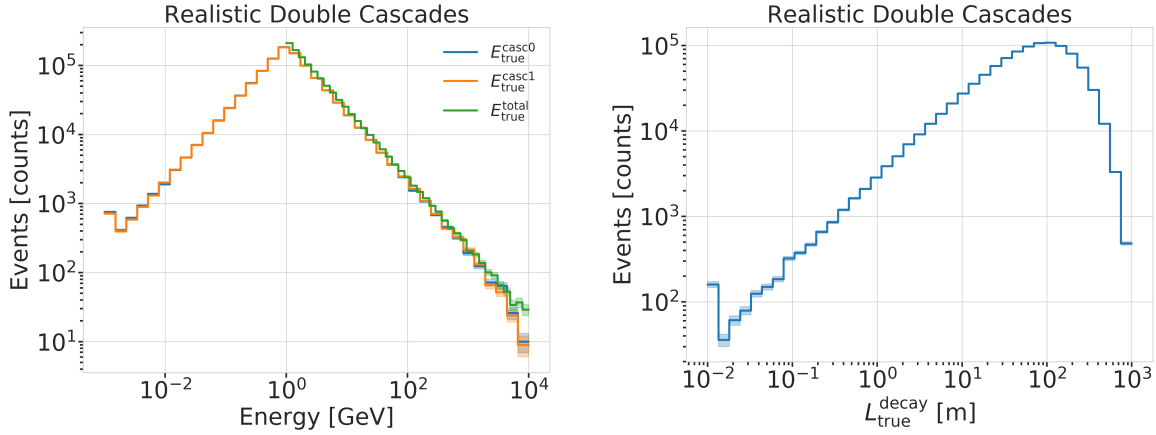


Figure 4.3: Generation level distributions of the simplistic realistic sample. Shown are the cascade and total energies (left) and decay lengths (right).

4.2 Model Dependent Simulation

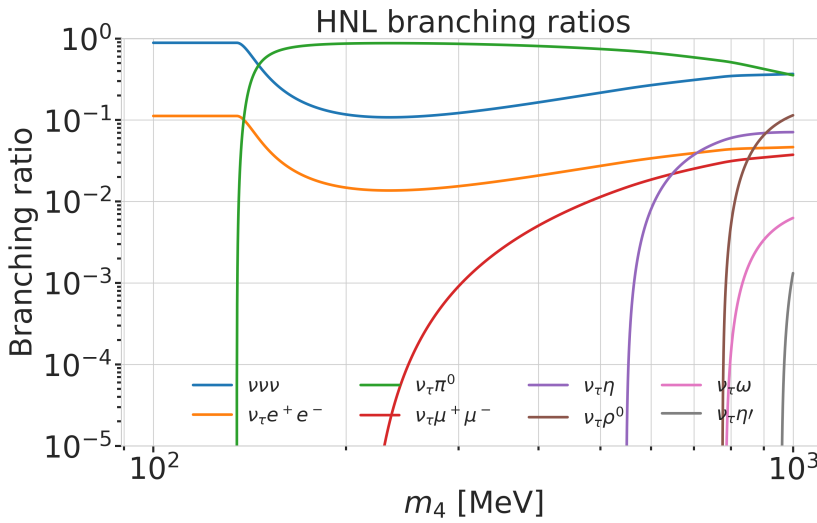
To estimate the HNL event expectation in IceCube DeepCore, depending on the specific model parameters, a generator was developed that is based on the HNL theory introduced in Section ???. For this work, only the interaction with the τ -sector was taken into account ($|U_{\alpha 4}^2| = 0$, $\alpha = e, \mu$), which reduces the physics parameters of interest and relevant for the simulation to the fourth heavy lepton mass, m_4 , and the mixing, $|U_{\tau 4}^2|$. The generator uses a customized *LeptonInjector* (LI) version to create the events and *LeptonWeighter* (LW) to weight them [53]. The modified LI and the essential components needed for the HNL simulation are described in the next sections, followed by the description of the weighting scheme and the sampling distributions chosen for the simulation generation.

[53]: Abbasi et al. (2021), “LeptonInjector and LeptonWeighter: A neutrino event generator and weighter for neutrino observatories”

4.2.1 Custom LeptonInjector

In its standard version, the LI generator produces neutrino interactions by injecting a lepton and a hadronic cascade at the interaction vertex of the neutrino, where the lepton is the charged (neutral) particle produced in a CC (NC) interaction and the cascade is the hadronic cascade from the breaking nucleus. The hadronic cascade is stored as a specific object of type *Hadrons*, which triggers the correct simulation of the shower development in the following simulation steps, identical to what will be described for SM neutrino simulation on Section 5.1.1. The main differences to an EM cascade is that part of the energy will not be observed, because it goes into neutral particles, and that the spatial development of the shower is different. Both objects are injected with the same (x, y, z, t) coordinates and the kinematics

are sampled from the differential and total cross-sections that are one of the inputs to LI.



JVS: consider remaking figures at the native size so type size is consistent. Also, consider making the legend box semi-transparent so the lines do not obscure the text and markers. (ORANGE)

Figure 4.4: Branching ratios of the HNL within the mass range considered in this work, only considering $|U_{\tau 4}^2| \neq 0$, calculated based on the results from [36].

In the modified version, the SM lepton at the interaction vertex is replaced by the new HNL particle, where the interaction cross-sections are replaced by custom, mass dependent HNL cross-sections. The HNL is forced to decay after a chosen distance¹ to produce secondary SM particles, where the decay mode is chosen with a probability given by the mass dependent branching ratios from the kinematically accessible decay modes shown in Figure 4.4. The cross-section and decay width calculations were implemented for this purpose and will be explained in more detail in the following. Another needed addition to LI is that the decay products of the HNL are also added to the list of MC particles in each event. They are injected with the correctly displaced position and delayed time from the interaction vertex, given the HNL decay length. These HNL daughter particles form the second cascade, not as a single hadronic cascade object, but as the explicit particles forming the shower. The kinematics of the two-body decays are computed analytically, while the three-body decay kinematics are calculated with MADGRAPH [54], which will also be explained further below. Independent of the number of particles in the final state of the HNL decay, the kinematics are calculated/simulated at rest and then boosted along the HNL momentum.

The injection is done using the LI *volume mode*, for the injection of the primary particle on a cylindrical volume, adding 50 % of the events with ν_τ and the other half with $\bar{\nu}_\tau$ as primary particle types. The generator takes the custom double-differential/total cross-section splines described below and the parameters defining the sampling distributions as inputs.

Cross-Sections

The cross-sections are calculated using the NuXSSPLMCR [55] software, which is a tool to calculate neutrino cross-sections from *parton distribution functions (PDFs)* and then fit to an N-dimensional tensor-product B-spline surface [56] to produce the splines that can be read and used with LI/LW. The tool was modified to produce the custom HNL cross-sections, where the main modification to calculate the cross-sections for the ν_τ -NC interaction into the new heavy mass state, is the addition of a kinematic condition to

1: The explicit sampling distributions and ranges can be found in Section 4.2.2.

[54]: Alwall et al. (2014), “The automated computation of tree-level and next-to-leading order differential cross sections, and their matching to parton shower simulations”

Maybe decide if I want to handle git repo urls/references in a different way.. currently (without date+title) they look ugly in the margin, so I just state them as regular cites, but Cris gave me some other ideas on how to handle them.. (YELLOW)

[56]: Whitehorn et al. (2013), “Penalized splines for smooth representation of high-dimensional Monte Carlo datasets”

[57]: Levy (2009), “Cross-section and polarization of neutrino-produced tau’s made simple”

ensure that there is sufficient energy to produce the heavy mass state. It is the same condition fulfilled for the CC case, where the outgoing charged lepton mass is non-zero. Following [57] (equation 7), the condition

$$(1 + x\delta_N)h^2 - (x + \delta_4)h + x\delta_4 \leq 0 \quad (4.1)$$

is implemented for the NC case in the NuXSSplMkr code. Here

$$\delta_4 = \frac{m_4^2}{s - M^2}, \quad (4.2)$$

$$\delta_N = \frac{M^2}{s - M^2}, \text{ and} \quad (4.3)$$

$$h \stackrel{\text{def}}{=} xy + \delta_4, \quad (4.4)$$

with x and y being the Bjorken variables, m_4 and M the mass of the heavy state and the target nucleon, respectively, and s the center of mass energy squared. The custom version was made part of the open source NuXSSplMkr software and can thus be found in [55]. The result of this kinematic condition is that events cannot be produced for energy, x , y combinations that don’t have sufficient energy going into the outgoing, massive lepton. This results in a reduction of the cross-section towards lower energies, which scales with the assumed mass of the HNL. This effect can clearly be seen in Figure 4.5.

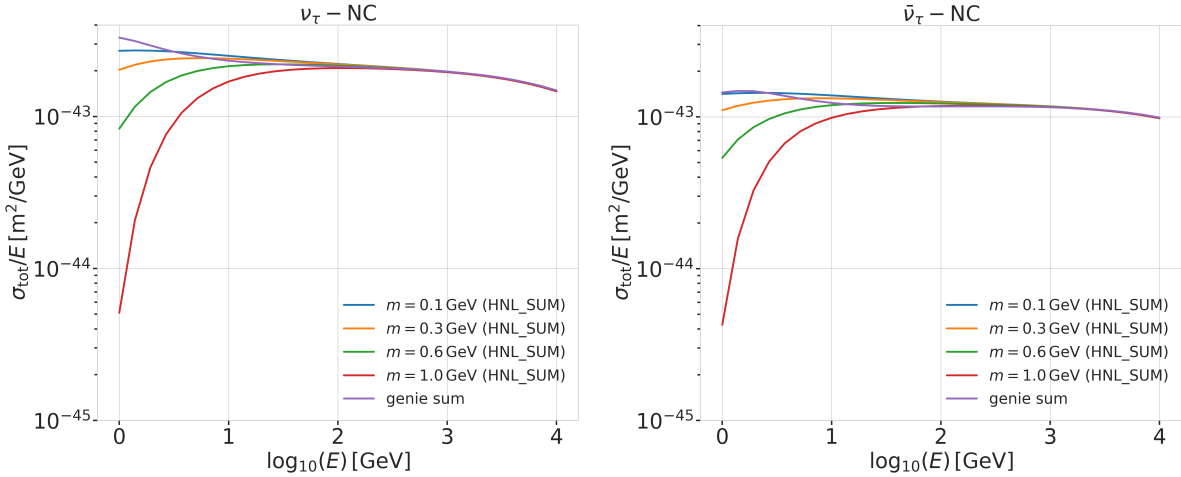


Figure 4.5: Custom HNL total cross-sections for the four target masses compared to the total ($\nu_\tau/\bar{\nu}_\tau$ NC) cross-section used for SM neutrino simulation production with GENIE.

Re-make plot with 3 star
get masses and better
labels/legends etc. (RED)

The GRV98LO PDFs were added to the cross-section spline maker and used to create the HNL cross-sections for consistency with the SM neutrino simulation that will be explained in Section 5.1.1. The double-differential ($d\sigma/dxdy$) and total (σ) cross-sections were produced for the chosen target HNL masses and then splined in energy, x , and y and just in the energy, respectively. The produced cross-section are added to the custom LI version and used for the simulation generation and weighting. Figure 4.5 shows the total cross-sections that were produced compared to the cross-section used for the production of the SM $\nu_\tau/\bar{\nu}_\tau$ NC background simulation. They agree above a certain energy (~ 200 GeV), where the modification should not have any effect on the cross-sections, which is the desired result of using the identical input PDFs and confirms that the unmodified cross-sections produced with NuXSSplMkr agree with the GENIE cross-sections, which

were used to generate the SM background MC.

Decay Channels

The accessible decay channels are dependent on the mass of the HNL and the allowed mixing. For this analysis, where only $|U_{\tau 4}|^2 \neq 0$, the decay channels considered are listed in Table 4.3 and the corresponding branching ratios are shown in Figure 4.4. The individual branching ratio for a specific mass is calculated as $\text{BR}_i(m_4) = \Gamma_i(m_4)/\Gamma_{\text{total}}(m_4)$, where $\Gamma_{\text{total}}(m_4) = \sum \Gamma_i(m_4)$. The individual decay widths Γ_i are computed using the state-of-the-art calculations from [36], which are described in the following.

2-Body Decay Widths The decay to a neutral pseudoscalar meson is

$$\Gamma_{\nu_4 \rightarrow \nu_\tau P} = |U_{\tau 4}|^2 \frac{G_F^2 m_4^3}{32\pi} f_P^2 (1 - x_p^2)^2, \quad (4.5)$$

with $x_P = m_P/m_4$ and the *effective decay constants* f_P given by

$$f_{\pi^0} = +0.1300 \text{ GeV}, \quad (4.6)$$

$$f_\eta = +0.0816 \text{ GeV}, \text{ and} \quad (4.7)$$

$$f_{\eta'} = -0.0946 \text{ GeV}, \quad (4.8)$$

while the decay to a neutral vector meson is given by

$$\Gamma_{\nu_4 \rightarrow \nu_\tau V} = |U_{\tau 4}|^2 \frac{G_F^2 m_4^3}{32\pi} \left(\frac{f_V}{m_V} \right)^2 g_V^2 (1 + 2x_V^2)(1 - x_V^2)^2, \quad (4.9)$$

with $x_V = m_V/m_4$,

$$f_{\rho^0} = 0.171 \text{ GeV}^2, \quad (4.10)$$

$$f_\omega = 0.155 \text{ GeV}^2, \quad (4.11)$$

and

$$g_{\rho^0} = 1 - 2 \sin^2 \theta_w, \quad (4.12)$$

$$g_\omega = \frac{-2 \sin^2 \theta_w}{3}, \quad (4.13)$$

and $\sin^2 \theta_w = 0.2229$ [58], where θ_w is the Weinberg angle.

SB: emphasize the cut-off/suppression (ORANGE)

Add comparisons of SM cross-sections between NuXSSplMkr and genie? (YELLOW)

[36]: Coloma et al. (2021), “GeV-scale neutrinos: interactions with mesons and DUNE sensitivity”

| Channel | Opens | $\hat{\text{BR}}$ |
|--|---------|-------------------|
| $\nu_4 \rightarrow \nu_\tau \nu_\alpha \bar{\nu}_\alpha$ | 0 MeV | 1.0 |
| $\nu_4 \rightarrow \nu_\tau e^+ e^-$ | 1 MeV | ? |
| $\nu_4 \rightarrow \nu_\tau \pi^0$ | 135 MeV | ? |
| $\nu_4 \rightarrow \nu_\tau \mu^+ \mu^-$ | 211 MeV | ? |
| $\nu_4 \rightarrow \nu_\tau \eta$ | 548 MeV | ? |
| $\nu_4 \rightarrow \nu_\tau \rho^0$ | 770 MeV | ? |
| $\nu_4 \rightarrow \nu_\tau \omega$ | 783 MeV | ? |
| $\nu_4 \rightarrow \nu_\tau \eta'$ | 958 MeV | ? |

Table 4.3: Possible decay channels of the HNL, considering only $|U_{\tau 4}|^2 \neq 0$. Listed is the mass at which each channel opens and the maximum branching ratio.

Calculate max BRs or remove.. (RED)

[58]: Tiesinga et al. (2021), “CODATA recommended values of the fundamental physical constants: 2018”

3-Body Decay Widths The (invisible) decay to three neutrinos, one of flavor τ and two of any flavor α , is

$$\Gamma_{\nu_4 \rightarrow \nu_\tau \nu_\alpha \bar{\nu}_\alpha} = |U_{\tau 4}|^2 \frac{G_F^2 m_4^5}{192\pi^3}, \quad (4.14)$$

while the decay to two charged leptons (using $x_\alpha = (m_\alpha/m_4)^2$) of the same flavor reads

$$\Gamma_{\nu_4 \rightarrow \nu_\tau l_\alpha^+ l_\alpha^-} = |U_{\tau 4}|^2 \frac{G_F^2 m_4^5}{192\pi^3} [C_1 f_1(x_\alpha) + C_2 f_2(x_\alpha)], \quad (4.15)$$

with the constants defined as

$$C_1 = \frac{1}{4}(1 - 4 \sin^2 \theta_w + 8 \sin^4 \theta_w), \quad (4.16)$$

$$C_2 = \frac{1}{2}(-\sin^2 \theta_w + 2 \sin^4 \theta_w), \quad (4.17)$$

the functions as

$$f_1(x_\alpha) = (1 - 14x_\alpha - 2x_\alpha^2 - 12x_\alpha^3)\sqrt{1 - 4x_\alpha} + 12x_\alpha^2(x_\alpha^2 - 1)L(x_\alpha), \quad (4.18)$$

$$f_2(x_\alpha) = 4[x_\alpha(2 + 10x_\alpha - 12x_\alpha^2)\sqrt{1 - 4x_\alpha} + 6x_\alpha^2(1 - 2x_\alpha + 2x_\alpha^2)L(x_\alpha)], \quad (4.19)$$

and

$$L(x) = \ln\left(\frac{1 - 3x_\alpha - (1 - x_\alpha)\sqrt{1 - 4x_\alpha}}{x_\alpha(1 + \sqrt{1 - 4x_\alpha})}\right). \quad (4.20)$$

3-Body Decay Kinematics with MadGraph

The specific MadGraph version used to produce the 3-body decay kinematics is `MADGRAPH4 v3.4.0` [59], which uses the decay diagrams calculated with `FEYNRULES 2.0` [60] and the Lagrangians derived in [36] as input. The *Universal FeynRules Output (UFO)* from `EFFECTIVE_HEAVYN_MAJORANA_v103` were used for our calculation. For each mass and corresponding decay channels, we produce 1×10^6 decay kinematic variations in the rest frame and store those in a text file. During event generation, we uniformly select an event from that list, to simulate the decay kinematics of a 3-body decay.

4.2.2 Sampling Distributions

In principle, the generation level sampling distributions should be chosen such that at final level of the selection chain the phase space relevant for the analysis is covered with sufficient statistics to make a reasonable estimate of the event expectation. Initial distributions insufficiently covering the phase space leads to an underestimate of the expected rates, because part of the events that would pass the selection are not produced. This limits the expected analysis potential. Three discrete simulation samples were produced with HNL masses of 0.3 GeV, 0.6 GeV, and 1.0 GeV. Because during development it became clear that the low lengths component is crucial to get a reasonable event estimate, each sample consists of a part that is generated for very short decay lengths and one for long decay lengths. The remaining sampling distributions are identical for all samples and are listed in Table 4.4. The target number of events for each sample was 2.5×10^9 .

Table 4.4: Generation level sampling distributions and ranges/values of the model dependent simulation samples.

| Variable | Distribution | Range/Value |
|--------------------|------------------------------|------------------------------|
| energy | E^{-2} | [2 GeV, 1×10^4 GeV] |
| zenith | uniform (in $\cos(\theta)$) | [80°, 180°] |
| azimuth | uniform | [0°, 360°] |
| vertex x, y | uniform | $r=600$ m |
| vertex z | uniform | -600 m to 0 m |
| m_4 | fixed | [0.3, 0.6, 1.0] GeV |
| L_{decay} | L^{-1} | [0.0004, 1000] m |

4.2.3 Weighting Scheme

To produce physically correct event distributions based on the simplified generation sampling distributions for the HNL simulation, the forward folding method that was already introduced for the SM simulation in Section 5.1 is also used. The only required input is the mixing strength $|U_{\tau 4}|^2$, which is the variable physics parameter in this analysis. For each event the gamma factor

$$\gamma = \frac{\sqrt{E_{\text{kin}}^2 + m_4^2}}{m_4}, \quad (4.21)$$

is calculated, with the HNL mass m_4 , and its kinetic energy E_{kin} . The speed of the HNL is calculated as

$$v = c \cdot \sqrt{1 - \frac{1}{\gamma^2}}, \quad (4.22)$$

where c is the speed of light. With these, the lab frame decay length range $[s_{\min}, s_{\max}]$ can be converted into the rest frame lifetime range $[\tau_{\min}, \tau_{\max}]$ for each event

$$\tau_{\min/\max} = \frac{s_{\min/\max}}{v \cdot \gamma}. \quad (4.23)$$

The proper lifetime of each HNL event can be calculated using the total decay width Γ_{total} from Section 1 and the chosen mixing strength $|U_{\tau 4}|^2$ as

$$\tau_{\text{proper}} = \frac{\hbar}{\Gamma_{\text{total}}(m_4) \cdot |U_{\tau 4}|^2}, \quad (4.24)$$

where \hbar is the reduced Planck constant. Since the decay lengths or lifetimes of the events are sampled from an inverse distribution instead of an exponential, as it would be expected from a particle decay, we have to re-weight accordingly to achieve the correct decay lengths or lifetimes distribution. This is done by using the wanted exponential distribution

$$\text{PDF}_{\text{exp}} = \frac{1}{\tau_{\text{proper}}} \cdot e^{\frac{-\tau}{\tau_{\text{proper}}}}, \quad (4.25)$$

and the inverse distribution that was sampled from

$$\text{PDF}_{\text{inv}} = \frac{1}{\tau \cdot (\ln(\tau_{\max}) - \ln(\tau_{\min}))}. \quad (4.26)$$

This re-weighting factor is then calculated as

$$w_{\text{lifetime}} = \frac{\text{PDF}_{\text{exp}}}{\text{PDF}_{\text{inv}}} = \frac{\Gamma_{\text{total}}(m_4) \cdot |U_{\tau 4}|^2}{\hbar} \cdot \tau \cdot (\ln(\tau_{\max}) - \ln(\tau_{\min})) \cdot e^{\frac{-\tau}{\tau_{\text{proper}}}}. \quad (4.27)$$

Adding another factor of $|U_{\tau 4}|^2$ to account for the mixing at the interaction vertex the total re-weighting factor becomes

$$w_{\text{total}} = |U_{\tau 4}|^2 \cdot w_{\text{lifetime}}. \quad (4.28)$$

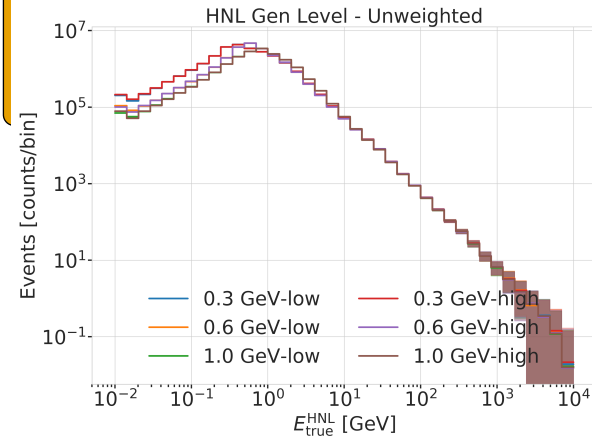
If this additional weighting factor is multiplied to a generation weight with units m^2 (like in Equation 5.1), the livetime in s , and the oscillated primary neutrino flux in $\text{m}^{-2}\text{s}^{-1}$, it results in the number of expected events in the detector for this particular MC event for a chosen mixing (and mass).

JVS: The build-up of the weight expression is hard to follow without knowing where it's going. It may be better to start with the fact that the importance sampling weight is the ratio of PDFs, then write down each pdf, then drill down into each of the terms (basically, the standard "tell me what you're going to tell me, then tell me, then tell me what you told me" scheme). (RED)

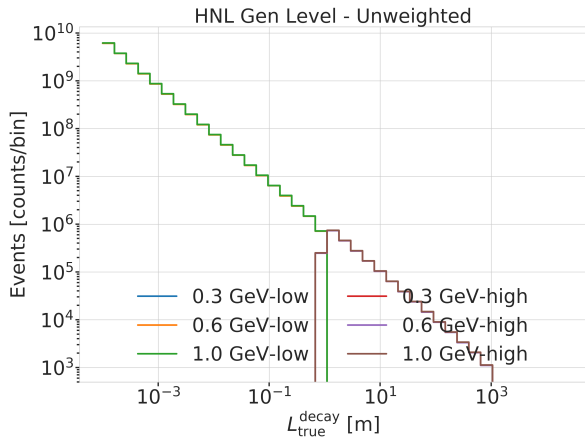
4.2.4 Generation Level Distributions

Figure 4.6 shows some selected generation level distributions. Additional distributions can be found in Figure A.3.

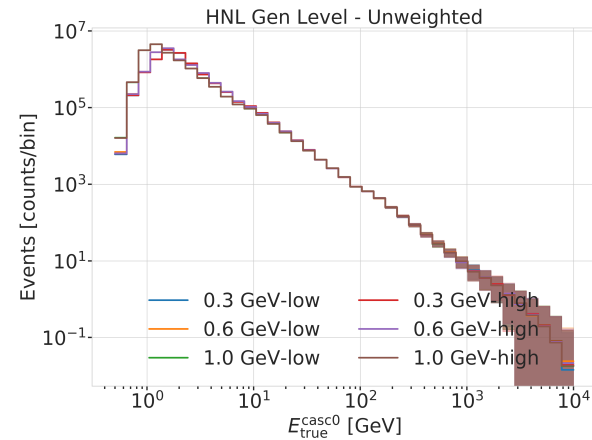
Combine low/high plots
and remove all traces



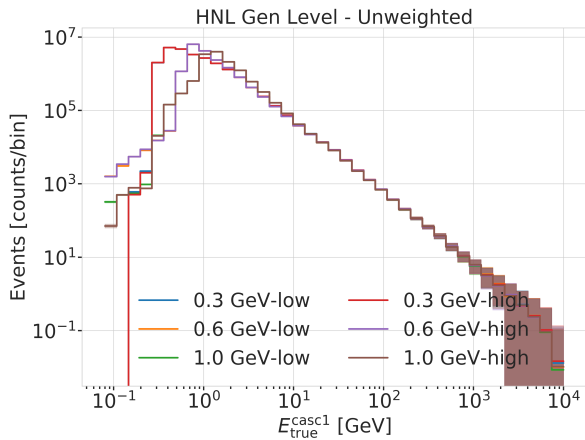
(a) HNL energy



(b) Decay length



(c) First cascade energy



(d) Second cascade energy

Figure 4.6: Generation level distributions of the model dependent simulation.

What is the message of these plots? Make it clear in the text and also in the captions. Potentially cut down to one or two and leave the rest or move them to the appendix. (RED)

Standard Model Background Simulation and Data Processing

5

The analysis presented in this thesis is highly dependent on an efficient event selection to reduce the raw IceCube trigger data to a usable atmospheric neutrino sample. Based on this selection, a precise estimation of both expected SM background and expected BSM signal events can be made using MC simulations. This chapter describes the current simulation and event selection chain used for state-of-the-art IceCube neutrino oscillation measurements like [61]. The whole chain can be broadly split into 4 steps:

Step 1 Event Generation: The initial step for all particle (non-noise) simulation is the generation of events from selected initial distributions and fluxes. Events are the primary particle and the particles produced in the interaction with the ice.

Step 2 Detector Simulation: The particles from the first step are propagated through the ice, producing Cherenkov photons, which are then propagated further until they reach a DOM or are absorbed. If they hit a DOM the detector response (acceptance and PMT) is simulated.

Step 3 Processing: Starting from the PMT output, both real data and simulation are processed through the in-ice trigger, the online filter and processing, and the low energy event selection to produce a neutrino dominated sample.

Step 4 Reconstruction: Once the sample is small enough for more sophisticated reconstruction techniques to be feasible to run, the events are reconstructed using a CNN and some high level variables are computed. Based on these variables the final event selection is applied.

This chapter only describes the event generation for the SM background simulation (neutrinos and muons), while the signal simulation is described in Chapter 4. The detector simulation is identical for both signal and background events while processing and reconstruction are applied to all simulation and data in the same way. Splitting the simulation steps has the advantage of reusing the outputs of for example the generation step to propagate the particles with different ice model, in order to estimate the systematic impacts of uncertainties of the ice properties. Similar approach can be taken for varying detector response and through this a more efficient (reduced) use of computing resources can be achieved. The following sections describe the different steps in more detail and the last section, Section 5.5, describes the related systematic uncertainties considered for this work.

5.1 Event Generation

The MC is used in the analysis by applying a method called *forward folding*, where a very large number of events (signal and background) is produced using sampling distribution that are tuned to have a large selection efficiency. Those distributions don't have to be physically correct distributions, but they need to cover the full parameter space of interest for the analysis. To produce a physical distribution, the events are weighted given a specific

Adapt chapter to reflect switched chapter order
5.1 Event Generation . . . 37
5.2 Detector Simulation . . 39

SSB: Processing considered instead to have a chapter on all Simulation (signal and background). and . . 47
then another chapter on [61] Abbasi et al. (2023), Measurement, Data processing and reconstruction? The “DeepCore calibration and data processing” description can either go into the simulation chapter OR it can go into the double cascade reconstruction chapter at an appropriate location/sub-section (ORANGE)

Table 5.1: Cylinder volumes used for GENIE neutrino simulation generation. Cylinder is always centered in DeepCore at $(x, y, z) = (46.29, -34.88, -330.00)$ m.

| Flavor | Energy [GeV] | Radius [m] | Length [m] | Events/File | Files |
|-----------------------------|--------------|------------|------------|-------------|-------|
| $\nu_e + \bar{\nu}_e$ | 1-4 | 250 | 500 | 450000 | |
| | 4-12 | | | | |
| | 12-100 | 350 | 600 | 100000 | 650 |
| | 100-10000 | 550 | 1000 | 57500 | |
| $\nu_\mu + \bar{\nu}_\mu$ | 1-5 | 250 | 500 | 408000 | |
| | 5-80 | 400 | 900 | 440000 | |
| | 80-1000 | 450 | | 57500 | 1550 |
| | 1000-10000 | 550 | 1500 | 6700 | |
| $\nu_\tau + \bar{\nu}_\tau$ | 1-4 | 250 | 500 | 1500000 | |
| | 4-10 | | | 300000 | |
| | 10-50 | 350 | 600 | 375000 | 350 |
| | 50-1000 | 450 | 800 | 200000 | |
| | 1000-10000 | 550 | 1500 | 26000 | |

choice of physics and nuisance parameters. The large number of raw MC events ensures a good estimation of the expected numbers and weighted distributions.

The analysis itself is then performed by comparing the weighted MC distributions to the observed data. This is done by binning them as described in Chapter 7 and calculating a loss function comparing the bin expectations to the data. The physics and nuisance parameters that best correspond to the observed data are estimated by minimizing this loss function. In order to achieve a reliable result with this method the MC needs to be precise and as close to the data as possible (at least at the final event selection).

5.1.1 Neutrinos

Due to the very low interaction rate of neutrinos, the event generation is performed in a way that forces every event to interact in a chosen sampling volume. The weight of each event is then calculated as the inverse of the simulated neutrino fluence

$$w_{\text{gen}} = \frac{1}{F_{\text{sim}}} \frac{1}{N_{\text{sim}}} , \quad (5.1)$$

where F_{sim} is the number of neutrino events per energy, time, area, and solid angle and N_{sim} is the number of simulated events. If this weight is multiplied by the livetime and the theoretically expected neutrino flux for a given physical model, it results in the number of expected events in the detector for this particular MC event. The baseline neutrino flux used in this thesis, computed for the South Pole, is taken from Honda *et al.* [31].

The simulation volume is a cylinder centered in DeepCore with radius and height chosen such that all events possibly producing a signal are contained. The different sizes, chosen depending on energy and neutrino flavor, are shown in Table 5.1. The directions of the neutrinos are sampled isotropically and the energies are sampled from an E^{-2} power law. The number of simulated events is chosen such that the livetime is more than 70 years for each flavor. Neutrinos and antineutrinos are simulated with ratios of 70% and 30%, respectively.

[31]: Honda *et al.* (2015), “Atmospheric neutrino flux calculation using the NRLMSISE-00 atmospheric model”

To simulate the neutrino interaction with the ice, the GENIE event generator [62] (version 2.12.8) is used, resulting in the secondary particles and the kinematic and cross-section parameters. As input, the outdated GRV98LO [63] *parton distribution functions (PDFs)* was used, because it was the only option that could incorporate extrapolations to lower Q^2 [64]. Muons produced in these interactions are propagated using PROPOSAL [65], also simulating their Cherenkov light output. The shower development of gamma rays, electrons, and positrons below 100 MeV and hadronic showers below 30 GeV is simulated using GEANT4 [50] while for higher energies an analytical approximation from [47] is used.

5.1.2 Muons

Atmospheric muons are generated on a cylinder surface enclosing the full IceCube detector array. The cylinder has a height of 1600 m and a radius of 800 m. The energy is sampled from an E^{-3} power law while the other sampling distributions (position, direction) are found from parameterizations based on [66]. This work uses full CORSIKA [67] simulations of muons to tailor the parameterizations, starting from *cosmic ray (CR)* interactions with atmospheric nuclei using the CR flux model from [68] and producing the muons applying the *hadronic interaction (HI)* model SIBYLL 2.1 [69]. After the generation, they are propagated through the ice with PROPOSAL producing photons, treating them exactly like the muons produced in neutrino interactions.

Since the offline processing and selection steps described in Section 5.3.2 and Section 5.4 reduce the muon contamination to an almost negligible level, the statistical uncertainty on the number of expected muon events at the final selection level is large and therefore two separate sets of muon simulation are produced. **A first set** including all events resulting from the above described generation to tune the lower level selection (up to L4) and **a second set** to estimate the muon contamination at higher levels (above L5), which only accepts muon events if they pass through a smaller cylinder centered in DeepCore (height of 400 m and radius of 180 m) and rejects events based on a KDE estimated muon density at L5 (in energy and zenith) increasing the simulation efficiency at L5 significantly .

[62]: Andreopoulos et al. (2015), “The GENIE Neutrino Monte Carlo Generator: Physics and User Manual”

[63]: Glück et al. (1998), “Dynamical parton distributions revisited”

[64]: Bodek et al. (2003), “Higher twist, xi(omega) scaling, and effective LO PDFs for lepton scattering in the few GeV region”

[65]: Koehne et al. (2013), “PROPOSAL: A tool for propagation of charged leptons”

[50]: Agostinelli et al. (2003), “Geant4—a simulation toolkit”

[47]: Rädel et al. (2012), “Calculation of the Cherenkov light yield from low energetic secondary particles accompanying high-energy muons in ice and water with Geant4 simulations”

[66]: Becherini et al. (2006), “A parameterisation of single and multiple muons in the deep water or ice”

[67]: Heck et al. (1998), “CORSIKA: A Monte Carlo code to simulate extensive air showers”

[68]: Gaisser (2012), “Spectrum of cosmic-ray nucleons, kaon production, and the atmospheric muon charge ratio”

[69]: Engel et al. (2017), “The hadronic interaction model Sibyll – past, present and future”

put a number on this significant increase? (YELLOW)

5.2 Detector Simulation

The detector simulation is performed after the event generation, where the initial particles and the resulting photons and secondary particles from their propagation were produced. This part of the simulation chain is applied to all muon and neutrino simulation as well as the HNL signal simulation explained in detail in Chapter 4. The detector simulation can be split into two parts, the propagation of the photons and the simulation of the detector response (including internal noise).

5.2.1 Photon Propagation

Any photon that was produced in the event generation is individually traced through the ice, simulating scattering and absorption processes. The

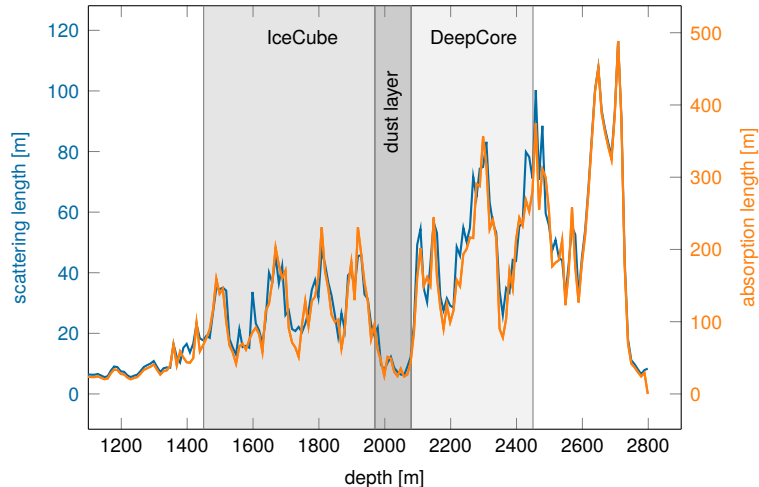


Figure 5.1: Scattering and absorption lengths in the SPICE model used for simulation production as a function of depth, modified from [73].

[71]: Chirkin et al. (2019), "Photon Propagation using GPUs by the IceCube Neutrino Observatory"

[72]: Aartsen et al. (2013), "Measurement of South Pole ice transparency with the IceCube LED calibration system"

put a number on the tilt angle? (YELLOW)

[74]: Mie (1908), "Beiträge zur Optik trüber Medien, speziell kolloidaler Metallösungen"

[75]: Henyey et al. (1941), "Diffuse radiation in the Galaxy."

1: A photon is absorbed, when it traveled its full absorption length, sampled in the initial step of the photon propagation.

[76]: Fiedlschuster (2019), "The Effect of Hole Ice on the Propagation and Detection of Light in IceCube"

propagation is done using `clsim` [70] which is an implementation of the *Photon Propagation Code (PPC)* [71] in OPENCL. It is optimized to be run very efficiently on GPUs, which is what is done for IceCube simulation production. The ice is modeled as a set of 10 m thick, almost horizontal layers with specific absorption and scattering lengths. The *South Pole ice (SPICE)* model [72] accounts for the layers being tilted by a small amount (°) and the absorption and scattering lengths having a non-uniformity with respect to the azimuth direction. Figure 5.1 shows the values of this model for the different depths, indicating the location of IceCube, DeepCore, and the dust layer.

In an initial step, each photon's absorption length is sampled from an exponential distribution with the expectation value at the current layer's absorption length. The following propagation steps are performed in parallel for all photons. In each of those steps, corresponding to a single scattering event, the photon travels a length that is sampled from an exponential distribution with the expectation value at the scattering length of the current layer and the scattering angle chosen based on a combination of a simplified Mie scattering distribution [74] and a Henyey-Greenstein distribution [75]. The parameters defining the shape of these distributions were calibrated using data from *in-situ* LED calibration runs. These steps are continuously repeated until each photon reached a DOM or was absorbed¹. After all photons have been propagated in that manner, the final step is to output the photons that reached a DOM for further processing.

5.2.2 Detector Responses

The second part of simulating the IceCube detector is the DOM response. Whether a photon that reached a DOM produces a signal depends on the total efficiency and the angular acceptance curve of the specific DOM. The total efficiency includes effects of the DOM glass, PMT quantum and photo-electron collection efficiencies, and it is wavelength dependent. Additionally, there is another angle dependent effect called *hole ice* [76]. This effect is due to varied ice properties resulting from the re-freezing process of the water column inside the borehole after deployment of the string. Accepted photons are converted into a so-called *Monte Carlo photo-electron (MCPE)*. The amount of charge measured for each MCPE is determined by sampling

from a mixture of two exponential distributions and a normal distribution. This *single photo-electron (SPE)* distribution was tuned to match the observed distribution in each DOM in an *in-situ* calibration study [77]. Figure ?? shows the distribution compared to a lab measurement. Based on the sampled charges and times of MCPEs, the voltage waveforms for the (two) different readout channels are simulated and passed on to the trigger simulation starting with *WaveDeform*, which was already mentioned in Section 3.1.1.

Besides the Cherenkov photons, IceCube also observes photons that are produced in radioactive decays inside the DOMs, both in the glass housing sphere and the PMT glass itself. To simulate this internal noise, the *Vuvuzela* module [78, 79] is used to create additional MCPEs that are fed into the same simulation chain described above. This module takes into account thermal and non-thermal components and their times are sampled using parameterizations of the measured distributions, where the thermal noise component is uncorrelated photons and the non-thermal component is from burst of photons. The noise hits are simulated by drawing the times from a constant rate Poisson process and the number of photons from a Poisson distribution. Then the time differences between the individual photons per hit is found, based on a Log-Normal distribution. The simulation is defined by 5 parameters that are calibrated for each DOM individually. Table 5.2 shows the average values for these parameters.

[77]: Aartsen et al. (2020), “In-situ calibration of the single-photoelectron charge response of the IceCube photomultiplier tubes”

Add SPE distribuiton plot (RED)

| Parameter | Value |
|-----------------------------------|----------------------------|
| Therm. rate λ_{th} | 180 Hz |
| Decay rate λ_{dec} | 80 Hz |
| Decay hits η | 8.5 |
| Decay μ | $4.3 \log_{10}(\text{ns})$ |
| Decay σ | $1.8 \log_{10}(\text{ns})$ |

Table 5.2: Typical parameter values used in the vuvuzela noise simulation. Averaged over all DOMs.

[78]: Larson (2013), “Simulation and Identification of Non-Poissonian Noise Triggers in the IceCube Neutrino Detector”

[79]: Larson (2018), “A Search for Tau Neutrino Appearance with IceCube-DeepCore”

5.3 Processing

After the detector simulation is performed, all MC and data are processed in exactly the same way. This section explains the trigger and event selection that is applied starting from the raw voltage measured by the PMTs. Most parts of this processing are identical to the procedure already described in [73, 80]. It is split in different steps run inside the ice, at the South Pole, and after the data was transferred to the North. The complexity and computational cost of the processing increases with each step, while the total number of events reduces, making it feasible and reducing the use of computational resources on events that are not of interest for the analysis.

[73]: Trettin (2023), “Search for eV-scale sterile neutrinos with IceCube DeepCore”

[80]: Lohfink (2023), “Testing non-standard neutrino interaction parameters with IceCube-DeepCore”

5.3.1 Trigger and Filter

Before the data can be sent to the North, the initial signal coming from the PMT is a voltage waveform that has to be digitized (for data) and then information of photon hits has to be extracted (also for the MC coming from the detector response simulation). The trigger and filter explained here are tailored to select events that passed through the DeepCore volume, while rejecting background events (either from atmospheric muons or from random noise). There are other filters used in IceCube which will not be explained here, since they are not relevant for this work. A full description of the instrumentation and the online systems can be found in [81].

Include some low level plots like the trigger efficiency for the HNL simulation (ORANGE)

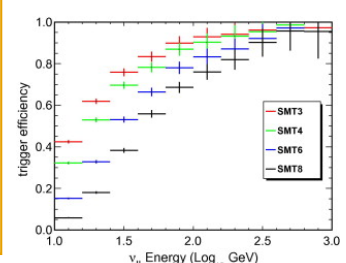


Figure 5.2: Efficiencies of different IceCube and DeepCore triggers, taken from [43].

In-ice Trigger

The trigger is applied inside the DOM in the ice before sending the information to the ICL on the surface. The time dependent voltage curves are

[39]: Abbasi et al. (2009), “The IceCube data acquisition system: Signal capture, digitization, and timestamping”

[6]: Aartsen et al. (2017), “The IceCube Neutrino Observatory: instrumentation and online systems”

[43]: Abbasi et al. (2012), “The design and performance of IceCube DeepCore”

captured if a pre-defined threshold value is exceeded. Once the threshold set to the equivalent of 0.25 PE is crossed, 6.4 μs of the waveform are coarsely digitized by a *Fast Analog-to-Digital Converter* (*FADC*) with a sampling rate of 40 MHz. Additionally, the first 427 ns are digitized using an *Analog Transient Waveform Recorder* (*ATWD*) with a sampling rate of 300 MHz [39], but only if some trigger condition is met, because this readout frequency is too high to be sampled directly and requires some buffering. For DeepCore, the HLC condition already mentioned in Section 3.1.1 has to be met for three DOMs inside the fiducial volume within a time window of 5 μs . If this is the case, all waveforms that crossed the threshold within a 20 μs time window around the trigger are digitized and sent to the ICL for further processing. This trigger is called *Simple Multiplicity Trigger 3* (*SMT-3*). The DOM hits that are read out in this process, but do not meet the HLC condition, are called *soft local coincidence* (*SLC*) hits. The rate of the DeepCore SMT-3 trigger is \sim 250 Hz [6], accepting \sim 70 % of ν_μ -CC events at 10 GeV and \sim 90 % at 100 GeV [43]. The trigger efficiencies for different SMT triggers, including the DeepCore SMT-3, are shown in Figure 5.2.

Online Filter

2: Where *online* means running on hardware at the South Pole.

The digitized waveforms are sent to the ICL, where a further filter is applied *online*². First, the WaveDeform algorithm is run to extract photon arrival times and charge from the waveforms, then the DeepCore filter is applied, which is an iterative hit cleaning starting from HLC hits and removing any hits outside a 125 m radius and a 500 ns time window (called *radius-time cleaning* (*RT-cleaning*)) of the initial hit. This mainly rejects unphysical SLC hits, which are potentially caused by random noise. The following selection steps are done using the resulting cleaned pulses.

Next, an additional cut is applied to reject events that are likely to be caused by atmospheric muons. This is done by splitting the hits depending on whether they were inside the DeepCore fiducial volume or outside and then calculating the speed of each hit outside the fiducial volume towards the *center of gravity* (*COG*) of the hits inside. If one of them has a speed close to the speed of light, the whole event is rejected, because this is a strong indication for a muon event.

As input for the further selection levels, a few event properties, like vertex position and direction, are determined using fast and simple event reconstructions. After the DeepCore online filter, the rate is about 15 Hz, which can be sent to the North via satellite for further processing.

5.3.2 Event Selection

After the data was sent to the North, the *offline* filters and selection are applied to further reduce the background of atmospheric muons and noise. The selection is split into three levels referred to as *Level 3-5* (*L3-L5*), which bring down the neutrino and muon rate to \sim 1 mHz, while the remaining fraction of random noise is below 1 %.

Level 3

At the first offline filtering level, Level 3, 1D cuts are used to reduce atmospheric muons, pure noise, and coincident muons. These cuts are targeting regions where the data/MC agreement is poor, so that more sophisticated *machine learning (ML)* techniques can be applied at later levels. The cuts are made using 12 control variables, that are inexpensive to compute for the very large sample at this stage. The variables are related to position, time, and overall number of hits in the event.

Pure noise hits, that are temporally uncorrelated, are cleaned by applying a 300 ns sliding window, requiring the containment of more than 2 hits at its maximum. Additionally, an algorithm is run to check whether the hits show some directionality, accepting them only if they do.

To reduce the amount of muons a series of cuts is applied using spatial and temporal information. Events that have more than 9 hits observed above -200 m or the first HLC hit above -120 m are rejected as well as events where the fraction of hits in the first 600 ns of the event is above 0.37, ignoring the first two hit DOMs. Additionally, the ratio between hits in the veto region and the DeepCore fiducial volume is required to be below 1.5.

If a muon enters the detector after the data acquisition was already triggered, it causes events that span over a much larger time range. To reduce those coincident events, the time difference between first and last pulse cannot be above 5000 ns. This cut mainly affects a region of very poor data to MC agreement, because coincident events are not simulated at all.

The L3 cuts remove 95 % of the atmospheric muons and >99 % of pure noise hits, while keeping >60 % of the neutrino events. The sample now roughly contains muons/neutrinos/noise at a ratio of 100:10:1 with a total rate of $\sim 0.5\text{ Hz}$.

add example plots (2?)
for L3 cut variables and
applied cuts (YELLOW)

Level 4

After the total rate was reduced by the simple cuts of L3 and the overall agreement between data and MC is established, ML techniques can be applied to further reduce the background. For Level 4, two *Boosted Decision Trees (BDTs)* [82] classifier are trained to separate neutrino events from atmospheric muons and noise hits, separately. The output of each classifier, a probability score, can be seen in Figure 5.3. The noise filter is applied first and an event passes the score if it is larger than 0.7, reducing the noise hits by a factor of 100, while keeping 96 % of neutrinos. Then the second BDT classifier is applied to reject muons. It was trained partly on unfiltered data, which consists of >99 % atmospheric muons, to reject the data and keeping the neutrinos from the simulation. Rejecting events with a score smaller than 0.65 removes 94 % of atmospheric muons while keeping 87 % of neutrinos. This fraction varies depending on the flavor and interaction type, ν_μ -CC events for example, which have a muon in the final state, are therefore reduced to 82.5 %. After applying the L4 cuts based on the BDT classifier outputs, the sample is still dominated by atmospheric muons, while the noise rate dropped to below most neutrino types.

[82]: Friedman (2002), “Stochastic gradient boosting”

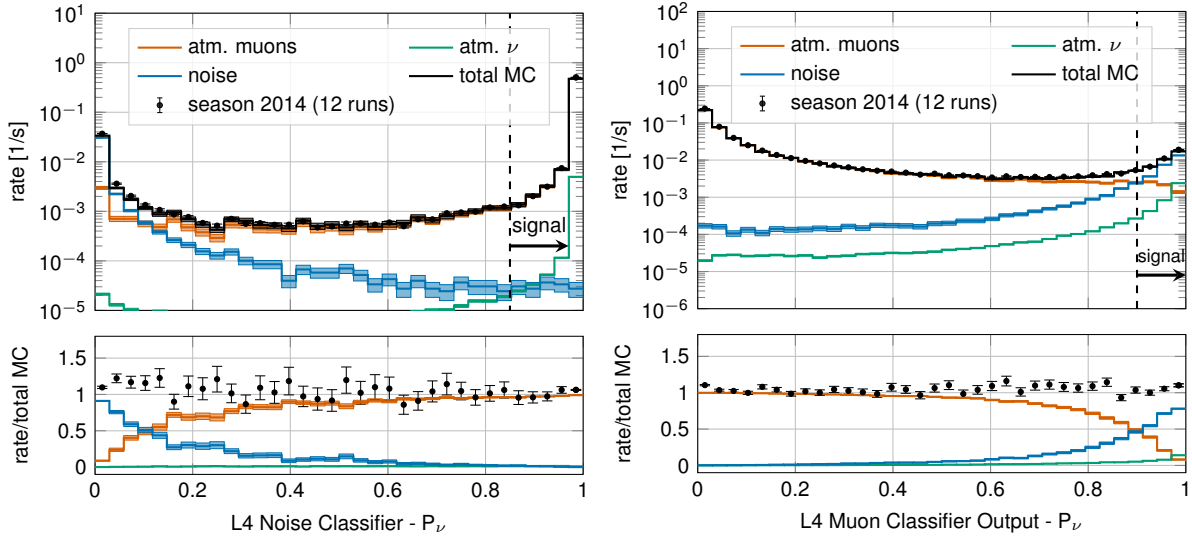


Figure 5.3: Distributions of Level 4 noise classifier output (left) and muon classifier output (right), where larger values indicate more neutrino-like and lower values more noise-like/muon-like. Taken from [61].

Level 5

Level 5 is the final selection level, before event reconstructions are applied. This level aims to reduce the remaining atmospheric muon rate below the rate of neutrinos. Muons not rejected by the earlier levels are those that produced little or no light in the veto regions. One possible reason is that they passed through one of the un-instrumented regions between the strings called *corridors*. To reject those, special corridor cuts, based on the number of hits they produced close to a potential corridor they passed through. The potential corridor in question is identified based on a simple infinite track fit. In addition to the corridor cuts, starting containment cuts are applied to reject events that start at the edge of the fiducial volume. Events with more than seven hits in the outermost strings of the detector or those that have a down going direction in the uppermost region are rejected. This further reduces the fraction of muons by 96 % while keeping 48 % of neutrinos. The rates after this level are 1 mHz and 2 mHz for neutrinos and muons, respectively, making it a neutrino dominated sample.

add some figure showing the corridors? (YELLOW)

add table with rates per level (split in flavor) - maybe better in analysis chapter to also show signal? (RED)

5.4 Reconstruction

[83]: Abbasi et al. (2022), "Low energy event reconstruction in IceCube DeepCore"

[61]: Abbasi et al. (2023), "Measurement of atmospheric neutrino mixing with improved IceCube DeepCore calibration and data processing"

[84]: Yu et al. (2023), "Recent neutrino oscillation result with the IceCube experiment"

In the energy range most relevant for this work, between 10 GeV and 100 GeV, the light deposition is very low and only a few DOMs detect light, making the reconstructions difficult. In [83] two classical methods are described, which have partly been applied in one recent IceCube atmospheric neutrino oscillation measurement using a sub-sample of the DeepCore sample [61]. The algorithm used in this work on the other hand, is a newer method that applies a *convolutional neural network* (CNN) to reconstruct the events and determine some discriminating quantities. The latest muon neutrino disappearance result from IceCube [84] is based on this reconstruction.

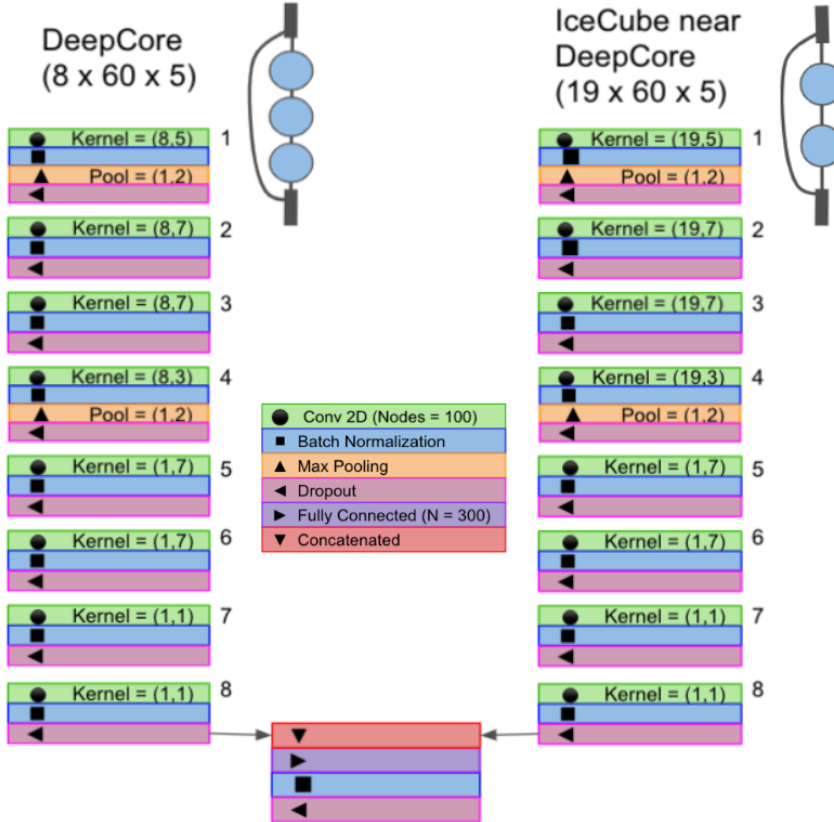


Figure 5.4: Architecture of the FLERCNN neural networks, taken from [85].

5.4.1 Fast Low Energy Reconstruction using Convolutional Neural Networks

As the name *Fast Low Energy Reconstruction using Convolutional Neural Networks (FLERCNN)* already indicates, the FLERCNN reconstruction [85, 86] is a CNN optimized to reconstruct IceCube events at low energies ($< 100 \text{ GeV}$) in a fast and efficient manner, by leveraging the approximate translational invariance of event patterns within the detector. The architecture of the network is very similar to the preexisting IceCube CNN event reconstruction [87], but optimized on low energy events and specifically tailored to include the DeepCore sub-array. Only the eight DeepCore strings and the central 19 IceCube strings are used for the reconstruction (compare to Figure 3.4). Because of the different z-positions of the DeepCore and IceCube DOMs, they are divided into two networks that are combined in the final layer of the network. The full architecture is shown in Figure 5.4. The first dimension of the network is the string index, while the second dimension is the order of the DOMs along the vertical axis. The horizontal position of the DOMs is not used, since the strings are arranged in an irregular pattern. The information from the DOM hits is summarized into five charge and time variables, which make up the last dimension of the input layer. The variables are the total summed charge, the time of the first hit, the charge weighted mean time of the hits, the time of the last hit, and the charge weighted standard deviation of the hit times.

Five different networks are trained using this architecture. Three networks do the regression of the events' energy, zenith angle, and the starting vertex (x, y, z position), while two of them are used for classification. One is trained to predict the probability of the event being a track (used as PID) and the

[85]: Yu et al. (2021), "Direction reconstruction using a CNN for GeV-scale neutrinos in IceCube"

[86]: Micallef (),

[87]: Huenefeld (2017), "Deep Learning in Physics exemplified by the Reconstruction of Muon-Neutrino Events in IceCube"

add image with selected strings used for flercnn
IC and DC (YELLOW)

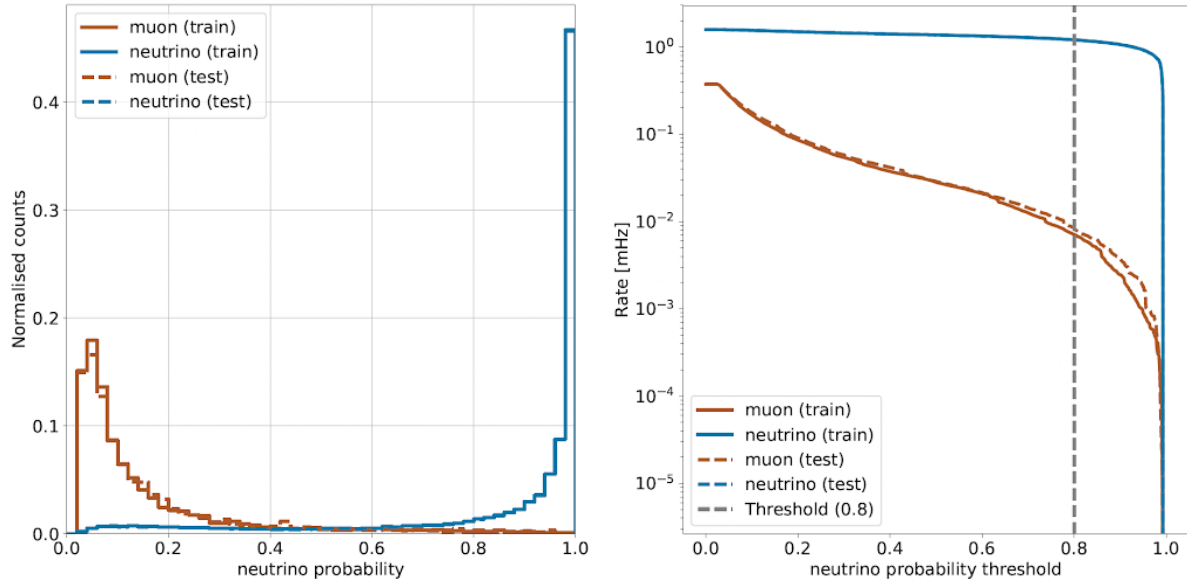


Figure 5.5: FLERCNN muon classifier output score (left) and rate of neutrinos and muons as function of muon classifier cut (right). Taken from [flercnn_analysis_internal_note]

other to predict the probability of the event being a muon. Each network is trained with an MC sample modified to have a flat distribution in the target variable, to be unbiased for that variable and ideally extending outside the target reconstruction region. For the classification tasks the loss function is the *binary cross entropy* and the activation function is a *sigmoid*. To perform the regression of zenith and vertex position, the loss function is the *mean squared error (MSE)*, while for the energy it is the *mean absolute percentage error*. The activation for all regression tasks is *linear*.

add some performance plots of the FLERCNN reconstruction (ORANGE)

There is more information on pre-processing the samples and preparing the input features, and training each cnn, but I'm not sure if that might be too much detail? (YELLOW)

3: A radial variable that is often used in IceCube, is the horizontal distance to string 36 called ρ_{36} , which is basically the distance to the center of IceCube.

add reference for flercnn analysis internal note (ORANGE)

5.4.2 Analysis Selection

Before the reconstruction is applied a few additional high level variables are computed, which are from fast and inexpensive algorithms. Then the reconstruction is performed by applying the trained FLERCNN networks to get the output quantities. After that, another BDT classifier is trained to further reduce the muon background for the final sample. The BDT is trained on five high level variables, where three are FLERCNN reconstruction variables (vertex z , ρ_{36}^3 and muon probability) and two are lower level variables (L4 muon classifier output and L5 corridor cut variable). To train the BDT, the FLERCNN nominal simulation set is used, only using events with $\cos(\theta_{\text{zenith}}) \leq 0.3$. The output of the BDT is the neutrino probability and a cut at 0.8 is applied to reject events with a high probability of being a muon. Figure 5.5 shows the output of the BDT classifier, where the neutrinos in both training and testing sets are gathered at 1 and muons are around 0, which shows great classification power.

To get the final, pure sample of well reconstructed neutrinos another set of cuts is applied. The first cuts are meant to reject events with poor reconstruction quality, by requiring the events to fall into the DeepCore volume, where the denser, better instrumented detector leads to enhanced resolution. The cuts are applied on the vertex z and ρ_{36} and are listed in Table 5.3. The FLERCNN reconstruction was optimized for atmospheric

| Variable | Threshold | Removed |
|-------------------------------|---------------------------------------|---------|
| Number of hit DOMs | ≥ 7 | 1.05 % |
| Radial distance | $< 200 \text{ m}$ | 0.09 % |
| Vertical position | $-495 \text{ m} < z < -225 \text{ m}$ | 5.48 % |
| Energy | $5 \text{ GeV} < E < 100 \text{ GeV}$ | 20.70 % |
| Cosine of zenith angle | < 0.04 | 19.66 % |
| Number of direct hits | > 2.5 | 10.50 % |
| Number of hits in top layers | < 0.5 | 0.03 % |
| Number of hits in outer layer | < 7.5 | 0.001 % |
| Muon classifier score | ≥ 0.8 | 23.90 % |

Table 5.3: Cuts performed to select the final analysis sample. Parts of the cuts are meant to increase the data/MC agreement, while others are meant to reject events with poor reconstruction quality.

neutrino analyses which are mainly in the region below 100 GeV and there are very few events with energies below 5 GeV, so the reconstructed energy is required to be in that range. Additionally, rejecting events with fewer than seven hits in the selected DOMs used for FLERCNN showed to increase the resolution.

Another set of cuts is applied to make sure the agreement between data and MC is good. To remove coincident muon and neutrino events, cuts are applied to the number of hits in the top 15 layers of IceCube DOMs and the number of hits in the outermost IceCube strings. Coincident random noise events are removed by requiring more than three hit DOMs from direct photons⁴. Neither of the two coincident event types are simulated, which can be seen as bad agreement between data and MC. The last cut is on the reconstructed cosine zenith, which is required to be smaller than 0.04 to reject down-going muons.

4: *Direct photons* are photons that were not scattered on their way from the interaction vertex to the DOM.

5.5 Systematic Uncertainties

There are multiple sources of systematic uncertainties related to the event generation and processing explained in this chapter. All uncertainties considered in this work are implemented with parameters that can be varied continuously so that a simultaneous fit of the physics and systematic parameters can be performed. Where possible, a correct model of the effect is used, but in many cases the variations are captured by effective parameters. Uncertainties that solely scale the total event rate are not included individually, since the analysis only uses the relative distribution of events and a single scaling parameter N_ν is used to scale the total neutrino rate instead.

SB: I think its better to discuss the sources of uncertainty when you introduce each component, e.g. when you talk about cross-sections you can explain the existing measurements and models, and how the uncertainty is derived. Same for the detector calibration uncertainties - you can discuss the magnitude of the errors and how they are derived when you discuss the detector. (ORANGE)

5.5.1 Atmospheric Flux Uncertainties

The flux of atmospheric neutrinos is influenced by multiple factors, the spectrum and composition of CRs, the assumed atmospheric conditions, and the HI model used to describe the air showers development. Uncertainties of the neutrino flux are therefore dictated by the uncertainties on these components, where the variations in atmospheric conditions were found to have negligible effect [61].

Cosmic ray flux: The selected sample of atmospheric neutrinos lies around energies of up to 100 GeV. The initial primary particles in the CR flux can have 100 times larger energies and therefore the CR flux between 10 GeV and 10 TeV is important, which dominantly consists of hydrogen and helium

[61]: Abbasi et al. (2023), “Measurement of atmospheric neutrino mixing with improved IceCube DeepCore calibration and data processing”

[88]: Dembinski et al. (2017), “Data-driven model of the cosmic-ray flux and mass composition from 10 GeV to 10^{11} GeV”

[89]: Barr et al. (2006), “Uncertainties in atmospheric neutrino fluxes”

[90]: Evans et al. (2017), “Uncertainties in atmospheric muon-neutrino fluxes arising from cosmic-ray primaries”

[61]: Abbasi et al. (2023), “Measurement of atmospheric neutrino mixing with improved IceCube Deep-Core calibration and data processing”

[92]: Barr et al. (2006), “Uncertainties in Atmospheric Neutrino Fluxes”

add figure with Barr blocks? (RED)

[93]: Riehn et al. (2020), “Hadronic interaction model sibyll 2.3d and extensive air showers”

[88]: Dembinski et al. (2017), “Data-driven model of the cosmic-ray flux and mass composition from 10 GeV to 10^{11} GeV”

5: The choice of flux and HI model have minor impact on the variations.

which experiments measure the axial mass? (ORANGE)

nuclei [88]. The uncertainty in this CR flux component can be described as a power law correction [89, 90]

$$\Phi'_\nu = \Phi_\nu \left(\frac{E}{E^*} \right)^{\Delta\gamma}, \quad (5.2)$$

where E^* is the pivot energy and $\Delta\gamma$ is the correction to the power law exponent. This modification propagates into the neutrino flux, which is therefore corrected in the same way. E^* was chosen to be 24 GeV as to minimize the dependence of the overall flux scale on $\Delta\gamma$ [61].

Hadronic interaction model: Neutrinos are produced in the decaying hadrons in CR air showers, spanning a large parameter space that is sparsely evaluated by experimental data. To include uncertainties based on energy, direction, and neutrino flavor, the MCEq package [91] is used to compute the distribution of atmospheric leptons and to estimate the impact of varying their contributions. The calculations result in the change in flux $d\Phi_l/dB$ for a variation dB of some parameter B . Scaling this variation by some value b , the modified total flux, s is then given by

$$\Phi'_l = \Phi_l + \left(b \cdot \frac{d\Phi_l}{dB} \right). \quad (5.3)$$

Matching the work in [92], the parameter space is divided in regions of the primary energy E_i and the energy fraction of the secondary meson x_{lab} , with varying uncertainties, derived from fixed target experiment data. The Sibyll2.3c [93] HI model and the GSF CR flux [88] were used to calculate the related flux changes⁵ for the different regions in E_i and x_{lab} , resulting in 17 variables, encoding the possible changes.

5.5.2 Cross-Section Uncertainties

The uncertainties related to the cross-sections are split into low and high energy components, since there is no coherent model to explain both DIS interactions, which are the dominant processes above 20 GeV, and *charged current resonance production* (CCRES) and *charged current quasi elastic scattering* (CCQE), which are relevant below 20 GeV where interactions with the nucleons as a whole are important. Three parameters are included to account for all relevant cross-sections uncertainties.

At low energies two parameters are included accounting for uncertainties in form factors of CCQE and CCRES events. These uncertainties are due to uncertainties in the *axial mass* M_A , which enters the form factor as in

$$F(Q^2) \sim \frac{1}{(1 - (\frac{Q}{M_A})^2)^2}, \quad (5.4)$$

where Q^2 is the momentum transfer squared. The axial mass can be determined experimentally and to include uncertainties on the values of M_A^{CCQE} and M_A^{CCRES} , the cross-sections are computed with GENIE, where the form factors are calculated varying the axial mass by $\pm 20\%(1\sigma)/\pm 40\%(1\sigma)$ around the nominal value. This is an approximation of the recommended uncertainties by the GENIE collaboration, which are -15% , $+25\%$ for M_A^{CCQE} and

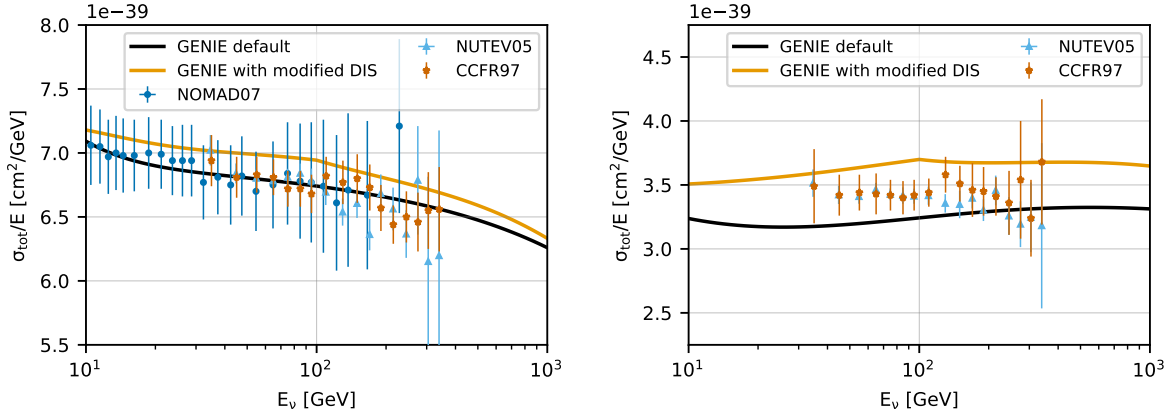


Figure 5.6: Inclusive total neutrino-nucleon cross-sections on an isoscalar target (black) for neutrinos (left) and antineutrinos (right) calculated with GENIE, comparing to measurements from NOMAD [95], NUTEV [96], and CCFR [97]. The scaled GENIE cross-section (orange) is also shown. Taken from [61].

$\pm 20\%$ for M_A^{CCRES} [62]. To apply a continuous uncertainty variation of the axial mass in a fit, the total cross-section is fit with a quadratic function to interpolate between the cross-sections computed with the different axial masses.

Even though the DIS interactions can be calculated very precisely, there are still uncertainties in the input PDF, describing the probability of finding a specific parton (quark) with a specific momentum fraction x inside a nucleon. To account for differences between the used method and more sophisticated methods using newer PDFs seen at high energies, an uncertainty parameter is introduced. The parameter is based on the discrepancy between the cross-sections computed with GENIE and the ones computed with CSMS [94] above 100 GeV. The included parameter scales the cross-section from the GENIE values to the CSMS values, which are considered more accurate above 100 GeV. The scaling is done as a function of energy and inelasticity and to guarantee continuity, the scaling is extrapolated linearly below 100 GeV. The parameter is designed such that a value of 0.0 corresponds to the GENIE cross-sections and a value of 1.0 gives an approximation of the CSMS cross-sections. A comparison of the total cross-sections GENIE (scaled/unscaled) with the data is shown in Figure 5.6.

[94]: Cooper-Sarkar et al. (2011), “The high energy neutrino cross-section in the Standard Model and its uncertainty”

5.5.3 Detector Calibration Uncertainties

There are multiple sources of systematic uncertainties related to the detection process of neutrinos in IceCube. Dominant for this analysis are the effects of the properties of the ice itself and the optical efficiency of the DOMs. None of these uncertainties can be described by an analytic expression, so they have to be estimated using MC simulation. The method used to derive the continuous variations based on the MC simulation is described in Section 7.2.4. The five relevant uncertainty parameters are the absolute efficiency of the DOMs, a global scaling of bulk ice scattering and absorption lengths, and variations of the relative angular acceptance due to hole ice variations in two parameters.

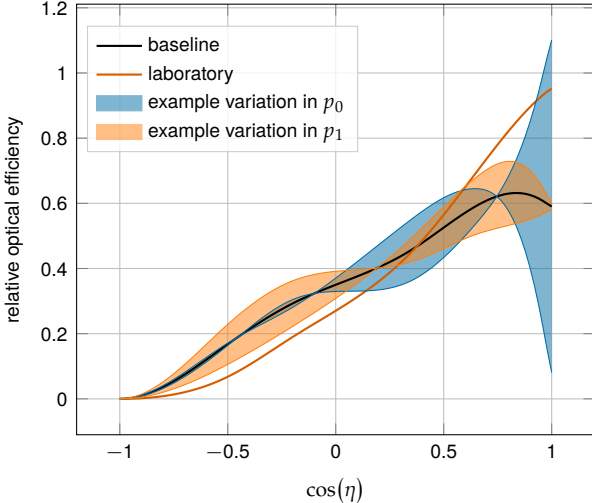


Figure 5.7: Relative angular acceptance modification due to hole ice. Shown is the current baseline model, the variations from changing p_0 and p_1 , and a laboratory measurement. Modified from [73].

[41]: Feintzeig (2014), “Searches for Point-like Sources of Astrophysical Neutrinos with the IceCube Neutrino Observatory”

[42]: Kulacz (2019), “In Situ Measurement of the IceCube DOM Efficiency Factor Using Atmospheric Minimum Ionizing Muons”

[98]: Rongen, Martin (2016), “Measuring the optical properties of IceCube drill holes”

6: The hole ice angular acceptance modification is normalized so that it does not affect the total charge.

DOM efficiency: As was already mentioned in Section 3.1.1, the absolute efficiency of the DOMs, ϵ_{DOM} is calibrated using minimum ionizing muons from air showers, due to the lack of a calibrated light source in the detector. Using the muons as a steady, controlled source of light, the efficiency can be estimated by comparing simulated muon data sets with varied DOM response to the measured data. Since the uncertainties found in multiple iterations of this study [41, 42] are at the order of 10 %, this systematic is highly relevant and has to be included in the analysis.

Bulk ice scattering and absorption: Absorption and scattering length are the most important properties that govern the propagation of photons through the ice. The simulation principle and how the depth dependent absorption and scattering coefficients are used was already explained in Section 5.2.1. To account for uncertainties on this model of the bulk ice coefficients, a global scaling for each of the two parameters (global absorption, global scattering) is applied.

Hole ice angular acceptance: Due to bubble formation in the re-freezing process of the boreholes, the hole ice seems to be less transparent in the center of the columns [98]. This effectively decreases the chance of photons hitting the DOMs directly from below, which can be described as an additional angular modification of the DOM acceptance. The modification is parameterized by a two dimensional, normalized⁶ function, where the two dominant of the parameters (p_0, p_1), dictating its form, are enough to describe all past and the current hole ice models from both *in-situ* and laboratory measurements. Figure 5.7 shows the acceptance modification as a function of the incident photon angle $\cos(\eta)$. The current baseline model, the variations achieved through modifying p_0 and p_1 , and a laboratory measurement can be seen.

5.5.4 Muon Uncertainties

The muon fraction in the final level selection (see Section 5.4.2) is below 1 %, therefore additional muon systematic uncertainties apart from the spectral index are not implemented, but rather a total muon scaling parameter is

added. This total scale is somewhat degenerate with the DOM efficiency, since an increased DOM efficiency leads to better muon rejection. Both the total muon scaling and the muon spectral index have a very small impact on the analysis as will be shown in Section ??.

cite this? (YELLOW)

Detecting Low Energetic Double Cascades

6

6.1 Reconstruction

All existing reconstruction algorithms applied for low energetic atmospheric neutrino events mentioned in Section 5.4 are either assuming a single cascade hypothesis or a track and cascade hypothesis, which are the two SM morphologies observable at these energies, as was described in Section 3.3. A HNL being produced and decaying inside the IceCube detector however, will produce two cascade like light depositions. The morphology and how the cascade properties and their spatial separation depend on the model parameters was introduced in Section ???. To investigate the performance of the detector to observe these events, a low energetic double cascade reconstruction algorithm was developed, based on a pre-existing algorithm used to search for double cascades produced from high energetic astrophysical tau neutrinos [99] that was established in [100], but first mentioned in [101].

6.1.1 Table-Based Minimum Likelihood Algorithms

The reconstruction is relying on a maximum likelihood algorithm, which is the *classical* approach to IceCube event reconstructions, as opposed to ML based methods. A Poissonian likelihood is constructed, which compares the observed photon numbers, n , with their arrival times to the expected light depositions, μ , for a given even hypothesis as

$$\ln(L) = \sum_j \sum_t n_{j,t} \cdot \ln(\mu_{j,t}(\Theta) + \rho_{j,t}) - (\mu_{j,t}(\Theta) + \rho_{j,t}) - \ln(n_{j,t}!) , \quad (6.1)$$

where ρ are the number of expected photons from noise, Θ are the parameters governing the source hypothesis, and the likelihood is calculated summing over all DOMs j splitting observed photons into time bins t . The light expectations are calculated using look-up tables [56] that contain the results from MC simulations of reference cascade events or track segments. By varying the parameters defining the event hypothesis, the likelihood of describing the observed light pattern by the expected light depositions is maximized to find the reconstructed event. Algorithms of this kind used in IceCube are described in great detail in [40]. For the table production a specific choice of ice model has to be made, while the calibrated DOM information is taken from the measurement itself.

Based on the tabulated light expectations for cascades and track segments, various event hypothesis can be constructed, like the common cascade only or the track and cascade hypotheses. The hypothesis describing the double cascade signature of the HNL is using two reference cascades that are separated by a certain distance. The whole hypothesis is defined by 9 parameters and assumes that the two cascades are aligned with each other, which is a safe assumption for strongly forward boosted interactions. The parameters are the position of the first cascade x, y, z , the direction of both

| | | |
|-----|---|----|
| 6.1 | Reconstruction | 53 |
| 6.2 | Double Cascade Classification | 60 |
| 6.3 | Generic Double Cascade Performance . . | 60 |

[99]: Abbasi et al. (2020), “Measurement of Astrophysical Tau Neutrinos in IceCube’s High-Energy Starting Events”

[100]: Usner (2018), “Search for Astrophysical Tau-Neutrinos in Six Years of High-Energy Starting Events in the IceCube Detector”

[101]: Hallen (2013), “On the Measurement of High-Energy Tau Neutrinos with IceCube”

maybe I want a figure for this, or not so important? (YELLOW)

[56]: Whitehorn et al. (2013), “Penalized splines for smooth representation of high-dimensional Monte Carlo datasets”

[40]: Aartsen et al. (2014), “Energy Reconstruction Methods in the IceCube Neutrino Telescope”

Elaborate whether this is the case (show it in a plot?). Discuss directionality of cascades in general. (ORANGE)

cascades ϕ, θ , and its time t as well as the decay length L between the two cascades. Assuming the speed of the HNL to be the speed of light, c , this already defines the full signature. The HNL particle does not produce any light while traveling, as it is electrically neutral. The full 9 parameters describing the event are $\Theta = (x, y, z, t, \theta, \phi, E_0, E_1, L)$. To compute the full likelihood the term in Equation 6.1 is summed over both cascade parts, i , as $\sum_i \ln(L_i)$.

6.1.2 Optimization for Low Energy Events

Optimizing the double cascade reconstruction for low energetic events was done in parallel to the development of the model dependent simulation generator introduced in Section 4.2. A preliminary sample of HNL events was used, containing a continuum of masses between 0.1 GeV and 1.0 GeV and lab frame decay lengths sampled uniformly in the range from 5 m to 500 m. Even though this sample is not representative of a physically correct model and therefore not useful to predict the event expectation, it can still be used to optimize the reconstruction. The double cascade nature of the individual events and the evenly spaced decay length distribution are especially useful for this purpose.

[83]: Abbasi et al. (2022), “Low energy event reconstruction in IceCube DeepCore”

The simulation is processed up to Level 5 of the selection chain described in Section 5.3.2 and one of the reconstructions from [83] is applied to the events, fitting a cascade and a track and cascade hypothesis. The results from this reconstruction are used as an input for the double cascade reconstruction, where the position of the vertex, the direction of the event, and its interaction time are used as the input quantities for the first cascade, and the length of the track reconstruction is used as a seed for the distance between the two cascades.

Decay Length Seeds

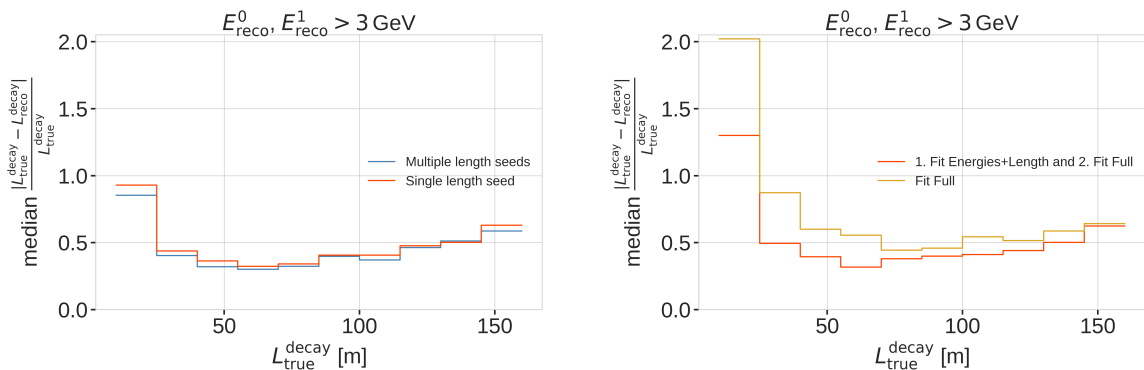


Figure 6.1
fix caption of this figure
(RED)

The full 9 dimensional likelihood space is very complex and can have many local minima, depending on the specific event and its location in the detector. Especially the seed value of the length between the two cascades was found to have a very strong impact on whether the global minimum was found during the minimization. To mitigate this effect, multiple fits are performed, seeding with variations of the input length at different orders of magnitude.

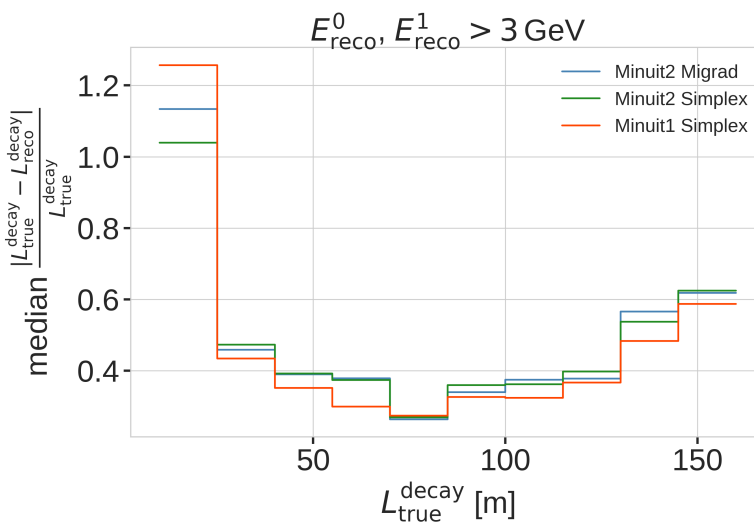
The best result is used, selected based on the total likelihood value of the best fit parameter set. A small improvement in the decay length resolution can be found by using this approach as compared to a single length seed. The effect can be seen in the left part of Figure 6.1, which shows the median, absolute, fractional decay length resolution.

Fit Routine

Because the length seed showed to have such a large impact on the reconstruction performance, a more sophisticated fit routine, than just fitting all 9 parameters at once, was tested. In a first fit iteration, some parameters are fixed and the resulting best fit point is used to fit all 9 parameters in a second iteration. In the right part of Figure 6.1 it can be seen how a fit split into two consecutive steps, where the first step fits only both cascade energies and the decay length and the second step fits the full 9 parameters, performs better as compared to a single, full 9 parameter fit. The initial seed for both routines is the same.

Minimizer Settings

To investigate the effect of the minimizer used to find the best fit parameters, the reconstruction was performed using three different minimizers, which were easily accessible within the reconstruction framework. The minimizers used were Minuit1 Simplex, Minuit2 Simplex, and Minuit2 Migrad. The results can be seen in Figure 6.2, where the Minuit1 Simplex minimizer performs best. The initial idea was to test a global minimizer, or a routine that can find the rough position of the global minimum first and then a local minimizer to find the exact minimum, but unfortunately this was not possible with the minimizers available in the framework. From the three tested minimizers, Minuit1 Simplex performed best and was chosen as the default for the reconstruction. The comparison of the decay length resolutions can be seen in Figure 6.2.



fix caption of this figure
(RED)
Figure 6.2: title

6.1.3 Performance

The chosen reconstruction chain used to test the performance of the detector to observe low energetic double cascades is the following; Minuit1 Simplex is used as the minimizer, the decay length is seeded with 3 different values, 0.5x, 1.0x, and 1.5x the length of the track reconstruction, and the fit routine is split into two steps, where the first step fits the energies and the decay length and the second step fits the full 9 parameters. In the first step, the number of time bins in Equation 6.1 is set to 1, so just the number of photons and their spatial information is used. The second step is seeded with the best results from the first fit and here the number of time bins is chosen such that each photon falls into a separate time bin, which means all time information is used. The average runtime per event is ~ 16 s on a single CPU core, but is very dependent on the number of photons observed in the event, since the likelihood calculation in the second step scales with this number and a table lookup has to be performed for each photon.

To get a more realistic estimate of the reconstruction performance, it is run on a second preliminary sample of HNL events, containing masses between 0.1 GeV and 3.0 GeV and the lab frame decay length is sampled from an inverse distribution in the range from 1 m to 1000 m, which is a better approximation of the expected exponential decay distribution of the HNL. The performance is shown for events where the reconstruction chain was successfully run, the event selection criteria up to level 7 are fulfilled, and the reconstructed energy of both cascades is above 3.0 GeV. This is done to only investigate well reconstructed events with two significant light depositions at a usual final selection level of the oscillation analyses.

one half sentence on why
this number was chosen?
(ORANGE)

Energy Resolutions

The energy resolution is inspected by looking at the 2-dimensional distribution of reconstructed energy versus the true energy as shown in Figure 6.3. The bin entries are shown as well as the median and $\pm 25\%$ calculated per vertical column, to get an idea of the distribution for a given energy slice. The color scale is showing the PDF along in each true energy slice, which is the full information combined into the median $\pm 25\%$ lines. The reconstructed energy is only the energy that is observable from photons, while the true energy is the total cascade energy, including the parts that go into EM neutral particles that do not produce light. It is therefore not expected that the median lines up with the axis diagonal, but rather the reconstructed energy is going to be lower.

The histogram for the first cascade energy is shown on the left and above an energy of ~ 10 GeV the reconstruction performs well, with the median being parallel to the diagonal and the spread in the $\pm 25\%$ quantile being small. Below this energy the reconstruction is over-estimating the true energy, which is a known effect in IceCube, where the reconstruction is biased towards higher energies around the energy detection threshold, because events that enter the sample are events with an over fluctuation in their light deposition, which makes them pass into the selection and being reconstructible in the first place.

For the second cascade the overall behavior is similar, only that the energy where the reconstruction starts to perform good is higher around ~ 20 GeV.

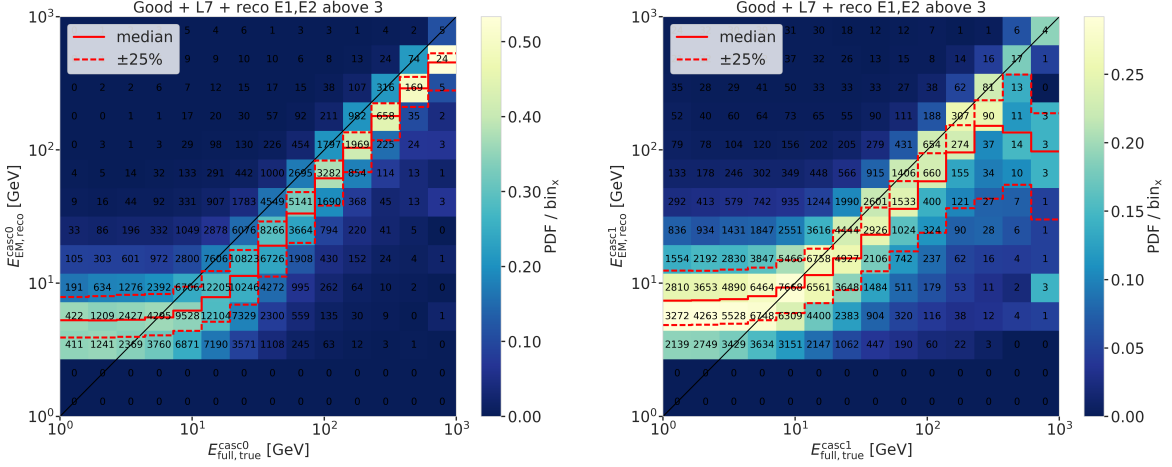


Figure 6.3: Reconstructed (EM) energy versus true energy (full) energy for the first cascade (left) and second cascade (right). The color scale is according to the PDF in each vertical true energy slice, with the solid and dashed lines showing the median $\pm 25\%$ quantiles. The bin entries are shown as numbers.

The spread around the median is also larger and starts to expand a lot above 200 GeV, where the statistics are lower as can be seen from the bin counts. It is also very apparent that the majority of energies of the second cascade are at lower true energy values between 1 GeV and 20 GeV.

For both cascade resolutions the effect of the reconstruction being biased towards lower values, due to the comparison of the full true energy to the reconstructed EM energy can be seen.

Length Resolutions

The decay length resolution is also investigated by looking at a similar style of 2-d histograms as for the energies, where the reconstructed decay length is plotted versus the true decay length. The left part of Figure 6.4 shows the distributions after the same selection criteria from Section 6.1.3 are applied. It can be observed that for short true lengths the reconstruction is over-estimating the length, while for long true lengths the reconstruction is strongly under-estimating the length. There is a region between true lengths of 20 m and 80 m where the median reconstruction is almost unbiased, but the 50 % interquartile range is large and increasing from ~ 50 m to ~ 70 m with true decay lengths.

The over-estimation at small true lengths can be explained for multiple reasons, one being that the shortest DOM spacing is ~ 7 m, vertically for DeepCore strings, but mostly larger than that, so resolving lengths below this is very complicated, and the reconstruction tends to be biased towards estimating the length around where the light was observed. Another reason is a similar argument to why the energies are over-estimated at small true values, namely that events that passed the selection and were reconstructed in those cases, probably have an over fluctuation in light deposition, extending further out from the vertices, so the reconstructed length is larger. Additionally, approaching a length of 0.0, the reconstructed length will of course always be a one-sided distribution, because the lengths have to be positive.

The under-estimation at large true lengths is more puzzling, and it seems like the distribution becomes bimodal in the reconstructed lengths, with

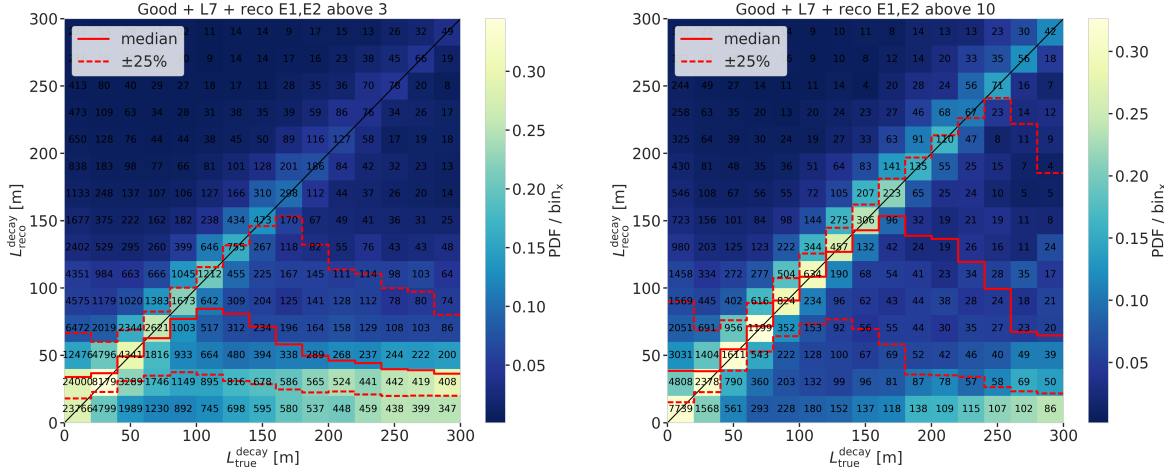


Figure 6.4: Reconstructed decay length versus true decay length for $\sim 3\text{ GeV}$ (left) and $\sim 10\text{ GeV}$ (right) minimum reconstructed cascade energies. The color scale is according to the PDF in each vertical true length slice, with the solid and dashed lines showing the median $\pm 25\%$ quantiles. The bin entries are shown as numbers.

one population around the diagonal, meaning that they are properly reconstructed, and one population at very short reconstructed lengths, which are badly reconstructed. Above 150 m the badly reconstructed population starts to dominate, and the median resolution drops off strongly. The assumption is that for these events, only one cascade was observed with enough light to be reconstructed, and the reconstruction describes the one observed cascade in two parts, separated by a short distance, driven by similar factors as mentioned before. A quick check to confirm whether this is the case, was to increase the selection criteria to minimum reconstructed cascade energies of 10 GeV, which is shown in the right part of Figure 6.4. It can be seen that the median resolution is already much better, aligning with the expectation between 40 m and 160 m. Judging from the median resolution and the $+25\%$ quantile in this range, there is very few events with an over-expectation in the energy, since both of them are alidgning with the diagonal. The spread towards lower reconstructed lengths, on the other hand, is still very large and above 200 m the badly reconstructed population starts to dominate again.

make on figure, where
the two selected regions
are highlighted? (RED)

fix caption (RED)

Badly Reconstructed Cascade Population

To investigate the badly reconstructed population further, a rough separation was made to find out what the cause of the difference is. It was already established that a larger reconstructed energy in both cascades, which is related to a larger true energy in form of more deposited light, leads to a better reconstruction in more events. As shown in Figure 6.5, only events with true decay length larger than 80 m are used, where the populations are split by the reconstructed decay length being larger or smaller than 80 m. Based on a few potential sourced of bad reconstruction, several variables were checked to see if there is a difference between the two populations.

The left part of Figure 6.6 shows the true horizontal distance of the second cascade from string 36. The distance is denoted as ρ_{36} and is a very good proxy for the distance to the center of the detector, because string 36 is almost at the center. While the distributions looks very similar for the first cascade

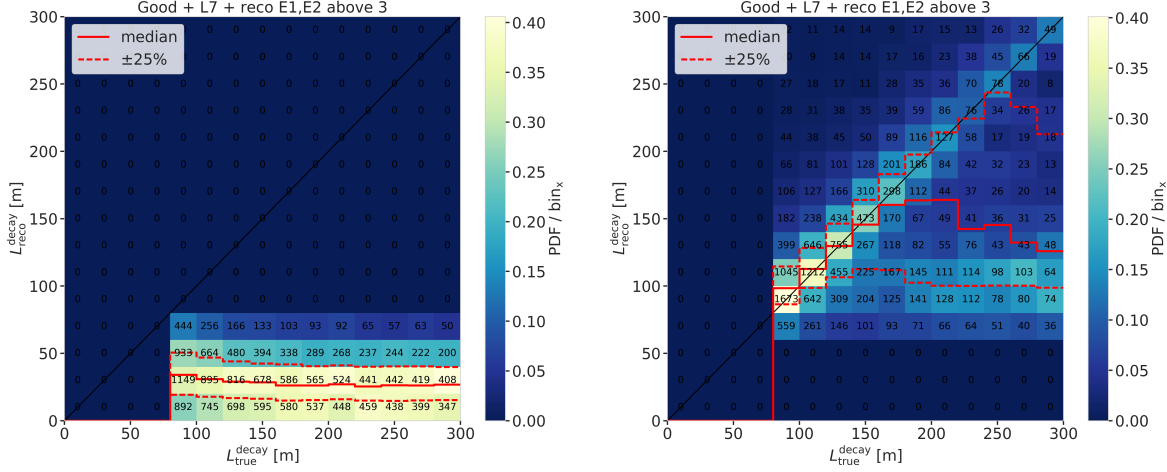


Figure 6.5

(not shown), for the second cascade the badly reconstructed population extends to larger values. Considering that the DeepCore strings are roughly inside a 70 m radius from the center, and the next layer of IceCube strings is at a radius of 125 m, this is a plausible explanation for a worse reconstruction, because for the badly reconstructed population the second cascades are more often in regions without DOMs, so less or no light is observed from them.

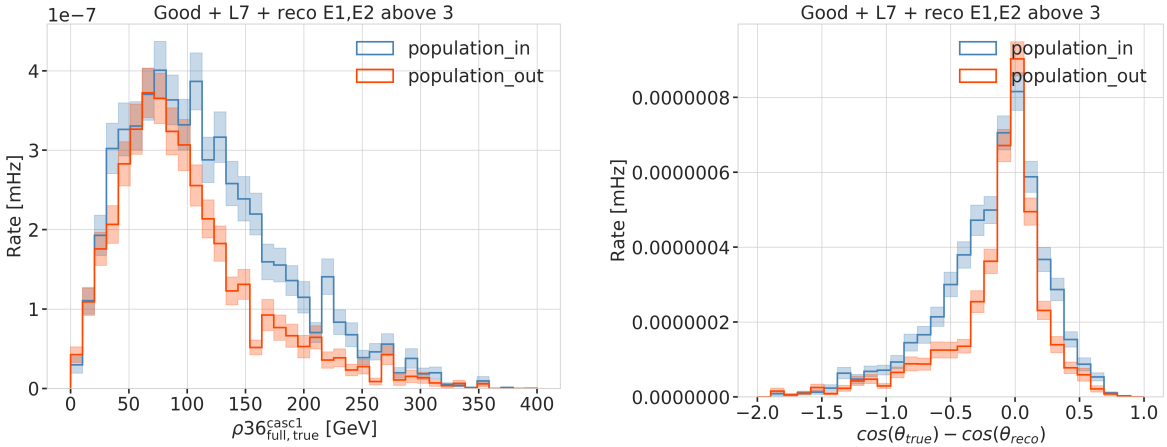


Figure 6.6

Another possible reason why the reconstruction underperforms could be that the initial seed direction was off and therefore one of the cascades cannot be found properly. Looking at the error of the cosine of the reconstructed zenith angle shown in the right of Figure 6.6, we see that the badly reconstructed population has a larger error, and is less peaked around 0.0. This could be a hint that the direction is worse for the badly reconstructed population, which could be due to a bad seed direction, or just the result of one cascade not being observed properly.

The true energies of both cascades are shown in Figure 6.5, where it can be observed that the first cascade energy is generally much larger than the second, peaking between 10 GeV and 20 GeV, while the second cascade peaks

re-make normalized?
(ORANGE)

fix caption (RED)

re-make normalized?
(ORANGE)

fix caption (RED)

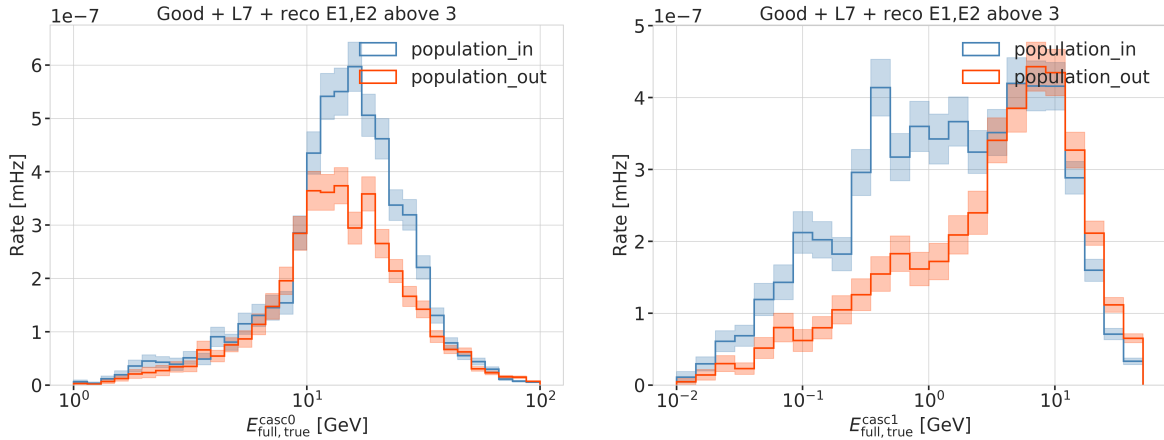


Figure 6.7

below 10 GeV. For the first cascade there is no significant difference between the two populations, but for the second cascade the badly reconstructed population has a larger fraction of events with lower energies and the distribution is almost uniform in the range of 2 GeV to 10 GeV, while the well reconstructed population has a peak around 10 GeV and falls off faster towards lower energies. This is a strong indication that the main reason for the bad reconstruction is the low energy of the second cascade.

Despite the fact that the split into the two populations was very rudimentary, it is clear that the main reason for the bad reconstruction is the low energy of the second cascade, while other factors, like the position of the second cascade, or the potentially bad input seed direction are also contributing to the bad reconstruction. For a more thorough investigation, a more sophisticated separation would be needed, but this is sufficient to conclude that the main reason for the bad reconstruction is the low energy of the second cascade.

circle back to the energy distributions I showed somewhere else, and state how the cascade energies are distributed in general (ORANGE)

6.2 Double Cascade Classification

Missing Points

- ▶ Briefly mention MuMillipede "reconstruction" (depending on how deep I want to go into the classifier I tested?)
- ▶ Calculated variables to input the classifier (distributions?) I guess some examples might do?
- ▶ Cuts applied to make sure the classifier is trained on well reconstructed events (energy, length, true, reco..)
- ▶ Tested classifier (BDT) versions and their performance
- ▶ takeaway? (not sure how to deal with the caveat of the weight being kind of wrong for these..)

6.3 Generic Double Cascade Performance

Ideas:

- ▶ why do these checks again with the model independent samples? (controllable parameter space and distributions, especially energy and length)
- ▶ benchmark some edge cases (e.g. "best case" of up-going string centered, purely horizontal, and realistic case)
- ▶ investigate where the reconstructions breaks down (in terms of cascade energies, which are the main factor as shown before)

6.3.1 Idealistic Performance

- ▶ for the perfect edge case of the event being directly on top of a DeepCore string with an up-going direction the length can be very well reconstructed above a true length of around 20 m
- ▶ 2-d histogram shows that up to a true decay length of ~ 210 m, there is no under-estimation of the length
- ▶ this means that the under-estimation observed before is only possible if there is no DOMs in between the two cascades
- ▶ this makes a lot of sense, since DOMs being present, but not observing any light is affecting the light expectation that goes into the reconstruction likelihood and therefore makes these hypotheses less likely and therefore incompatible with the data
- ▶ do I want more detailed plots here? I feel like this is enough..

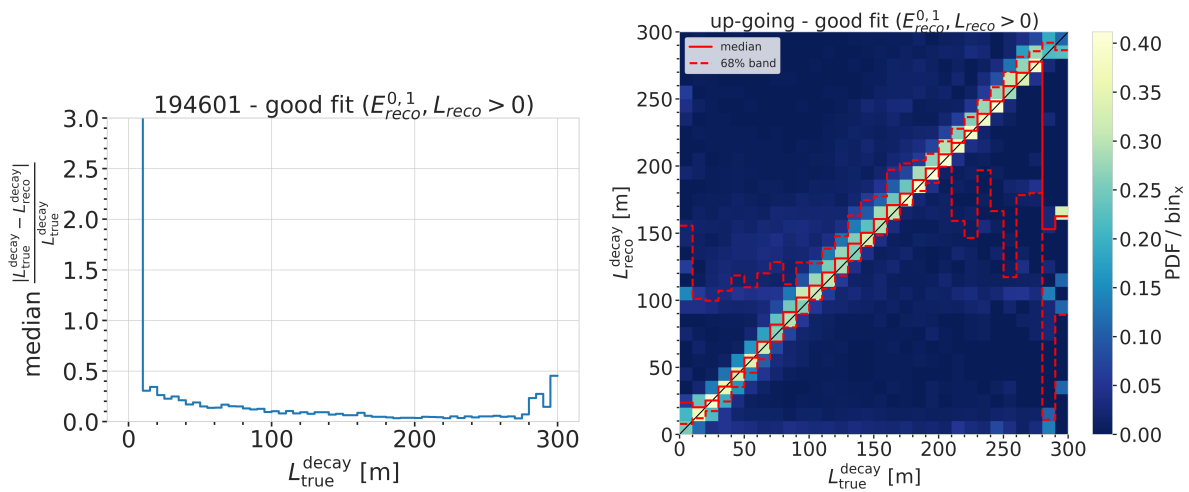


Figure 6.8

fix caption of this figure
(RED)

6.3.2 Realistic Performance

Energy/Decay Length Resolution

2-D Histograms

Things to mention about the 2d-hists:

- ▶ total energy resolution looks very good, above 10 GeV it's almost unbiased and the 1-sigma resolution band is below 20 %

describe the "good fit" selection when I first show plots that use it (ORANGE)

add some 1D resolution plots (ORANGE)

- ▶ individual cascade resolutions mirror this behavior, but are starting to stabilize in energy at lower energies around 5 GeV to 6 GeV with a broader resolution band of 50 %, but reducing drastically with increasing energy (down to 20 % at 100 GeV)
- ▶ interestingly, the second cascade energy reconstruction performs slightly worse, although they have the same energy ranges. This could hint at an asymmetry in the reconstruction process (might relate to how the two cascades are parameterized) or be due to the different positions and the dominantly up-going direction used in the sampling combined with the DOMs looking down (relate this to the sampling distributions explained/shown in the previous chapter)
- ▶ the decay length resolution looks much worse. In the region between 20 m and 80 m it's roughly unbiased, but 1-sigma resolution band is quite wide with a lot of outliers towards short reconstructed lengths. Below 20 m the reconstructed lengths are always over-estimating the true and above 80 m a population of events start to dominate where the decay lengths isn't getting reconstructed at all, which might indicate that one of the cascades wasn't observed. (Relate to the fact that this marginalizes over all energies, meaning also all events which have one cascade with very low energy are included here.)
- ▶ another interesting feature is the band of reconstructed lengths around 100 m, which is probably related to the spacing between most of the strings, which favors the reconstruction to be around this value, because that's the distance at which light can be observed, just from the fact that the DOMs are spaced at this distance (for low energetic cascades, this can dominate the reconstruction)

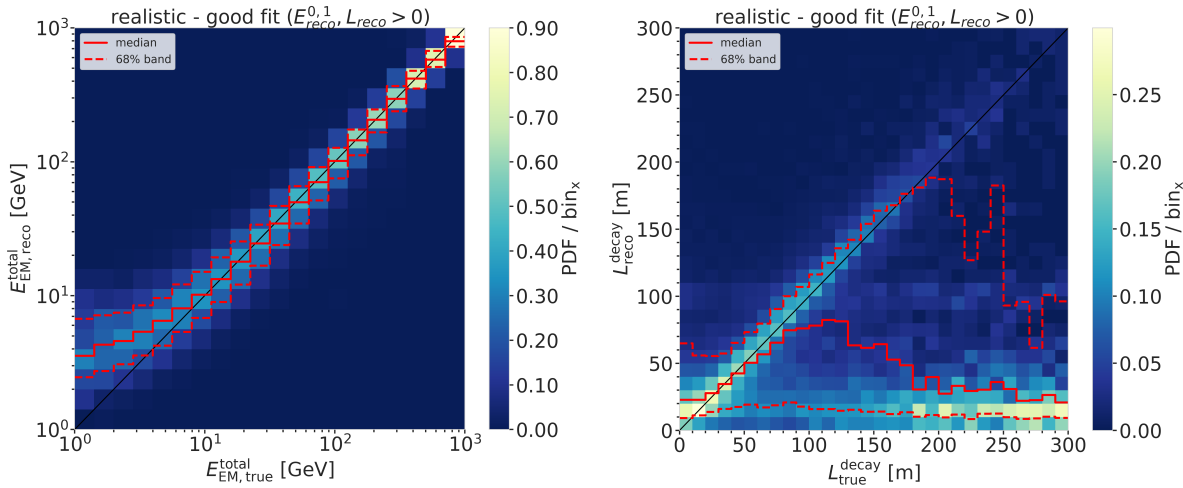


Figure 6.9
fix caption of this figure
(RED)

fix caption of this figure
(RED)

Energy Resolution Things to mention about the energy resolution:

- ▶ Here it can be seen more clearly how the median total energy resolution starts to stabilize around 0.0 at 10 GeV, while for lower energies the reconstruction is over-estimating the true energy. This is a known behavior of energy reconstructions in IceCube, which is mainly due to a selection effect. Only events with a certain amount of light can be reconstructed, which means that the ones with true small energies that are still in the sample are events with over average light production

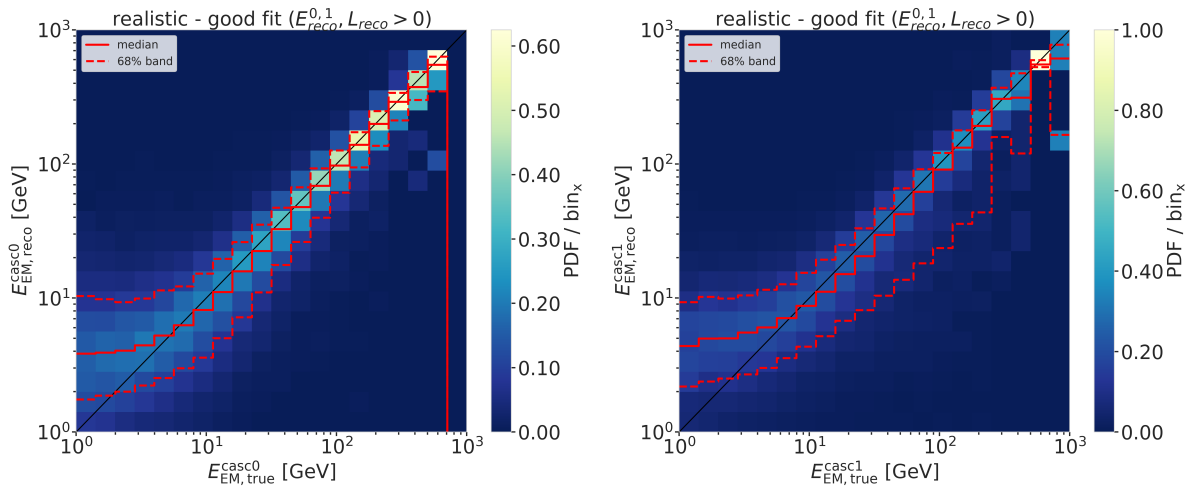


Figure 6.10

due to fluctuations or other effects?

fix caption of this figure
(RED)

Decay Length Resolution Things to mention about the decay length resolution:

- As already mentioned before, the decay length resolution is much worse than the energy resolutions. Figure 6.12 also shows that the median is below 0.0 for short true length and above 0.0 and approaching 1.0 for long true lengths.
- To investigate whether this is really due to the fact that one of the cascades is not observed, the decay length resolution was plotted against the total energy of the event and the minimum energy of the two cascades Figure 6.13.
- It can be seen that the median of the decay length resolution stabilizes at 0.0 for a total energy above 20 GeV, but the spread of the distribution is still quite large with a 1-sigma band of 80 % to 100 %.
- From the plot against the minimum energy it can be seen that the decay length resolution starts to be unbiased for a minimum energy of the cascades of 7 GeV, with an equivalently large spread.
- A preliminary takeaway from this is that the decay length reconstruction is not reliable at all for events with a total energy below 20 GeV or a minimum cascade energy below 7 GeV.

fix caption of this figure
(RED)

fix caption of this figure
(RED)

Make plot to show efficiency of the OscNext selection for HNL events.
(ORANGE)

Plot energy (true total) and true decay length across the different levels
(ORANGE)

Make table with the rates across the different levels for benchmark mass/mixing
(ORANGE)

6.3.3 Low Energy Event Selection Efficiency

Discussion ideas:

- Show energy, length distribution across the different levels?
- Show efficiency as table across the different levels (MC events + fraction?)
- Compare this to BG efficiency? (maybe rather for the discussion)
- At which level does the selection reduce the HNL the most?
- Is there a place to improve the HNL selection? (Might have to factor in the BG efficiency, as well..)

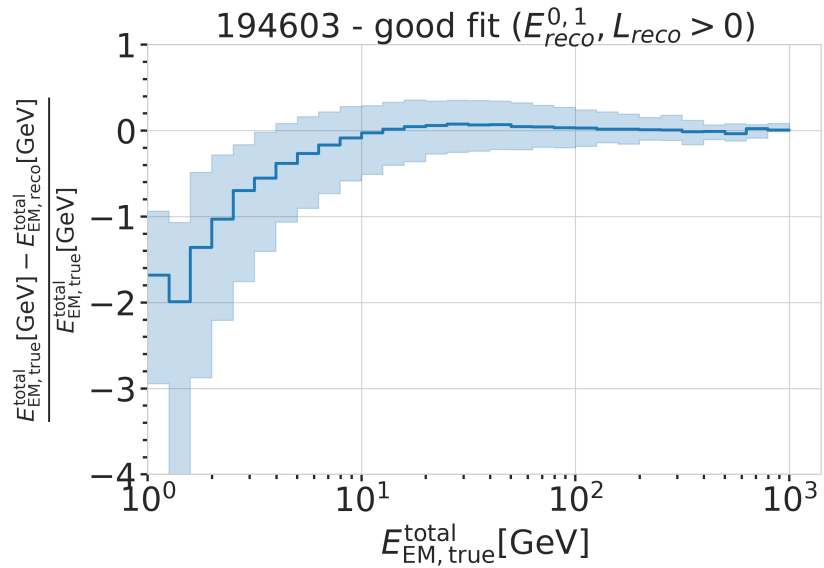


Figure 6.11

- What of this might change with Upgrade? (maybe rather for the discussion)

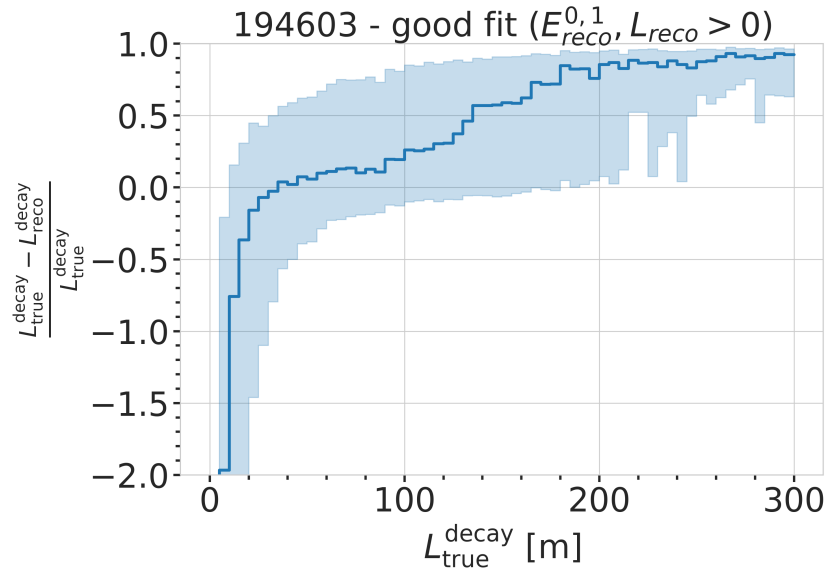


Figure 6.12

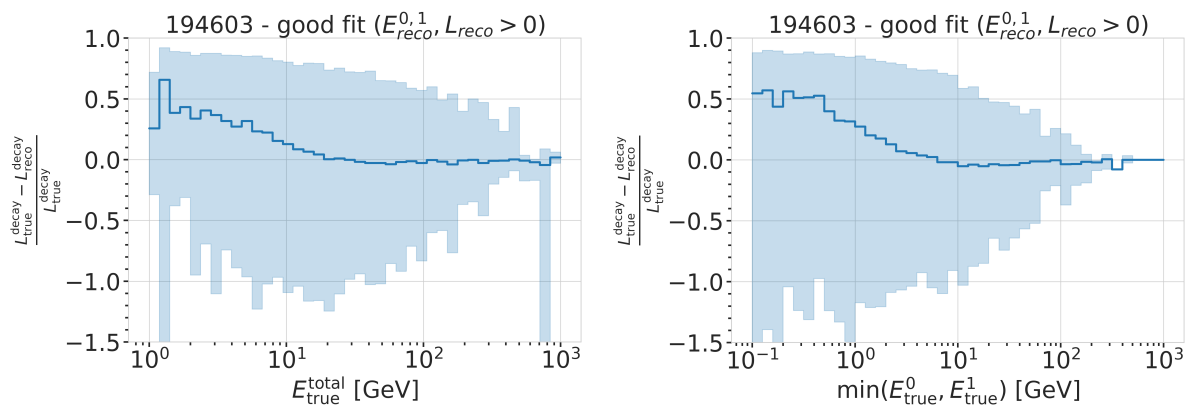


Figure 6.13

Search for Tau Neutrino Induced Heavy Neutral Lepton Events

7

This chapter describes the search for HNL events using 10 years of IceCube DeepCore data. The expected number of HNL events in the data sample depends on the mass of the additional heavy state, m_4 , and the mixing element $|U_{\alpha 4}^2|$, with $\alpha = e, \mu, \tau$, between the SM flavors and the new mass state. As discussed in Section ??, this work focuses on the mixing to the tau sector, $|U_{\tau 4}^2|$, which has the weakest constraints to date. Since the mass itself influences the production and decay kinematics of the event and the accessible decay modes, individual mass samples were produced as described in Section 4.2. The mass influences the decay length and energy distributions, while the mixing both changes the overall scale of the HNL events and the shape in energy and length. The search is performed for the three mass samples individually, while the mixing is the parameter that can be varied continuously and is measured in each fit.

7.1 Final Level Sample

The final level sample of this analysis consists of the neutrino and muon MC introduced in Section 5.1 and one of the three HNL samples explained in Section 4.2. All simulation and the 10 years of data are processed through the full processing and event selection chain described in Section 5.3 and Section 5.4 leading to the final level sample. As described in Section 5.4.2, event triggers consisting purely of random coincidences induced by noise in the DOMs have been reduced to a negligible rate, and will not be discussed further.

To get the neutrino expectation, the MC events are weighted according to their generation weight introduced in Section 5.1.1, multiplied by the total lifetime, and the expected neutrino flux. For the correct expectation at the detector, the events have to be weighted by the oscillation probability, depending on their energy and their traveled distance from the atmosphere. The oscillation probabilities are calculated using a PYTHON implementation of the calculations from [102], which use the matter profile of the Earth following the *Preliminary Reference Earth Model* (PREM) [103] as input. Apart from the energy and the distance, the two relevant parameters defining the oscillation probabilities are the atmospheric neutrino oscillation parameters θ_{23} and Δm_{31}^2 . Since the HNL events originate from the tau neutrinos produced in the atmosphere this weighting is also applied in addition to the specific weighting scheme for the HNL events described in Section 4.2.3, which is defined by the mixing $|U_{\tau 4}^2|$.

| | | |
|-----|----------------------|----|
| 7.1 | Final Level Sample | 67 |
| 7.2 | Statistical Analysis | 69 |
| 7.3 | Analysis Checks | 71 |
| 7.4 | Results | 73 |

[102]: Barger et al. (1980), “Matter effects on three-neutrino oscillations”

[103]: Dziewonski et al. (1981), “Preliminary reference Earth model”

7.1.1 Expected Rates/Events

The rates and the expected number of events for the SM background are shown in Table 7.1 with around 175000 total events expected in the 10 years. The explicit, good detector livetime in this data taking period is 9.28 years. The rates are calculated by summing the weights of all events in the final

level sample, while the uncertainties are calculated by taking the square root of the sum of the weights squared. The expected number of events is calculated by multiplying the rate with the livetime. The individual fractions show that this sample is neutrino dominated where the majority of events are ν_μ -CC events.

Table 7.1: Final level rates and event expectation of the SM background particle types.

| Type | Rate [mHz] | Events (in 9.28 years) | Fraction [%] |
|------------------------|------------|------------------------|--------------|
| ν_μ^{CC} | 0.3531 | 103321 ± 113 | 58.9 |
| ν_e^{CC} | 0.1418 | 41490 ± 69 | 23.7 |
| ν_{NC} | 0.0666 | 19491 ± 47 | 11.1 |
| ν_τ^{CC} | 0.0345 | 10094 ± 22 | 5.8 |
| μ | 0.0032 | 936 ± 15 | 0.5 |
| total | 0.5991 | 175336 ± 143 | 100.0 |

Should I adapt the total numbers to match the sum of the rounded individual parts? (YELLOW)

Table 7.2 shows the rates and expected number of events for the HNL signal simulation. The expectation depends on the mass and the mixing and shown here are two example mixings for all the three masses that are being tested in this work. A mixing of 0.0 would result in no HNL events at all. It can already be seen that for the smaller mixing of $|U_{\tau 4}|^2 = 10^{-3}$ the expected number of events is very low, while at the larger mixing of $|U_{\tau 4}|^2 = 10^{-1}$ the number is comparable to the amount of muons in the background sample.

Table 7.2: Final level rates and event expectations of the HNL signal for all three masses and two example mixing values.

| HNL mass | Rate [μHz] | Events (in 9.28 years) |
|----------------------------|-------------------------|------------------------|
| $ U_{\tau 4} ^2 = 10^{-1}$ | | |
| 0.3 GeV | 3.3298 ± 0.0053 | 974.5 ± 1.6 |
| 0.6 GeV | 3.0583 ± 0.0058 | 895.0 ± 1.7 |
| 1.0 GeV | 2.4988 ± 0.0059 | 731.3 ± 1.7 |
| $ U_{\tau 4} ^2 = 10^{-3}$ | | |
| 0.3 GeV | 0.0057 | 1.67 ± 0.01 |
| 0.6 GeV | 0.0220 | 6.44 ± 0.01 |
| 1.0 GeV | 0.0248 | 7.27 ± 0.01 |

7.1.2 Analysis Binning

An identical binning to the analysis performed in [84] is used. In total, there are three bins in PID (cascade-like, mixed, and track-like), 12 bins in reconstructed energy, and 8 bins in cosine of the reconstructed zenith angle as specified in Table 7.3. Extending the binning towards lower energies or increasing the number of bins in energy or cosine of the zenith angle did not improve the HNL sensitivities significantly, because the dominant signal region is already covered with a sufficiently fine binning to observe the shape and magnitude of the HNL events. This can be seen in the middle panel of Figure 7.1. To ensure that sufficient data events end up in the individual bins to result in a good fit, a few bins were not taken into account in the analysis that showed low data statistics. Those are shown in dark green in the three dimensional histogram.

[84]: Yu et al. (2023), “Recent neutrino oscillation result with the Ice-Cube experiment”

Table 7.3: Three dimensional binning used in the analysis. All variables are from the FLERCNN reconstruction explained in Section 5.4. remake without the top row of masked bins? add label to cbar and remove from title (RED)

| Variable | N _{bins} | Edges | Step |
|----------------|-------------------|--------------------------|-------------|
| P_v | 3 | [0.00, 0.25, 0.55, 1.00] | linear |
| E | 12 | [5.00, 100.00] | logarithmic |
| $\cos(\theta)$ | 8 | [-1.00, 0.04] | linear |

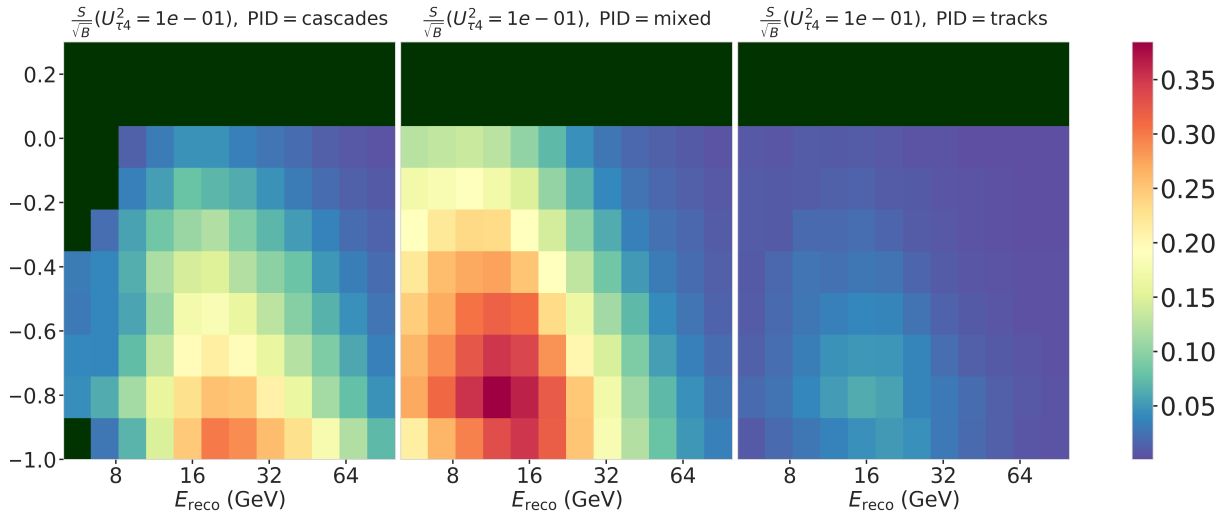


Figure 7.1

7.2 Statistical Analysis

7.2.1 Test Statistic

The measurements are performed by comparing the weighted MC to the data. Through variation of the nuisance and physics parameters that govern the weights, the best matching set of parameters can be found. The comparison is done using a modified χ^2 , defined as

$$\chi^2_{\text{mod}} = \sum_{i \in \text{bins}} \frac{(N_i^{\text{exp}} - N_i^{\text{obs}})^2}{N_i^{\text{exp}} + (\sigma_i^{\nu})^2 + (\sigma_i^{\mu})^2 + (\sigma_i^{\text{HNL}})^2} + \sum_{j \in \text{syst}} \frac{(s_j - \hat{s}_j)^2}{\sigma_{s_j}^2}, \quad (7.1)$$

as the fit metric. It is designed such that taking the difference between a free fit and a fit with fixed parameters based on a chosen hypothesis, $\Delta\chi^2_{\text{mod}}$, can be used as a *test statistic* (TS) for hypothesis testing. The total even expectation is $N_i^{\text{exp}} = N_i^{\nu} + N_i^{\mu} + N_i^{\text{HNL}}$, where N_i^{ν} , N_i^{μ} , and N_i^{HNL} are the expected number of events in bin i from neutrinos, atmospheric muons, and HNLs, while N_i^{obs} is the observed number of events in the bin. The expected number of events from each particle type is calculated by summing the weights of all events in the bin $N_i^{\text{type}} = \sum_i^{\text{type}} \omega_i$, with the statistical uncertainty being $(\sigma_i^{\text{type}})^2 = \sum_i^{\text{type}} \omega_i^2$. The additional term in Equation 7.1 is included to apply a penalty term for prior knowledge of the systematic uncertainties of the parameters where they are known. s_j are the systematic parameters that are varied in the fit, while \hat{s}_j are their nominal values and σ_{s_j} are the known uncertainties.

Do I want/need to include the description of the KDE muon estimation? (YELLOW)

7.2.2 Physics Parameters

The variable physics parameter in this analysis is the mixing between the HNL and the SM τ sector, $|U_{\tau 4}|^2$. It can be changed continuously in the range of $[0.0, 1.0]$ by applying the weighting scheme described in Section 4.2.3. The fit is initialized at an off-nominal value of 0.1. The other physics parameter, the mass m_4 of the HNL, is fixed to one of the three discrete masses to be

tested, by using the corresponding sample of the HNL simulation described in Section 4.2.

SB: generally you are missing a lot of references, and I don't think its very nice to read all these ranges and so on in the text. Surely you can just have a table with the systematics you include, their allowed range and prior if applicable? You can choose whether or not you want to discuss some parameters in more detail here, but it should be a discussion of the physics and impact on the analysis. e.g. you can include some plots showing how a change in some of the nuisance parameters changes the event counts in the analysis binning (RED)

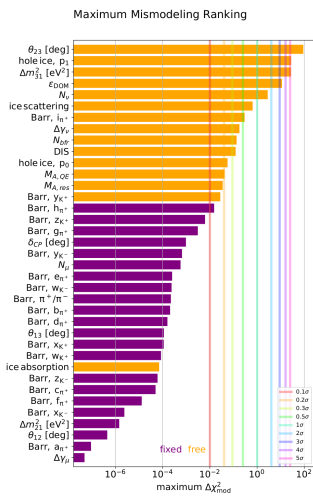


Figure 7.2: "calculated at a mixing of 0.1 and for the 1.0 GeV sample"

Blow up labels/legend/title and make it more readable in the margin or move it into the main text? (RED)

7.2.3 Nuisance Parameters

To decide which systematic uncertainties should be included in the fit, we test the potential impact they have on the TS if they are neglected. The test is performed by creating Asimov data using the BG simulation and the HNL simulation of the 1.0 GeV mass sample at a mixing value of 0.1, which is chosen as a benchmark physics parameter and does not have a significant impact on the test. The systematic parameter of interest is set to a value above its nominal expectation, either pulled up by $+1\sigma$ or by an educated estimate for parameters without a well-defined uncertainty. A fit is performed fixing the systematic parameter of interest and leaving all additional parameters free. The resulting TS is the mis-modeling significance between this fit and a fit with all parameters free, which would result in a TS of 0.0 for this Asimov test. Parameters below a significance of 0.1σ are fixed, and the test is performed in an iterative manner until the final set of free parameters is found.

Figure 7.2 shows the resulting significances of one of these tests. The parameters tested are the systematic parameters introduced in Section 5.5 and the atmospheric oscillation parameters mentioned in Section 7.1. In the final selection of free parameters the Barr. h_{π^+} parameter was also left free and the ice absorption is still kept free, despite showing a small significance. This is done because the bulk ice parameters are not well constrained and are known to have a large impact, which might be concealed in the test, due to correlations with the other parameters. In this test, the effect of correlations is challenging to consider, because only the impact of one parameter is tested at a time, using the overall mis-modeling significance as a measure. The mis-modeling could be reduced by a correlated parameter capturing the effect of the parameter of interest. For this reason a very conservative threshold of 0.1σ is chosen and some parameters below the threshold are still left free in the fit.

All nuisance parameters that are left free in the fit are summarized in Table 7.4, showing their nominal values, the allowed fit ranges, and their Gaussian prior, if applicable. The scaling parameter N_v is included to account for the overall normalization of the neutrino rate, and it has the identical effect on the SM neutrino events and the BSM HNL events, because they both originate from the same neutrino flux. Despite being known to $\sim 5\%$ in this energy range, there is no prior applied to this parameter, because the fit itself is able to constrain it well, which can be seen by the large impact it shows in Figure 7.2. Concerning the atmospheric neutrino flux, the CR power law flux correction factor $\Delta\gamma_v$ introduced in Section 5.5.1 is included with nominal value of 0.0 which corresponds to a CR power law of E^{-2} . A slightly conservative prior of 0.1 is applied to the parameter, while latest measurements show an uncertainty of 0.05 [90].

All the detector systematic uncertainties are included in the fit. The DOM efficiency ϵ_{DOM} is constrained by a Gaussian prior with a width of 0.1, which is a conservative estimate based on the studies of the optical efficiency using minimum ionizing muons from [41, 42].

| Parameter | Nominal | Range | Prior |
|---------------------------------|-----------|----------------|-------|
| $\theta_{23}[\circ]$ | 47.5047 | [0.0, 90.0] | - |
| $\Delta m_{31}^2 [\text{eV}^2]$ | 0.002475 | [0.001, 0.004] | - |
| N_ν | 1.0 | [0.1, 2.0] | - |
| $\Delta\gamma_\nu$ | 0.0 | [-0.5, 0.5] | 0.1 |
| Barr h_{π^+} | 0.0 | [-0.75, 0.75] | 0.15 |
| Barr i_{π^+} | 0.0 | [-3.05, 3.05] | 0.61 |
| Barr y_{K^+} | 0.0 | [-1.5, 1.5] | 0.3 |
| DIS | 0.0 | [-0.5, 1.5] | 1.0 |
| $M_{A,\text{QE}}$ | 0.0 | [-2.0, 2.0] | 1.0 |
| $M_{A,\text{res}}$ | 0.0 | [-2.0, 2.0] | 1.0 |
| ϵ_{DOM} | 1.0 | [0.8, 1.2] | 0.1 |
| hole ice p_0 | 0.101569 | [-0.6, 0.5] | - |
| hole ice p_1 | -0.049344 | [-0.2, 0.2] | - |
| bulk ice absorption | 1.0 | [0.85, 1.15] | - |
| bulk ice scattering | 1.05 | [0.9, 1.2] | - |
| N_{bfr} | 0.0 | [-0.2, 1.2] | - |

The two atmospheric neutrino oscillation parameters θ_{23} and Δm_{31}^2 are also included in the fit with nominal values of 47.5047° and $2.475 \times 10^{-3} \text{ eV}^2$, respectively. Since they govern the shape and the strength of the tau neutrino flux, by defining the oscillation from ν_μ to ν_τ , they are also relevant for the HNL signal shape.

Table 7.4: Systematic uncertainty parameters that are left free to float in the fit. Their allowed fit ranges are shown with the nominal value and the Gaussian prior width if applicable.

7.2.4 Treatment of Detector Response Uncertainties via a Likelihood-Free Inference Method

[104]

7.2.5 Low Energy Analysis Framework

The analysis is performed using the PISA [105] [106] software framework, which was developed to perform analyses "of small signals in high-statistics neutrino oscillation experiments". It is used to generate the expected event distributions from several MC samples, which can then be compared to the observed data. The expectation for each sample is calculated in parallel, applying physics and nuisance parameter effects in a stage-wise manner, before combining the final expectation from all the samples.

7.3 Analysis Checks

Fitting to data is performed in a *blind* manner, where the analyzer does not immediately see the fitted physics and nuisance parameter values, but first checks that a set of pre-defined *goodness of fit* (GOF) criteria are fulfilled. This is done to circumvent the so-called *confirmation bias* [107], where the analyzer might be tempted to construct the analysis in a way that confirms their expectation. After the GOF criteria are met to satisfaction, the fit results are unblinded and the full result can be revealed. Before these blind fits to data are performed, the robustness of the analysis method is tested using pseudo-data that is generated from the MC.

elaborate why this is also done to cover the whole energy range for the Pion production, referencing the Barr Block plot that I haven't included yet :D (RED)

Need cite here! (RED)

[90]: Evans et al. (2017), "Uncertainties in atmospheric muon-neutrino fluxes arising from cosmic-ray primaries"

[41]: Feintzeig (2014), "Searches for Point-like Sources of Astrophysical Neutrinos with the IceCube Neutrino Observatory"

[42]: Kulacz (2019), "In Situ Measurement of the IceCube DOM Efficiency Factor Using Atmospheric Minimum Ionizing Muons"

I should add some final level effects of some systematics on the 3D binning and maybe discuss how they are different from the signal shape, or so? (ORANGE)

I still need to write this section... (RED)

[104]: Fischer et al. (2023), "Treating detector systematics via a likelihood free inference method"

[105]: Aartsen et al. (2020), "Computational techniques for the analysis of small signals in high-statistics neutrino oscillation experiments"

Do I want more information about the different pipelines and stages? Could link back to the extra stage I wrote and add the earth model and oscillation calculation information here, I guess?! (ORANGE)

[107]: Nickerson (1998), "Confirmation Bias: A Ubiquitous Phenomenon in Many Guises"

1: There is a degeneracy between the lower octant ($\theta_{23} < 45^\circ$) and the upper octant ($\theta_{23} > 45^\circ$), which can lead to fit metric minima (local and global) at two positions that are mirrored around 45° in θ_{23} .

[108]: Dembinski et al. (2022), *scikit-hep/minuit*: v2.17.0

[109]: James et al. (1975), "Minuit: A System for Function Minimization and Analysis of the Parameter Errors and Correlations"

| Fit | Err. | Prec. | Tol. |
|--------|------|-------|------|
| Coarse | 1e-1 | 1e-8 | 1e-1 |
| Fine | 1e-5 | 1e-14 | 1e-5 |

Table 7.5: Migrad settings for the two stages in the minimization routine. *Err.* are the step size for the numerical gradient estimation, *Prec.* is the precision with which the LLH is calculated, and *Tol.* is the tolerance for the minimization.

2: A pseudo-data set without statistical fluctuations is called Asimov data set.

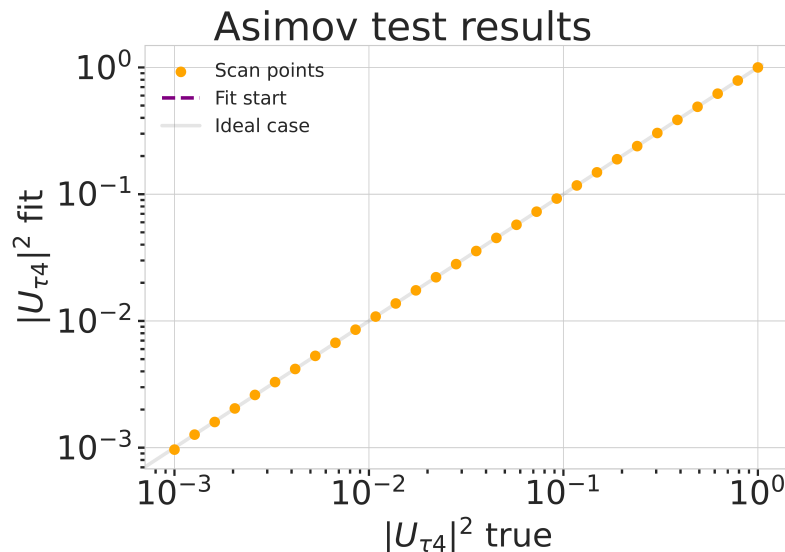
Figure 7.3: Asimov inject/recover test for the 0.6 GeV mass sample. Mixes in one plot and adjust the text to it! Remove fit start from legend (RED).

Mention that the mis-modeling (what it is) is at the order of 1e-07 for all of them (check again) and refer to the deviations in the mixing to be not relevant because of that! (RED)

7.3.1 Minimization Robustness

To find the set of parameters that best describes the data, a staged minimization routine is used. In the first stage, a fit with coarse minimizer settings is performed to find a rough estimate of the *best fit point* (BFP). In the second stage, the fit is performed again in both octants¹ of θ_{23} , starting from the BFP of the coarse fit. For each individual fit the *MIGRAD* routine of *iminuit* [108] is used to minimize the χ^2_{mod} fit metric defined in Equation 7.1. *Iminuit* is a fast, python compatible minimizer based on the *MINUIT2 C++ library* [109]. The individual minimizer settings for both stages are shown in Table 7.5.

To test the minimization routine and to make sure it consistently recovers any physics parameters, pseudo-data sets are produced from the MC by choosing the nominal nuisance parameters and specific physics parameters, without adding any statistical or systematic fluctuations to it. These so-called *Asimov*² data sets are then fit back with the full analysis chain. This type of test is called *Asimov inject/recover test*. A set of mixing values between 10^{-3} and 10^0 is injected and fit back. Without fluctuations the fit is expected to always recover the injected parameters (both physics and nuisance parameters). The fitted mixing values from the Asimov inject/recover tests are compared to the true injected values in Figure 7.3 for the 0.6 GeV sample. As expected, the fit is always able to recover the injected physics parameter and the nuisance parameters.



7.3.2 Goodness of Fit

To estimate the GOF, pseudo-data is generated from the MC by injecting the BFP parameters as true parameters and then fluctuating the expected bin counts to account for MC uncertainty and Poisson fluctuations in data. First, the expectation value of each bin is drawn from a Gaussian distribution centered at the nominal expectation value with a standard deviation corresponding to the MC uncertainty of the bin. Based on this sampled expectation value, each bin count is drawn from a Poisson distribution, independently, to get the final pseudo-data set. These pseudo-data sets are then fit back with the analysis chain. By comparing the distribution of fit

metric values from this *ensemble* of pseudo-data trials to the fit metric of the fit to real data, a p-value can be calculated. The p-value is the probability of finding a value at least as large as the one from the data fit. Figure 7.4 shows the distribution from the ensemble tests for the 0.6 GeV mass sample and the observed value from the fit, resulting in a p-value of 28.5 %. The p-values for the 0.3 GeV and 1.0 GeV are 28.3 % and 26.0 %, respectively, and the corresponding plots are shown in Section ???. Based on this test, it is concluded that the fit result is compatible with the expectation from the ensemble of pseudo-data trials.

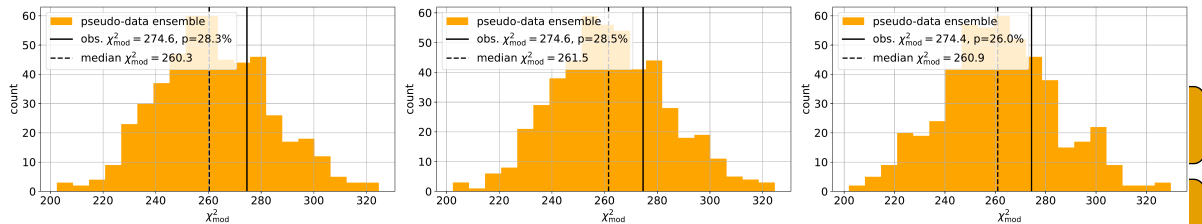


Figure 7.4: Observed fit metric and fit metric distribution from pseudo-data trials for the 0.6 GeV mass sample.

7.3.3 Data/MC Agreement

At the BFP, the agreement between the data and simulation is probed by comparing the 1-dimensional analysis distributions for PID, energy, and cosine of the zenith angle. As an example, two distributions for the 0.6 GeV mass sample are shown in Figure ???. The data is compared to the total MC expectation, which is also split up into its composing parts. Good agreement can be observed in the pull distributions and is quantified by a reduced χ^2 , which is close to 1.0 for all distributions. The reduced χ^2 for all investigated distributions is listed in Table ???, while the distributions themselves can be found in Section ???.

7.4 Results

7.4.1 Best Fit Nuisance Parameters

The resulting nuisance parameter values from the fits are illustrated in Figure 7.5, where the differences to the nominal values are shown, normalized by the distance to the closest boundary. The results from all three fits are shown in the same plot and the fits prefer values of the same size for all three mass samples. For parameters that had a Gaussian prior, the 1σ range is also displayed. As was already confirmed during the blind fit procedure, all fitted parameters are within this range. The effective ice model parameter, N_{bfr} , prefers a value of ~ 0.74 , indicating that the data fits better to an ice model that includes real birefringence effects during photon propagation. For completeness's sake, the explicit results are listed in Table B.1. There, the nominal values and the absolute differences to the best fit value are also presented.

Add 3D BFP-data pull distribution for one mass (they look the same, no?) (RED)

once I have them (RED)

add 1-d data/mc agreement for example mass sample (0.6?) and all 3 analysis variables (RED)

add table with reduced chi2 for all 1-d distributions (RED)

Cite (again)! (RED)

Compare here the best fit oscillation parameters to the FLERCNN results and try to quantify it, stating the pitfalls of the comparitions (statistically fully dependent) (RED)

Plot updates: change 0.6 GeV color, sort variables by type (same as table), offset markers left/right, change grid lines to separate the parameter region, ylabel limit instead of range (RED)

Show best fit hole ice angular acceptance compared to nominal and flasher/in-situ fits, maybe? (YELLOW)

Discuss what it means that the parameters are at these values? Here, or somewhere else? (RED)

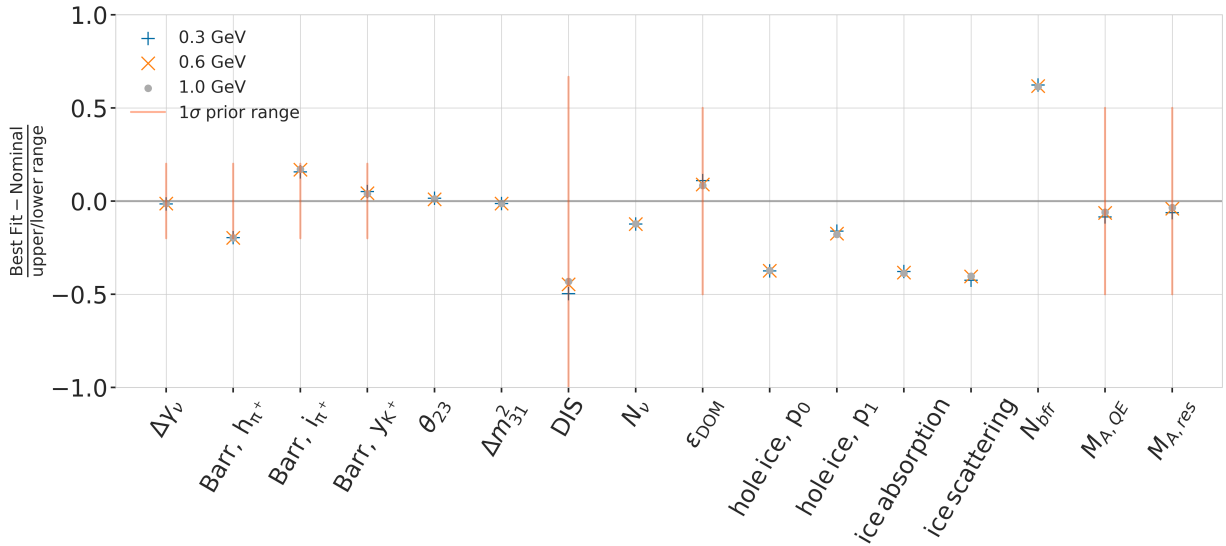


Figure 7.5: Best fit nuisance parameter distances to the nominal values, normalized by the distance to the closest boundary. For parameters with a Gaussian prior, the $+1\sigma$ range is also shown.

7.4.2 Best Fit Parameters and Limits

The fitted mixing values are

$$\begin{aligned}|U_{\tau 4}|^2(0.3 \text{ GeV}) &= 0.003^{+0.084}, \\|U_{\tau 4}|^2(0.6 \text{ GeV}) &= 0.080^{+0.134}, \text{ and} \\|U_{\tau 4}|^2(1.0 \text{ GeV}) &= 0.106^{+0.132},\end{aligned}$$

with their $+1\sigma$ uncertainty. All of them are compatible with the null hypothesis of 0.0 mixing, although the 0.6 GeV and 1.0 GeV fits indicate a mixing value of 0.08 and 0.106, respectively. The best fit mixing values and the corresponding upper limits at 68 % and 90 % confidence level (CL) are listed in Table 7.6, also showing the p -value to reject the null hypothesis. The CLs and p -value are estimated by assuming that Wilks' theorem [110] holds, meaning that the TS follows a χ^2 distribution with one degree of freedom.

[110]: Wilks (1938), "The Large-Sample Distribution of the Likelihood Ratio for Testing Composite Hypotheses,"

| HNL mass | $ U_{\tau 4} ^2$ | 68 % CL | 90 % CL | NH p -value |
|----------|------------------|---------|---------|---------------|
| 0.3 GeV | 0.003 | 0.087 | 0.194 | 0.97 |
| 0.6 GeV | 0.080 | 0.214 | 0.355 | 0.79 |
| 1.0 GeV | 0.106 | 0.238 | 0.396 | 0.63 |

fix table caption (RED)

Figure 7.6 shows the observed TS profiles as a function of $|U_{\tau 4}|^2$ for all three fits. The TS profile is the difference in χ^2_{mod} between the free fit and a fit where the mixing is fixed to a specific value. Also shown is the expected TS profile, based on 100 pseudo-data trials, produced at the BFP and then fluctuated using both Poisson and Gaussian fluctuations, to include the data and the MC uncertainty as was explained in Section 7.3.2. The median expectation and the 68 % and 90 % bands are shown and the observed TS profiles lie within the 68 % band for all three, confirming that they are compatible with data fluctuations. For the 0.3 GeV fit, the observed contour is slightly left of the median expectation, meaning that the observed upper limits in $|U_{\tau 4}|^2$ are slightly stronger than expected. For the 0.6 GeV the opposite is the case and the observed upper limit is therefore slightly weaker than expected. For the 1.0 GeV fit, the observed upper limit is very close to the median expectation

in the region where the 68 % and 90 % CLs thresholds are crossed. The observed upper limits are also shown in Table 7.6.

add horizontal CL lines?

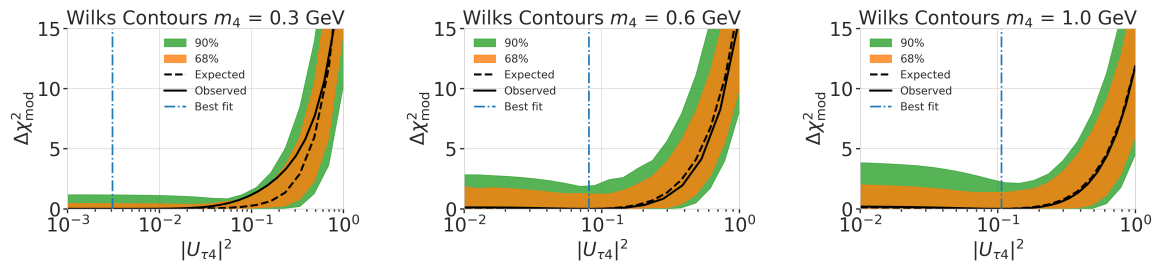


Figure 7.6: xx

fix caption for this figure (RED)

make plot with BFPs and limit, comparing to upper limits from other experiments, think about how to present it (RED)

8

Summary and Discussion

what was done?

1. set up model dependent and independent signal simulation for low energy double cascade events from HNL produciton and decay inside IceCube DeepCore
2. estimate performance of reconstructing and identifying these events
3. search for (cascade-like) events in 10 years of icecube deepcore data

| | | |
|-----|--|----|
| 8.1 | Performance to Detecting Low Energetic Double Cascades | 77 |
| 8.2 | Search for Heavy Neutral Lepton Production and Decay | 77 |
| 8.3 | Outlook | 77 |

8.1 Performance to Detecting Low Energetic Double Cascades

8.2 Search for Heavy Neutral Lepton Production and Decay

8.2.1 Agreement with Standard Model Three-Flavor Oscillation Measurement

8.3 Outlook

8.3.1 Shape Analysis Improvements

- ▶ estimate full contribution from cascade only events (underestimated due to limited sampling distributions)
- ▶ include double cascade classifier into Binning
- ▶ further optimize binning

8.3.2 Test Coupling to Electron/Muon Flavor

8.3.3 Test Additional Coupling Processes

8.3.4 IceCube Upgrade

Conclusion

9

Write conclusion (RED)

APPENDIX

A

Heavy Neutral Lepton Signal Simulation

A.1 Model Independent Simulation Distributions

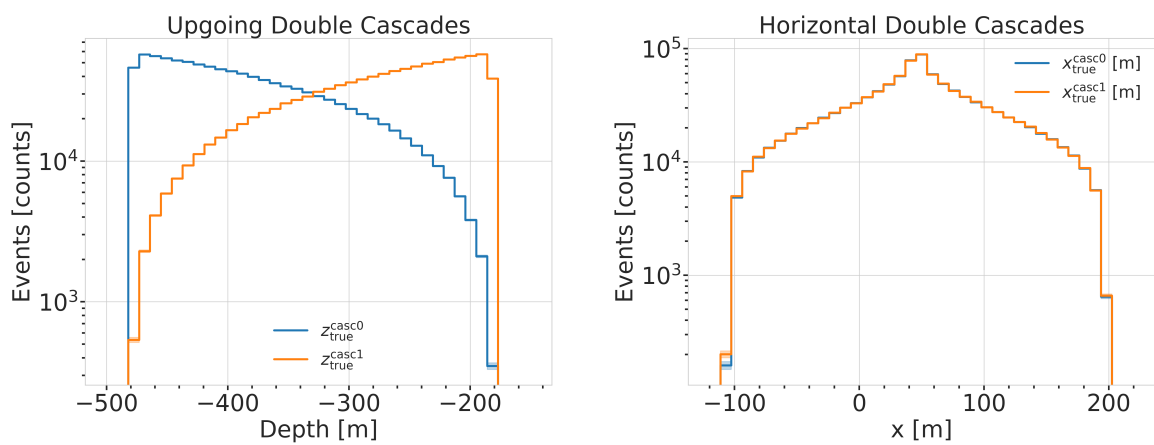


Figure A.1: Generation level distributions of the simplistic simulation sets. Vertical positions (left) and horizontal positions (right) of both sets are shown.

- Re-make plot with x, y for horizontal set one plot!
- Re-make plot with x, y, z for both cascades in one.
- Re-arrange plots in a more sensible way.

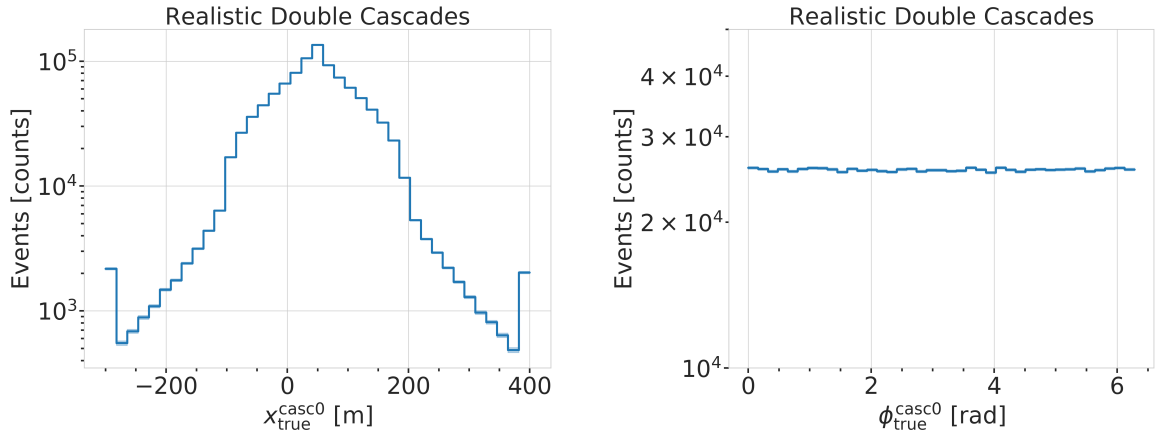


Figure A.2: Generation level distributions of the realistic simulation set. Shown are the cascade x, y, z positions (left) and direction angles (right).

A.2 Model Dependent Simulation Distributions

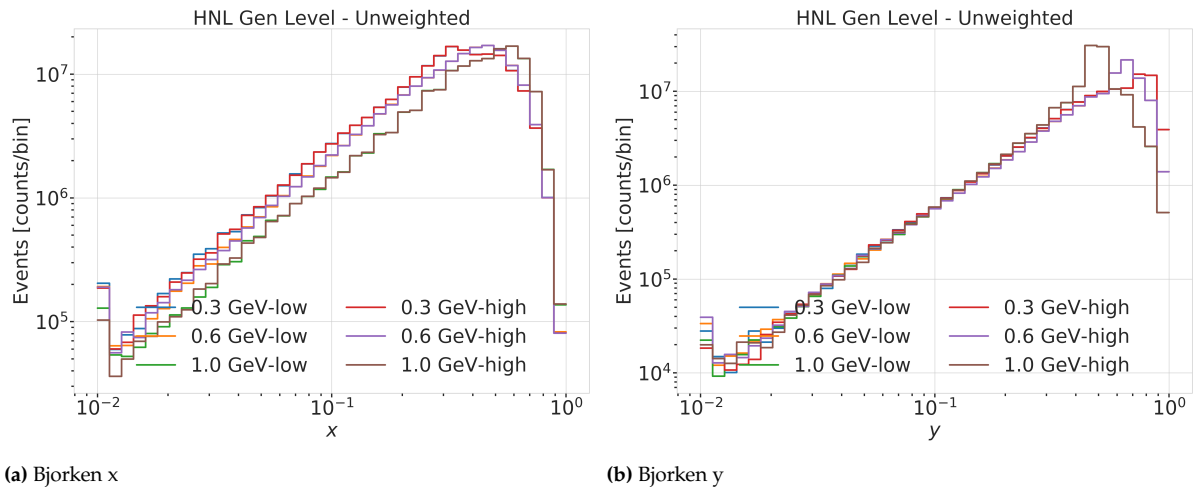


Figure A.3: Generation level distributions of the model dependent simulation.

B

Analysis Results

B.1 Best Fit Nuisance Parameters

Table B.1: xx

| Parameter | Nominal | Best Fit | | | Nominal - Best Fit | | |
|---------------------------------|-----------|-----------|-----------|-----------|--------------------|-----------|-----------|
| | | 0.3 GeV | 0.6 GeV | 1.0 GeV | 0.3 GeV | 0.6 GeV | 1.0 GeV |
| $ U_{\tau 4} ^2$ | - | 0.003019 | 0.080494 | 0.106141 | - | - | - |
| $\theta_{23} [\circ]$ | 47.504700 | 48.117185 | 47.918758 | 48.010986 | -0.612485 | -0.414058 | -0.506286 |
| $\Delta m_{31}^2 [\text{eV}^2]$ | 0.002475 | 0.002454 | 0.002454 | 0.002455 | 0.000020 | 0.000021 | 0.000019 |
| N_ν | 1.000000 | 0.889149 | 0.889055 | 0.889559 | 0.110851 | 0.110945 | 0.110441 |
| $\Delta \gamma_\nu$ | 0.000000 | -0.007926 | -0.006692 | -0.006596 | 0.007926 | 0.006692 | 0.006596 |
| Barr h_{π^+} | 0.000000 | -0.147475 | -0.148481 | -0.148059 | 0.147475 | 0.148481 | 0.148059 |
| Barr i_{π^+} | 0.000000 | 0.475448 | 0.513393 | 0.521626 | -0.475448 | -0.513393 | -0.521626 |
| Barr y_{K^+} | 0.000000 | 0.076176 | 0.062893 | 0.057548 | -0.076176 | -0.062893 | -0.057548 |
| DIS | 0.000000 | -0.248709 | -0.223302 | -0.215666 | 0.248709 | 0.223302 | 0.215666 |
| $M_{A,\text{QE}}$ | 0.000000 | -0.170528 | -0.128150 | -0.120345 | 0.170528 | 0.128150 | 0.120345 |
| $M_{A,\text{res}}$ | 0.000000 | -0.125855 | -0.080875 | -0.070716 | 0.125855 | 0.080875 | 0.070716 |
| ϵ_{DOM} | 1.000000 | 1.021984 | 1.017789 | 1.016689 | -0.021984 | -0.017789 | -0.016689 |
| hole ice p_0 | 0.101569 | -0.161341 | -0.161051 | -0.160129 | 0.262910 | 0.262620 | 0.261698 |
| hole ice p_1 | -0.049344 | -0.073701 | -0.075596 | -0.076261 | 0.024357 | 0.026252 | 0.026917 |
| ice absorption | 1.000000 | 0.943261 | 0.942463 | 0.942000 | 0.056739 | 0.057537 | 0.058000 |
| ice scattering | 1.050000 | 0.986152 | 0.989289 | 0.989438 | 0.063848 | 0.060711 | 0.060562 |
| N_{bfr} | 0.000000 | 0.746684 | 0.740255 | 0.736215 | -0.746684 | -0.740255 | -0.736215 |

fix caption and design +
significant digits to show
(ORANGE)

maybe show range/prior
and then deviation in
sigma, or absolute for the
ones without prior

Bibliography

Here are the references in citation order.

- [1] W. Pauli. "Dear radioactive ladies and gentlemen". In: *Phys. Today* 31N9 (1978), p. 27 (cited on page 1).
- [2] C. L. Cowan et al. "Detection of the Free Neutrino: a Confirmation". In: *Science* 124.3212 (1956), pp. 103–104. doi: [10.1126/science.124.3212.103](https://doi.org/10.1126/science.124.3212.103) (cited on page 1).
- [3] G. Danby et al. "Observation of High-Energy Neutrino Reactions and the Existence of Two Kinds of Neutrinos". In: *Phys. Rev. Lett.* 9 (1 July 1962), pp. 36–44. doi: [10.1103/PhysRevLett.9.36](https://doi.org/10.1103/PhysRevLett.9.36) (cited on page 1).
- [4] K. Kodama et al. "Observation of tau neutrino interactions". In: *Physics Letters B* 504.3 (2001), pp. 218–224. doi: [https://doi.org/10.1016/S0370-2693\(01\)00307-0](https://doi.org/10.1016/S0370-2693(01)00307-0) (cited on page 1).
- [5] R. Davis, D. S. Harmer, and K. C. Hoffman. "Search for Neutrinos from the Sun". In: *Phys. Rev. Lett.* 20 (21 May 1968), pp. 1205–1209. doi: [10.1103/PhysRevLett.20.1205](https://doi.org/10.1103/PhysRevLett.20.1205) (cited on pages 1, 6).
- [6] M. G. Aartsen et al. "The IceCube Neutrino Observatory: instrumentation and online systems". In: *Journal of Instrumentation* 12.3 (Mar. 2017), P03012. doi: [10.1088/1748-0221/12/03/P03012](https://doi.org/10.1088/1748-0221/12/03/P03012) (cited on pages 1, 19, 21, 42).
- [7] C. N. Yang and R. L. Mills. "Conservation of Isotopic Spin and Isotopic Gauge Invariance". In: *Physical Review* 96.1 (Oct. 1954), pp. 191–195. doi: [10.1103/PhysRev.96.191](https://doi.org/10.1103/PhysRev.96.191) (cited on page 3).
- [8] S. Weinberg. "A Model of Leptons". In: *Phys. Rev. Lett.* 19 (21 Nov. 1967), pp. 1264–1266. doi: [10.1103/PhysRevLett.19.1264](https://doi.org/10.1103/PhysRevLett.19.1264) (cited on page 3).
- [9] S. L. Glashow. "Partial-symmetries of weak interactions". In: *Nuclear Physics* 22.4 (Feb. 1961), pp. 579–588. doi: [10.1016/0029-5582\(61\)90469-2](https://doi.org/10.1016/0029-5582(61)90469-2) (cited on page 3).
- [10] R. Jackiw. "Physical Formulations: Elementary Particle Theory. Relativistic Groups and Analyticity. Proceedings of the eighth Nobel Symposium, Aspenäsgården, Lerum, Sweden, May 1968. Nils Svartholm, Ed. Interscience (Wiley), New York, and Almqvist and Wiksell, Stockholm, 1969. 400 pp., illus. \$31.75." In: *Science* 168.3936 (1970), pp. 1196–1197. doi: [10.1126/science.168.3936.1196.b](https://doi.org/10.1126/science.168.3936.1196.b) (cited on page 3).
- [11] P. Higgs. "Broken symmetries, massless particles and gauge fields". In: *Physics Letters* 12.2 (1964), pp. 132–133. doi: [https://doi.org/10.1016/0031-9163\(64\)91136-9](https://doi.org/10.1016/0031-9163(64)91136-9) (cited on page 3).
- [12] S. Chatrchyan et al. "Observation of a New Boson at a Mass of 125 GeV with the CMS Experiment at the LHC". In: *Phys. Lett. B* 716 (2012), pp. 30–61. doi: [10.1016/j.physletb.2012.08.021](https://doi.org/10.1016/j.physletb.2012.08.021) (cited on page 3).
- [13] G. Aad et al. "Observation of a new particle in the search for the Standard Model Higgs boson with the ATLAS detector at the LHC". In: *Phys. Lett. B* 716 (2012), pp. 1–29. doi: [10.1016/j.physletb.2012.08.020](https://doi.org/10.1016/j.physletb.2012.08.020) (cited on page 3).
- [14] M. Gell-Mann. "A Schematic Model of Baryons and Mesons". In: *Resonance* 24 (1964), pp. 923–925 (cited on page 3).
- [15] G. Zweig. "An SU(3) model for strong interaction symmetry and its breaking. Version 2". In: *DEVELOPMENTS IN THE QUARK THEORY OF HADRONS. VOL. 1. 1964 - 1978*. Ed. by D. B. Lichtenberg and S. P. Rosen. Feb. 1964, pp. 22–101 (cited on page 3).
- [16] D. J. Gross and F. Wilczek. "Ultraviolet Behavior of Non-Abelian Gauge Theories". In: *PRL* 30.26 (June 1973), pp. 1343–1346. doi: [10.1103/PhysRevLett.30.1343](https://doi.org/10.1103/PhysRevLett.30.1343) (cited on page 3).
- [17] C. Giunti and C. W. Kim. *Fundamentals of Neutrino Physics and Astrophysics*. Oxford University Press, Mar. 2007 (cited on page 3).

- [18] M. D. Schwartz. *Quantum Field Theory and the Standard Model*. Cambridge University Press, 2013 (cited on page 3).
- [19] A. Terliuk. "Measurement of atmospheric neutrino oscillations and search for sterile neutrino mixing with IceCube DeepCore". PhD thesis. Berlin, Germany: Humboldt-Universität zu Berlin, Mathematisch-Naturwissenschaftliche Fakultät, 2018. doi: [10.18452/19304](https://doi.org/10.18452/19304) (cited on pages 5, 15, 25).
- [20] Y. Fukuda et al. "Evidence for Oscillation of Atmospheric Neutrinos". In: *Phys. Rev. Lett.* 81 (8 Aug. 1998), pp. 1562–1567. doi: [10.1103/PhysRevLett.81.1562](https://doi.org/10.1103/PhysRevLett.81.1562) (cited on page 6).
- [21] Q. R. Ahmad and other. "Direct Evidence for Neutrino Flavor Transformation from Neutral-Current Interactions in the Sudbury Neutrino Observatory". In: *Phys. Rev. Lett.* 89 (1 June 2002), p. 011301. doi: [10.1103/PhysRevLett.89.011301](https://doi.org/10.1103/PhysRevLett.89.011301) (cited on page 6).
- [22] S. Alam et al. "Completed SDSS-IV extended Baryon Oscillation Spectroscopic Survey: Cosmological implications from two decades of spectroscopic surveys at the Apache Point Observatory". In: *Phys. Rev. D* 103 (8 Apr. 2021), p. 083533. doi: [10.1103/PhysRevD.103.083533](https://doi.org/10.1103/PhysRevD.103.083533) (cited on page 6).
- [23] N. Aghanim et al. "Planck2018 results: VI. Cosmological parameters". In: *Astronomy & Astrophysics* 641 (Sept. 2020), A6. doi: [10.1051/0004-6361/201833910](https://doi.org/10.1051/0004-6361/201833910) (cited on page 6).
- [24] M. Aker et al. "Direct neutrino-mass measurement with sub-electronvolt sensitivity". In: *Nature Phys.* 18.2 (2022), pp. 160–166. doi: [10.1038/s41567-021-01463-1](https://doi.org/10.1038/s41567-021-01463-1) (cited on page 6).
- [25] P. Astier et al. "Search for heavy neutrinos mixing with tau neutrinos". In: *Phys. Lett. B* 506 (2001), pp. 27–38. doi: [10.1016/S0370-2693\(01\)00362-8](https://doi.org/10.1016/S0370-2693(01)00362-8) (cited on page 10).
- [26] R. Acciari et al. "New Constraints on Tau-Coupled Heavy Neutral Leptons with Masses mN=280–970 MeV". In: *Phys. Rev. Lett.* 127.12 (2021), p. 121801. doi: [10.1103/PhysRevLett.127.121801](https://doi.org/10.1103/PhysRevLett.127.121801) (cited on page 10).
- [27] J. Orloff, A. N. Rozanov, and C. Santoni. "Limits on the mixing of tau neutrino to heavy neutrinos". In: *Phys. Lett. B* 550 (2002), pp. 8–15. doi: [10.1016/S0370-2693\(02\)02769-7](https://doi.org/10.1016/S0370-2693(02)02769-7) (cited on page 10).
- [28] I. Boiarska et al. "Blast from the past: constraints from the CHARM experiment on Heavy Neutral Leptons with tau mixing". In: (July 2021) (cited on page 10).
- [29] P. Abreu et al. "Search for neutral heavy leptons produced in Z decays". In: *Z. Phys. C* 74 (1997). [Erratum: *Z.Phys.C* 75, 580 (1997)], pp. 57–71. doi: [10.1007/s002880050370](https://doi.org/10.1007/s002880050370) (cited on page 10).
- [30] M. Tanabashi et al. "Review of Particle Physics". In: *Phys. Rev. D* 98 (3 Aug. 2018), p. 030001. doi: [10.1103/PhysRevD.98.030001](https://doi.org/10.1103/PhysRevD.98.030001) (cited on pages 12, 13, 24).
- [31] M. Honda et al. "Atmospheric neutrino flux calculation using the NRLMSISE-00 atmospheric model". In: *Phys. Rev. D* 92 (2 July 2015), p. 023004. doi: [10.1103/PhysRevD.92.023004](https://doi.org/10.1103/PhysRevD.92.023004) (cited on pages 12, 38).
- [32] A. Fedynitch et al. "Calculation of conventional and prompt lepton fluxes at very high energy". In: *European Physical Journal Web of Conferences*. Vol. 99. European Physical Journal Web of Conferences. Aug. 2015, p. 08001. doi: [10.1051/epjconf/20159908001](https://doi.org/10.1051/epjconf/20159908001) (cited on page 12).
- [33] S. Bilenky and B. Pontecorvo. "Lepton mixing and neutrino oscillations". In: *Physics Reports* 41.4 (1978), pp. 225–261. doi: [10.1016/0370-1573\(78\)90095-9](https://doi.org/10.1016/0370-1573(78)90095-9) (cited on page 13).
- [34] P. A. M. Dirac. "The Quantum Theory of the Emission and Absorption of Radiation". In: *Proceedings of the Royal Society of London Series A* 114.767 (Mar. 1927), pp. 243–265. doi: [10.1098/rspa.1927.0039](https://doi.org/10.1098/rspa.1927.0039) (cited on page 13).
- [35] J. A. Formaggio and G. P. Zeller. "From eV to EeV: Neutrino cross sections across energy scales". In: *Rev. Mod. Phys.* 84 (3 Sept. 2012), pp. 1307–1341. doi: [10.1103/RevModPhys.84.1307](https://doi.org/10.1103/RevModPhys.84.1307) (cited on page 15).
- [36] P. Coloma et al. "GeV-scale neutrinos: interactions with mesons and DUNE sensitivity". In: *Eur. Phys. J. C* 81.1 (2021), p. 78. doi: [10.1140/epjc/s10052-021-08861-y](https://doi.org/10.1140/epjc/s10052-021-08861-y) (cited on pages 16, 31, 33, 34).
- [37] P. B. Price, K. Woschnagg, and D. Chirkin. "Age vs depth of glacial ice at South Pole". In: *Geophysical Research Letters* 27.14 (2000), pp. 2129–2132. doi: <https://doi.org/10.1029/2000GL011351> (cited on page 20).

- [38] R. Abbasi et al. "In-situ estimation of ice crystal properties at the South Pole using LED calibration data from the IceCube Neutrino Observatory". In: *The Cryosphere Discussions* 2022 (2022), pp. 1–48. doi: [10.5194/tc-2022-174](https://doi.org/10.5194/tc-2022-174) (cited on page 20).
- [39] R. Abbasi et al. "The IceCube data acquisition system: Signal capture, digitization, and timestamping". In: *Nuclear Instruments and Methods in Physics Research Section A: Accelerators, Spectrometers, Detectors and Associated Equipment* 601.3 (2009), pp. 294–316. doi: <https://doi.org/10.1016/j.nima.2009.01.001> (cited on pages 20, 21, 42).
- [40] M. G. Aartsen et al. "Energy Reconstruction Methods in the IceCube Neutrino Telescope". In: *JINST* 9 (2014), P03009. doi: [10.1088/1748-0221/9/03/P03009](https://doi.org/10.1088/1748-0221/9/03/P03009) (cited on pages 21, 53).
- [41] J. Feintzeig. "Searches for Point-like Sources of Astrophysical Neutrinos with the IceCube Neutrino Observatory". PhD thesis. University of Wisconsin, Madison, Jan. 2014 (cited on pages 21, 50, 70, 71).
- [42] N. Kulacz. "In Situ Measurement of the IceCube DOM Efficiency Factor Using Atmospheric Minimum Ionizing Muons". MA thesis. University of Alberta, 2019 (cited on pages 21, 50, 70, 71).
- [43] R. Abbasi et al. "The design and performance of IceCube DeepCore". In: *Astropart. Phys.* 35.10 (2012), pp. 615–624. doi: [10.1016/j.astropartphys.2012.01.004](https://doi.org/10.1016/j.astropartphys.2012.01.004) (cited on pages 21, 41, 42).
- [44] P. A. Cherenkov. "Visible Radiation Produced by Electrons Moving in a Medium with Velocities Exceeding that of Light". In: *Phys. Rev.* 52 (4 Aug. 1937), pp. 378–379. doi: [10.1103/PhysRev.52.378](https://doi.org/10.1103/PhysRev.52.378) (cited on page 22).
- [45] I. Frank and I. Tamm. "Coherent visible radiation from fast electrons passing through matter". In: *C. R. Acad. Sci. USSR* 14 (1937), pp. 109–114 (cited on pages 22, 23).
- [46] I. Tamm. "Radiation Emitted by Uniformly Moving Electrons". In: *Selected Papers*. Ed. by B. M. Bolotovskii, V. Y. Frenkel, and R. Peierls. Berlin, Heidelberg: Springer Berlin Heidelberg, 1991, pp. 37–53. doi: [10.1007/978-3-642-74626-0_3](https://doi.org/10.1007/978-3-642-74626-0_3) (cited on pages 22, 23).
- [47] L. Rädel and C. Wiebusch. "Calculation of the Cherenkov light yield from low energetic secondary particles accompanying high-energy muons in ice and water with Geant4 simulations". In: *Astroparticle Physics* 38 (Oct. 2012), pp. 53–67. doi: [10.1016/j.astropartphys.2012.09.008](https://doi.org/10.1016/j.astropartphys.2012.09.008) (cited on pages 23, 39).
- [48] D. Chirkin and W. Rhode. "Propagating leptons through matter with Muon Monte Carlo (MMC)". In: (July 2004) (cited on pages 23, 24).
- [49] L. Raedel. "Simulation Studies of the Cherenkov Light Yield from Relativistic Particles in High-Energy Neutrino Telescopes with Geant4". MA thesis. Aachen, Germany: Rheinisch-Westfälischen Technischen Hochschule, 2012 (cited on pages 23, 24).
- [50] S. Agostinelli et al. "Geant4—a simulation toolkit". In: *Nucl. Instr. Meth. Phys. Res.* 506.3 (July 2003), pp. 250–303. doi: [10.1016/s0168-9002\(03\)01368-8](https://doi.org/10.1016/s0168-9002(03)01368-8) (cited on pages 24, 39).
- [51] T. Gabriel et al. "Energy dependence of hadronic activity". In: *Nuclear Instruments and Methods in Physics Research Section A: Accelerators, Spectrometers, Detectors and Associated Equipment* 338.2 (1994), pp. 336–347. doi: [https://doi.org/10.1016/0168-9002\(94\)91317-X](https://doi.org/10.1016/0168-9002(94)91317-X) (cited on page 24).
- [52] L. Fischer. https://github.com/LeanderFischer/icetray_double_cascade_generator_functions (cited on page 27).
- [53] R. Abbasi et al. "LeptonInjector and LeptonWeighter: A neutrino event generator and weighter for neutrino observatories". In: *Comput. Phys. Commun.* 266 (2021), p. 108018. doi: [10.1016/j.cpc.2021.108018](https://doi.org/10.1016/j.cpc.2021.108018) (cited on page 30).
- [54] J. Alwall et al. "The automated computation of tree-level and next-to-leading order differential cross sections, and their matching to parton shower simulations". In: *JHEP* 07 (2014), p. 079. doi: [10.1007/JHEP07\(2014\)079](https://doi.org/10.1007/JHEP07(2014)079) (cited on page 31).
- [55] C. Argüelles. <https://github.com/arguelles/NuXSpIMkr> (cited on pages 31, 32).
- [56] N. Whitehorn, J. van Santen, and S. Lafebre. "Penalized splines for smooth representation of high-dimensional Monte Carlo datasets". In: *Computer Physics Communications* 184.9 (2013), pp. 2214–2220. doi: <https://doi.org/10.1016/j.cpc.2013.04.008> (cited on pages 31, 53).

- [57] J.-M. Levy. "Cross-section and polarization of neutrino-produced tau's made simple". In: *J. Phys. G* 36 (2009), p. 055002. doi: [10.1088/0954-3899/36/5/055002](https://doi.org/10.1088/0954-3899/36/5/055002) (cited on page 32).
- [58] E. Tiesinga et al. "CODATA recommended values of the fundamental physical constants: 2018". In: *Rev. Mod. Phys.* 93 (2 July 2021), p. 025010. doi: [10.1103/RevModPhys.93.025010](https://doi.org/10.1103/RevModPhys.93.025010) (cited on page 33).
- [59] <https://launchpad.net/mg5amcnlo/3.0/3.3.x> (cited on page 34).
- [60] A. Alloul et al. "FeynRules 2.0 - A complete toolbox for tree-level phenomenology". In: *Comput. Phys. Commun.* 185 (2014), pp. 2250–2300. doi: [10.1016/j.cpc.2014.04.012](https://doi.org/10.1016/j.cpc.2014.04.012) (cited on page 34).
- [61] R. Abbasi et al. "Measurement of atmospheric neutrino mixing with improved IceCube DeepCore calibration and data processing". In: *Phys. Rev. D* 108 (1 July 2023), p. 012014. doi: [10.1103/PhysRevD.108.012014](https://doi.org/10.1103/PhysRevD.108.012014) (cited on pages 37, 44, 47–49).
- [62] C. Andreopoulos et al. "The GENIE Neutrino Monte Carlo Generator: Physics and User Manual". In: (2015) (cited on pages 39, 49).
- [63] M. Glück, E. Reya, and A. Vogt. "Dynamical parton distributions revisited". In: *The European Physical Journal C* 5 (Sept. 1998), pp. 461–470. doi: [10.1007/s100529800978](https://doi.org/10.1007/s100529800978) (cited on page 39).
- [64] A. Bodek and U. K. Yang. "Higher twist, xi(omega) scaling, and effective LO PDFs for lepton scattering in the few GeV region". In: *Journal of Physics G: Nuclear and Particle Physics* 29.8 (2003), p. 1899. doi: [10.1088/0954-3899/29/8/369](https://doi.org/10.1088/0954-3899/29/8/369) (cited on page 39).
- [65] J.-H. Koehne et al. "PROPOSAL: A tool for propagation of charged leptons". In: *Computer Physics Communications* 184.9 (2013), pp. 2070–2090. doi: <https://doi.org/10.1016/j.cpc.2013.04.001> (cited on page 39).
- [66] Y. Becherini et al. "A parameterisation of single and multiple muons in the deep water or ice". In: *Astroparticle Physics* 25.1 (2006), pp. 1–13. doi: <https://doi.org/10.1016/j.astropartphys.2005.10.005> (cited on page 39).
- [67] D. Heck et al. "CORSIKA: A Monte Carlo code to simulate extensive air showers". In: (Feb. 1998) (cited on page 39).
- [68] T. K. Gaisser. "Spectrum of cosmic-ray nucleons, kaon production, and the atmospheric muon charge ratio". In: *Astropart. Phys.* 35 (2012), pp. 801–806. doi: [10.1016/j.astropartphys.2012.02.010](https://doi.org/10.1016/j.astropartphys.2012.02.010) (cited on page 39).
- [69] R. Engel et al. "The hadronic interaction model Sibyll – past, present and future". In: *EPJ Web Conf.* 145 (2017). Ed. by B. Pattison, p. 08001. doi: [10.1051/epjconf/201614508001](https://doi.org/10.1051/epjconf/201614508001) (cited on page 39).
- [70] C. Kopper et al. <https://github.com/claudiok/clsim> (cited on page 40).
- [71] D. Chirkin et al. "Photon Propagation using GPUs by the IceCube Neutrino Observatory". In: *2019 15th International Conference on eScience (eScience)*. 2019, pp. 388–393. doi: [10.1109/eScience50050](https://doi.org/10.1109/eScience50050) (cited on page 40).
- [72] M. G. Aartsen et al. "Measurement of South Pole ice transparency with the IceCube LED calibration system". In: *Nucl. Instrum. Meth. A* 711 (2013), pp. 73–89. doi: [10.1016/j.nima.2013.01.054](https://doi.org/10.1016/j.nima.2013.01.054) (cited on page 40).
- [73] A. Trettin. "Search for eV-scale sterile neutrinos with IceCube DeepCore". PhD thesis. Berlin, Germany: Humboldt-Universität zu Berlin, Mathematisch-Naturwissenschaftliche Fakultät, 2023. doi: <https://github.com/atrettin/PhD-Thesis> (cited on pages 40, 41, 50).
- [74] G. Mie. "Beiträge zur Optik trüber Medien, speziell kolloidaler Metallösungen". In: *Annalen der Physik* 330.3 (1908), pp. 377–445. doi: <https://doi.org/10.1002/andp.19083300302> (cited on page 40).
- [75] L. G. Henyey and J. L. Greenstein. "Diffuse radiation in the Galaxy." In: *apj* 93 (Jan. 1941), pp. 70–83. doi: [10.1086/144246](https://doi.org/10.1086/144246) (cited on page 40).
- [76] S. Fiedlschuster. "The Effect of Hole Ice on the Propagation and Detection of Light in IceCube". In: (Apr. 2019) (cited on page 40).

- [77] M. G. Aartsen et al. "In-situ calibration of the single-photoelectron charge response of the IceCube photomultiplier tubes". In: *Journal of Instrumentation* 15.6 (June 2020), P06032. doi: [10.1088/1748-0221/15/06/P06032](https://doi.org/10.1088/1748-0221/15/06/P06032) (cited on page 41).
- [78] M. Larson. "Simulation and Identification of Non-Poissonian Noise Triggers in the IceCube Neutrino Detector". Available at <https://ir.ua.edu/handle/123456789/1927>. MA thesis. University of Alabama, Tuscaloosa, AL, USA, 2013 (cited on page 41).
- [79] M. Larson. "A Search for Tau Neutrino Appearance with IceCube-DeepCore". available at https://discoverycenter.nbi.ku.dk/teaching/thesis_page/mjlarson_thesis.pdf. PhD thesis. University of Copenhagen, Denmark, 2018 (cited on page 41).
- [80] E. Lohfink. "Testing nonstandard neutrino interaction parameters with IceCube-DeepCore". PhD thesis. Mainz, Germany: Johannes Gutenberg-Universität Mainz, Fachbereich für Physik, Mathematik und Informatik, 2023. doi: <http://doi.org/10.25358/open-science-9288> (cited on page 41).
- [81] M. G. Aartsen et al. "The IceCube Neutrino Observatory: Instrumentation and Online Systems". In: *JINST* 12.03 (2017), P03012. doi: [10.1088/1748-0221/12/03/P03012](https://doi.org/10.1088/1748-0221/12/03/P03012) (cited on page 41).
- [82] J. H. Friedman. "Stochastic gradient boosting". In: *Computational Statistics & Data Analysis* 38 (2002), pp. 367–378 (cited on page 43).
- [83] R. Abbasi et al. "Low energy event reconstruction in IceCube DeepCore". In: *Eur. Phys. J. C* 82.9 (2022), p. 807. doi: [10.1140/epjc/s10052-022-10721-2](https://doi.org/10.1140/epjc/s10052-022-10721-2) (cited on pages 44, 54).
- [84] S. Yu and J. Micallef. "Recent neutrino oscillation result with the IceCube experiment". In: *38th International Cosmic Ray Conference*. July 2023 (cited on pages 44, 68).
- [85] S. Yu and on behalf of the IceCube collaboration. "Direction reconstruction using a CNN for GeV-scale neutrinos in IceCube". In: *Journal of Instrumentation* 16.11 (2021), p. C11001. doi: [10.1088/1748-0221/16/11/C11001](https://doi.org/10.1088/1748-0221/16/11/C11001) (cited on page 45).
- [86] J. Micallef. <https://github.com/jessimic/LowEnergyNeuralNetwork> (cited on page 45).
- [87] M. Huennefeld. "Deep Learning in Physics exemplified by the Reconstruction of Muon-Neutrino Events in IceCube". In: *PoS ICRC2017* (2017), p. 1057. doi: [10.22323/1.301.1057](https://doi.org/10.22323/1.301.1057) (cited on page 45).
- [88] H. Dembinski et al. "Data-driven model of the cosmic-ray flux and mass composition from 10 GeV to 10^{11} GeV". In: *PoS ICRC2017* (2017), p. 533. doi: [10.22323/1.301.0533](https://doi.org/10.22323/1.301.0533) (cited on page 48).
- [89] G. D. Barr et al. "Uncertainties in atmospheric neutrino fluxes". In: *Phys. Rev. D* 74 (9 Nov. 2006), p. 094009. doi: [10.1103/PhysRevD.74.094009](https://doi.org/10.1103/PhysRevD.74.094009) (cited on page 48).
- [90] J. Evans et al. "Uncertainties in atmospheric muon-neutrino fluxes arising from cosmic-ray primaries". In: *Phys. Rev. D* 95 (2 Jan. 2017), p. 023012. doi: [10.1103/PhysRevD.95.023012](https://doi.org/10.1103/PhysRevD.95.023012) (cited on pages 48, 70, 71).
- [91] A. Fedynitch et al. <https://github.com/afedynitch/MCEq> (cited on page 48).
- [92] G. D. Barr et al. "Uncertainties in Atmospheric Neutrino Fluxes". In: *Phys. Rev. D* 74 (2006), p. 094009. doi: [10.1103/PhysRevD.74.094009](https://doi.org/10.1103/PhysRevD.74.094009) (cited on page 48).
- [93] F. Riehn et al. "Hadronic interaction model sibyll 2.3d and extensive air showers". In: *Phys. Rev. D* 102 (6 Sept. 2020), p. 063002. doi: [10.1103/PhysRevD.102.063002](https://doi.org/10.1103/PhysRevD.102.063002) (cited on page 48).
- [94] A. Cooper-Sarkar, P. Mertsch, and S. Sarkar. "The high energy neutrino cross-section in the Standard Model and its uncertainty". In: *JHEP* 08 (2011), p. 042. doi: [10.1007/JHEP08\(2011\)042](https://doi.org/10.1007/JHEP08(2011)042) (cited on page 49).
- [95] Q. Wu et al. "A precise measurement of the muon neutrino–nucleon inclusive charged current cross section off an isoscalar target in the energy range $2.5 < E < 40$ GeV by NOMAD". In: *Physics Letters B* 660.1 (2008), pp. 19–25. doi: <https://doi.org/10.1016/j.physletb.2007.12.027> (cited on page 49).
- [96] M. M. Tzanov. "Precise measurement of neutrino and anti-neutrino differential cross sections on iron". PhD thesis. University of Pittsburgh, Pennsylvania, Jan. 2005 (cited on page 49).
- [97] W. G. Seligman. "A next-to-leading-order QCD analysis of neutrino-iron structure functions at the Tevatron". PhD thesis. Columbia University, New York, Aug. 1997 (cited on page 49).

- [98] Rongen, Martin. "Measuring the optical properties of IceCube drill holes". In: *EPJ Web of Conferences* 116 (2016), p. 06011. doi: [10.1051/epjconf/201611606011](https://doi.org/10.1051/epjconf/201611606011) (cited on page 50).
- [99] R. Abbasi et al. "Measurement of Astrophysical Tau Neutrinos in IceCube's High-Energy Starting Events". In: *arXiv e-prints* (Nov. 2020) (cited on page 53).
- [100] M. Usner. "Search for Astrophysical Tau-Neutrinos in Six Years of High-Energy Starting Events in the IceCube Detector". PhD thesis. Berlin, Germany: Humboldt-Universität zu Berlin, Mathematisch-Naturwissenschaftliche Fakultät, 2018. doi: [10.18452/19458](https://doi.org/10.18452/19458) (cited on page 53).
- [101] P. Hallen. "On the Measurement of High-Energy Tau Neutrinos with IceCube". MA thesis. Aachen, Germany: RWTH Aachen University, 2013 (cited on page 53).
- [102] V. Barger et al. "Matter effects on three-neutrino oscillations". In: *Phys. Rev. D* 22 (11 Dec. 1980), pp. 2718–2726. doi: [10.1103/PhysRevD.22.2718](https://doi.org/10.1103/PhysRevD.22.2718) (cited on page 67).
- [103] A. M. Dziewonski and D. L. Anderson. "Preliminary reference Earth model". In: *Physics of the Earth and Planetary Interiors* 25.4 (1981), pp. 297–356. doi: [https://doi.org/10.1016/0031-9201\(81\)90046-7](https://doi.org/10.1016/0031-9201(81)90046-7) (cited on page 67).
- [104] L. Fischer, R. Naab, and A. Trettin. "Treating detector systematics via a likelihood free inference method". In: *Journal of Instrumentation* 18.10 (2023), P10019. doi: [10.1088/1748-0221/18/10/P10019](https://doi.org/10.1088/1748-0221/18/10/P10019) (cited on page 71).
- [105] M. G. Aartsen et al. "Computational techniques for the analysis of small signals in high-statistics neutrino oscillation experiments". In: *Nucl. Instrum. Meth. A* 977 (2020), p. 164332. doi: [10.1016/j.nima.2020.164332](https://doi.org/10.1016/j.nima.2020.164332) (cited on page 71).
- [106] <https://github.com/icecube/pisa> (cited on page 71).
- [107] R. S. Nickerson. "Confirmation Bias: A Ubiquitous Phenomenon in Many Guises". In: *Review of General Psychology* 2 (1998), pp. 175–220 (cited on pages 71, 72).
- [108] H. Dembinski et al. *scikit-hep/iminuit: v2.17.0*. Version v2.17.0. Sept. 2022. doi: [10.5281/zenodo.7115916](https://doi.org/10.5281/zenodo.7115916) (cited on page 72).
- [109] F. James and M. Roos. "Minuit: A System for Function Minimization and Analysis of the Parameter Errors and Correlations". In: *Comput. Phys. Commun.* 10 (1975), pp. 343–367. doi: [10.1016/0010-4655\(75\)90039-9](https://doi.org/10.1016/0010-4655(75)90039-9) (cited on page 72).
- [110] S. S. Wilks. "The Large-Sample Distribution of the Likelihood Ratio for Testing Composite Hypotheses". In: *The Annals of Mathematical Statistics* 9.1 (1938), pp. 60–62. doi: [10.1214/aoms/1177732360](https://doi.org/10.1214/aoms/1177732360) (cited on page 74).